IN-SITU DOPED FZO FILMS BY ALD FOR TCO APPLICATIONS

A THESIS SUBMITTED TO
THE GRADUATE SCHOOL OF NATURAL AND APPLIED SCIENCES
OF
MIDDLE EAST TECHNICAL UNIVERSITY

BY

MERYEM TUNÇKANAT

IN PARTIAL FULFILLMENT OF THE REQUIREMENTS
FOR
THE DEGREE OF MASTER OF SCIENCE
IN
MICRO AND NANOTECHNOLOGY

SEPTEMBER 2023

Approval of the thesis:

IN-SITU DOPED FZO FILMS BY ALD FOR TCO APPLICATIONS

submitted by **MERYEM TUNÇKANAT** in partial fulfillment of the requirements for the degree of **Master of Science** i**n Micro and Nanotechnology, Middle East Technical University** by,

Prof. Dr. Halil Kalıpçılar
Dean, Graduate School of **Natural and Applied Sciences** _____

Prof. Dr. Deniz Üner
Head of the Department, **Micro and Nanotechnology** _____

Assist. Prof. Dr. Bilge İmer
Supervisor, **Metallurgical and Materials Eng., METU** _____

Prof. Dr. Alpan Bek
Co-Supervisor, **Physics, METU** _____

Examining Committee Members:

Prof. Dr. Hakan Ateş
Metallurgical and Materials Eng., Gazi Uni _____

Assist. Prof. Dr. Bilge İmer
Metallurgical and Materials Eng., METU _____

Prof. Dr. Alpan Bek
Physics, METU _____

Assoc. Prof. Dr. Selçuk Yerci
Electrical and Electronics Eng., METU _____

Assist. Prof. Dr. Yusuf Keleştemur
Metallurgical and Materials Eng., METU _____

Date: 04.09.2023

I hereby declare that all information in this document has been obtained and presented in accordance with academic rules and ethical conduct. I also declare that, as required by these rules and conduct, I have fully cited and referenced all material and results that are not original to this work.

Name Last name : Meryem Tunçkanat

Signature :

ABSTRACT

IN-SITU DOPED FZO FILMS BY ALD FOR TCO APPLICATIONS

Tunçkanat, Meryem
Master of Science, Micro and Nanotechnology
Supervisor : Assist. Prof. Dr. Bilge İmer
Co-Supervisor: Prof. Dr. Alpan Bek

September 2023, 101 pages

Transparent conductive oxides (TCOs) that have high transparency in the visible spectra with outstanding electrical conductivity have drawn great interest with their wide-range use in optoelectronic applications. While indium tin oxide (ITO) is the most commercially used TCO, the replacement of it with in indium-free TCOs is essential due to the toxicity, scarcity, and high cost of indium. Zinc oxide (ZnO), an n-type semiconductor with a direct band gap of 3.37 eV, and its doped forms are suitable candidates for indium-free TCOs along with several additional advantages over ITO, such as their abundancy in nature, non-toxicity, low cost, and easy fabrication. If fluorine anion is selected as a dopant, the formed material is called fluorine doped ZnO (FZO). In literature, lowest resistivity and highest visible transmittance of FZO was reported as $4x10^{-4}$ Ωcm and 87%, respectively and the resistivity and the visible transmittance of ITO reported as $5.1x10^{-4}$ Ωcm and 88.5%, respectively. Thus, the electrical and optical properties of FZO are compatible with those of ITO.

ALD is a unique deposition technique that has several benefits, such as providing conformal coverage and producing highly uniform thin films at low temperatures. Due to lack of fluorine precursors suitable for ALD process, there was only one study that reported FZO growth utilizing home-made HF/H_2O as a source. But HF is an

extremely strong acid that damages the equipment when used and it should be used with teflon coating in equipment and with extremely diluted (approximately 0.5%) solution to obtain 1.2 at.% fluorine doping. . In this study, fluorination of zinc oxide films in ALD was demonstrated for the first time in the literature by using a new homemade precursor, a mixture of ammonium fluoride (NH_4F/H_2O) solution, as a fluorine doping source. Compared with HF, NH_4F is much weaker acid (0.125% HF has 1.1 nm/s etch rate while 10% NH4F has 1.1 nm/s etch rate for ZnO) and therefore, it is also much easier to fine tune the amount of fluorine amount incorporated in zinc oxide films. To study fluorine incorporation with this new precursor in ALD, experiments were set with changing variables. All FZO films were grown over silicon and quartz substrates. Diethyl zinc (DEZ) was used as the zinc source, and a mixture of NH_4F/H_2O solutions with different concentrations (1%-40% NH_4F) was used as the oxygen and fluorine source. FZO thin films were grown at temperatures between 160°C-200°C. The effect of canister temperature on fluorine doping was observed at 180 °C with a 30% NH4F/DI mixture, and the canister temperature was varied at room temperature, 40 °C, and 50°C and kept at those temperatures during the deposition. The lowest fluorine concentration was founded in deposition temperature at 180 °C with a 30% NH4F/DI mixture, 40 °C canister temperature as 2.62 at.% and the highest fluorine doping was achieved at 180 °C with a 40% NH4F/DI mixture, 50 °C canister temperature as 29.08 at.%. In literature the resistivity and optical transmittance at 400-800 nm for CVD-grown FZO film with 3 at. % F doping was reported as 18.57 Ω.cm and 84% respectively. In this study, the best electrical properties were achieved at 2.62 at. % fluorine doping with 1.24 $x10^{18}$ $1/cm^3$ carrier concentration, 2.14 Ω.cm resistivity, and 2.36 Hall mobility cm^2/Vs. The average transmittance values 400 nm to 800 nm of all FZO films are approximately 80% and above.

Keywords: Atomic Layer Deposition, Fluorine Doped Zinc Oxide, In-situ Doping, Transparent Conductive Oxide

ÖZ

TCO UYGULAMARI İÇİN ALD TARAFINDAN YERİNDE KATKILANMIŞ FZO FİLMLER

Tunçkanat, Meryem
Yüksek Lisans, Mikro ve Nanoteknoloji
Tez Yöneticisi: Dr. Öğr. Ü. Bilge İmer
Ortak Tez Yöneticisi: Prof. Dr. Alpan Bek

Eylül 2023, 101 sayfa

Görünür spektrumlarda yüksek şeffaflığa ve üstün elektriksel iletkenliğe sahip olan şeffaf iletken oksitler (SİO'ler), çeşitli optoelektronik uygulamalarda geniş kullanım alanları ile büyük ilgi görmektedir. İndiyum kalay oksit (ITO) ticari olarak en çok kullanılan SİO olmasına rağmen, indiyumun toksisitesi, kıtlığı ve yüksek maliyeti nedeniyle bunun indiyum içermeyen TCO'larla değiştirilmesi amaçlanmaktadır. Doğrudan bant aralığı 3,37 eV olan n tipi bir yarı iletken olan çinko oksit (ZnO) ve katkılı formları, doğada bol bulunması, toksik olmaması, düşük maliyetli olması ve kolay imal edilmesi sebebi ile indiyum içermeyen TCO'lara uygun bir adaydır. Katkı maddesi olarak flor anyonu seçilirse oluşan malzemeye flor katkılı ZnO (FZO) adı verilir. Literatürde FZO'nun en düşük özdirenci ve en yüksek görünür geçirgenliği sırasıyla $4x10^{-4}$ Ωcm ve %87 olarak, ITO'nun özdirenci ve görünür geçirgenliği ise sırasıyla $5,1x10^{-4}$ Ωcm ve %88,5 olarak rapor edilmiştir. Bu nedenle FZO'nun elektriksel ve optik özellikleri ITO'nunkilerle uyumludur.

ALD, uygun kaplama sağlamak ve düşük sıcaklıklarda oldukça düzgün ince filmler üretmek gibi çeşitli faydaları olan benzersiz bir biriktirme tekniğidir. ALD sürecine uygun flor öncüllerinin bulunmamasından dolayı, kaynak olarak ev yapımı HF/H_2O'yu kullanan FZO büyümesini bildiren tek bir çalışma vardı. Ancak HF,

kullanıldığında ekipmana zarar veren son derece güçlü bir asittir ve %1,2 oranında flor katkısı elde etmek için aşırı derecede seyreltilmiş (yaklaşık %0,5) kullanılmalıdır. Bu çalışmada, ALD'de çinko oksit filmlerin florlanması, literatürde ilk kez, bu çalışmada flor doping kaynağı olarak yeni bir ev yapımı öncü olan amonyum florür (NH_4F/H_2O) çözeltisi karışımı kullanılarak gösterilmiştir. HF ile karşılaştırıldığında, NH_4F çok daha zayıf bir asittir (ZnO için %0,125 HF, 1,1 nm/s aşındırma hızına sahipken, %10 NH4F 1,1 nm/s aşındırma hızına sahiptir) ve bu nedenle, flor katkı miktarının ayarını yapmak da çok daha kolaydır. Tüm FZO filmleri silikon ve kuvars substratlar üzerinde büyütülmüştür. Çinko kaynağı olarak dietil çinko (DEZ), oksijen ve flor kaynağı olarak ise farklı konsantrasyonlarda (%1-%40 NH_4F) NH_4F/H_2O karışımı kullanılmıştır. FZO ince filmleri 160°C-200°C arasındaki sıcaklıklarda büyütülmüştür. Kaynak kutusu sıcaklığının flor katkısı üzerindeki etkisini ölçmek amacıyla %30 NH_4F/DI karışımı 180°C büyütme sıcaklığı ve kutu sıcaklığı, oda sıcaklığı, 40°C ve 50°C'ye ayarlanmış ve büyütme sırasında bu sıcaklıklarda tutulmuştur. En düşük flor konsantrasyonu 180 °C biriktirme sıcaklığında %30 NH_4F/DI karışımı ile, 40 °C teneke kutu sıcaklığında %2,62 olarak, en yüksek flor katkısı ise 180 °C'de %40 NH_4F/DI karışımı ile 50 °C teneke kutu sıcaklığında %29,08 olarak elde edilmiştir. Literatürde CVD ile büyütülmüş 3 at. % F katkılı FZO filmi için direnç ve 400-800 nm'de ortalama optik geçirgenlik sırasıyla 18.57 Ω.cm ve %84 olarak rapor edilmiştir. Bu çalışmada en iyi elektriksel özellikler 2,62% flor katkısı ile 1,24 $x10^{18}$ $1/cm^3$ taşıyıcı konsantrasyonu, 2,14 Ω.cm direnç ve 2,36 Hall mobilitesi cm2/Vs olarak elde edilmiştir. Tüm FZO filmlerinin 400-800 nm arası ortalama geçirgenlik değerleri yaklaşık %80 üzerindedir.

Anahtar Kelimeler: Atomik Katman Biriktirme, Flor Katkılı Çinko Oksit, Yerinde Katkılama, Saydam İletken Oksit

To my lovely sisters,

Meliha & Ege

ACKNOWLEDGMENTS

Foremost, I would like to express my sincere gratitude to my advisor, Assist. Prof. Dr. Bilge İmer for her invaluable guidance, expertise, and continuous encouragement. Her insights and feedback have been instrumental in shaping this research.

I would like to thank Prof. Dr. Hakan Ateş for sharing the DEZ source when we ran out with our DEZ last minute with our laboratory and for his help. I would like to thank Prof. Dr. Raşit Turan, Associate Prof. Dr. Selçuk Yerci , Dr. Salar Habibpur Sedani, and Cem Maden, for providing me with all the resources of GÜNAM and assistance for my measurements. I would like to thank Prof. Dr. Mehmet Parlak for the Hall effect measurement. I also extend my gratitude to Prof. Dr. Levent Toppare and his student, Shadi Hosseini, for the UV-VIS measurement.

I am so thankful to Özge Demirdoğan, who has been more than just a lab mate who became one of my closest friends, for always standing by me and supporting me throughout this journey. I am grateful to my labmate İlayda Katırancı, who helped produce proper sample cylinders for our new homemade source., for making this thesis possible. I would like to thank my precious lab mates, Onur Daş, Ege Hacışahinoğlu, and Gaye Topcu, for their help and supportive role.

I would like to express my deepest gratitude to my mother Derya Tunçkanat and my sisters, Meliha Karagöz and Ege Tunçkanat and my brother-in-law Musa Karagöz, for their unwavering support and love throughout my journey. Their encouragement and belief in me have been my pillars of strength, guiding me through every challenge. I am truly fortunate to have such a loving and supportive family, and I owe a significant part of my success to them.

I want to extend my heartfelt thanks to my closest friends, Zeynel Yıldırım, Fatma Kılıç, and Begüm Bahçivan, who have been by my side through thick and thin. Your friendship has enriched my life in countless ways, and I am grateful for the moments

of laughter, companionship, and shared experiences we've had together. Your unwavering support has made my journey more enjoyable and meaningful.

TABLE OF CONTENTS

LIST OF TABLES

TABLES

LIST OF FIGURES

FIGURES

LIST OF ABBREVIATIONS

ALD	Atomic Layer Deposition
ALE	Atomic Layer Epitaxy
CVD	Chemical Vapor Deposition
DEZ	Diethly Zinc
DOS	Density of States
FPP	Four Point Probe
FTO	Fluorine doped Tin Oxide
FWHM	Full Width Half Maximum
FZO	Fluorine doped Zinc Oxide
GIXRD	Graxing Incidence X-Ray Diffraction
GPC	Growth Per Cycle
ITO	Indium Tin Oxide
PVD	Physical Vapor Deposition
SCCM	Standard cubic centimeters per minute
SE	Spectroscopic Ellipsometry
SIMS	Secondary Ion Mass Spectroscopy
TCO	Transparent Conductive Oxide
XPS	X-ray photoelectron spectroscopy

LIST OF SYMBOLS

σ	Electrical conductivity
μ	Mobility
h	Planck's constant
ε_0	The permittivity of free space
ε_μ	The static dielectric constant
λ	Mean free path
V_f	Drift velocity
ε_ρ	Low-frequency relative permittivity
N_d	Number of ionized donors
k	Boltzmann constant
λ_p	Plasma wavelength
w_p	Plasma frequency

CHAPTER 1

INTRODUCTION

Transparent conducting oxides (TCOs) are described as wide band gap semiconductor oxides with outstanding electrical conductivity and great optical transmittance at the visible spectrum. Not only their electrical properties but also the optical properties can be enhanced by native point defects and/or substitutional dopants (Coutts et al., 2000; Gordon, 2000; Lewis & Paine, 2000). These oxide-based materials must have average transmittance in the visible range greater than 80%, a carrier concentration of 10^{20}–10^{21} cm^{-3}, and resistivities of 10^{-3} Ω.cm or less (Minami, 2005).

The utilization of TCOs is essential as transparent electrodes in photovoltaic and optoelectronic devices such as solar cells (Dagkaldiran et al., 2009; Bernal-Correa et al., 2016; Colegrove et al., 2012; Park et al., 2018) light emitting diodes (LEDs) (Porch et al., 2004; Szabó et al., 2016), flat panel displays(Chae, 2001), touch panels (Wu, 2018) of tablet computers and phones, etc.

Over the past decades, the increased demand for TCOs for such applications has driven scientists to develop cost-effective new TCO materials with optimized electrical and optical properties by various fabrication methods. In Table 1.1 generally used TCOs and their dopants are listed (Minami, 2005)

Table 1.1. The example of TCO materials and their dopants

Oxides	**Dopants**
In_2O_3	Sn, F, Te, Ta, Ti, Ge, Hf, Mo, Zr, W, Nb
SnO_2	F, Ta, As, Sb, Nb
ZnO	Al, F, Ga, Hf, Ge, Si, Ti, In, Sc, Zr, Y, V, B
CdO	Sn, In

The TCO industry is dominated by fluorine-doped tin oxide (FTO) after indium tin oxide (ITO). The reason is that both ITO and FTO show transmittance above 80% in the visible wavelengths with low resistivities, on the order of 10^{-4} Ω.cm (Huang et al., 2021; Liao et al., 2011; Mehmood et al., 2017; Nishinaka & Yoshimoto, 2018). However, the exploration of alternative TCO materials has become vital in recent years because of the unstable expense of raw indium and tin (*Mineral Commodity Summaries*, 2002; *Mineral Commodity Summaries*, 2007; *Mineral Commodity Summaries*, 2012; *Mineral Commodity Summaries*, 2017; *Mineral Commodity Summaries*, 2022; *Mineral Commodity Summaries*, 2023). Zinc oxide (ZnO) is an n-type semiconductor that has a direct band gap (Eg = 3.37 eV). Its doped forms are proper candidates for replacing ITO and FTO along with various benefits such as their non-toxicity (Nordberg et al., 2007), abundance in nature, low-cost and easy fabrication (Hu & Gordon, 1991; Y. J. Lee et al., 2014; Mo et al., 2019).

The electrical and optical properties of ZnO are improved by doping via trivalent metal cations (B, Al, and Ga) (Y. J. Lee et al., 2014; Mo et al., 2019; Wenas et al., 1991) or halogen anions (Cl and F) (Liu et al., 2010a; Rousset et al., 2009). The most efficient doped form of ZnO is fluorine-doped zinc oxide (FZO) which is the main target of this thesis. The ionic radii of fluorine (0.136 nm) and oxygen (0.140 nm) ions are very close to each other, and the electronegativity of fluorine (3.98) is higher than that of oxygen (3.44). Therefore, fluorine easily substitutes oxygen sites intrinsic oxygen-related defects are eliminated as a result of the substitution and dangling bonds on the surface passivated by fluorine anions at grain boundaries. The doping mechanism of ZnO with fluorine will be discussed later.

The deposition of FZO thin films has been conducted by various physical vapor deposition (PVD) techniques such as sputtering (Tsai et al., 2009), pulsed laser deposition (Cao et al., 2011), electron beam evaporation (Xu et al., 2005), and chemical deposition methods such as solution-based spray pyrolysis (De La et al., 2002) and chemical vapor deposition (CVD) (Hu & Gordon, 1991).

Atomic layer deposition (ALD) is a CVD-like thin film deposition technique with self-limiting surface reactions (Suntola, 1989). Although ALD has several

advantages over PVD and CVD methods, in-situ fluorine doping by ALD is very problematic owing to the absence of a fluorine-based precursor. Only Park et al. achieved to produce FZO thin film via ALD by using hydrofluoric acid (HF) and deionized (DI) water (Choi & Park, 2014; Choi et al., 2015; Kang & Park, 2018). However, HF is an extremely corrosive material, and there is a necessity for a protective coating such as Teflon for all parts of the ALD system that will come into contact with HF (Park et al., 2015). On the other hand, ammonium fluoride (NH_4F) is not as strong an acid as HF, and when it is used in low concentrations, there is no requirement to make any adjustments in the parts of the ALD system (Baboian et al., 2004). The practical and economic advantages can be obtained in this way.

In this thesis, in-situ fluorination of ZnO films was conducted in ALD using a new homemade precursor, a mixture of ammonium fluoride (NH_4F/H_2O) solution, as a fluorine source for the first time in literature.

1.1 History of TCOs

TCO materials have been investigated since the beginning of the twentieth century. The first examples, including CdO, Cu_2O, and PbO films deposited via thermal oxidation, were founded by Bädeker (Bädeker, 1907).

When the electronics industry emerged following the Second World War, transparent electrodes were studied for optoelectronic applications such as heated and antistatic windows and front electrodes in photocells (Preston, 1950). It was also suggested that other TCOs, like SnO_2, be researched as a transparent heating layer for cockpit windows of aircraft (McMaster, 1947). In addition, ZnO has explored a semiconductor compound for device application after the Second World War. However, for the first time, ZnO thin layer was used in surface acoustic wave devices due to its great piezoelectric properties, which were realized in the 1960s (Hutson, 1960). The industrial application of TCOs has been broadened since the end of the 1960s when infrared (IR) light filters consisting of In_2O_3 or tin were used to enhance the efficiency of low-pressure sodium discharge lamps by lowering heat losses (Van Boort & Groth, 1968).

The world struggled with the oil crisis at the beginning of the 1970s. This crisis led to the emergence of research and development studies in energy conservation and efficiency. The electrical and optical properties of spray-coated ITO as an optical filter were investigated in the middle of the 1970s for the first time (Köstlin et al., 1975). The objective of this study was to produce a layer that let not only visible light pass through but also reflects infrared radiation and, by that, lower heat transfer and increases energy efficiency. According to this research, heat mirror coatings containing thin metal oxide layers were developed for selectively reflecting different wavelengths of light (Lampert, 1981). In addition, evaporated ITO's electrical and optical properties and their application on energy-efficient windows were investigated (Hamberg & Granqvist, 1986).

The usage of TCOs in flat panel display technology became in demand due to their application on computer monitors and televisions. In 1999, Katayama analyzed the technology underlying thin film transistor liquid crystal displays (TFT-LCDs) (Katayama, 1999). ITO films were applied on large flat panel displays in 2006, aligned with Katayama's review (Betz et al., 2006).

There was an increasing interest in applying TCOs in solar energy in the 2000s. The fundamentals and usage of TC-ZnO (transparent conductive zinc oxide) in thin film solar cells were explored in 2008 (Ellmer et al., 2008), and a comprehensive overview of TCOs for solar energy was presented (Granqvist, 2009). Table 1.2 shows summarized history of TCO materials and their processes.

Table 1.2. The selected history of transparent conductive oxides and their fabrication methods

References	TCO Material	Production Method
Bädeker, 1907	CdO	Thermal Oxidation
Mcmaster, 1947	SnO2:Cl	Spray Pyrolysis
Lytle et al., 1951	SnO2:F	Spray Pyrolysis
Moehel, 1951	In2O3:Sn	Spray Pyrolysis

Table 1.2 (continued)

Dates & Davis, 1967	SnO2:Sb	Chemical Vapor Deposition
Nozik, 1974	Cd2SnO4	Sputtering
Nozik & Haacke, 1976	Cd2SnO4	Spray Pyrolysis
Gordon, 1979	SnO2:F	Chemical Vapor Deposition
Major et al., 1984	ZnO:In	Spray Pyrolysis
Minami et al., 1985	ZnO:Al	Sputtering
Qiu et al., 1987	ZnO:In	Sputtering
B. H. Choi et al., 1990	ZnO:Ga	Sputtering
Hu & Gordon, 1991	ZnO:F	Chemical Vapor Deposition
Enoki et al., 1992	Zn2SnO4	Sputtering
Hu & Gordon, 1992	ZnO:Al	Chemical Vapor Deposition
Mcgraw et al., 1995	Cd2SnO4	Pulsed Laser Deposition
Yamada et al., 1997	ZnO:B	Atomic Layer Deposition
Ott & Chang, 1999	ZnO:Ga	Atomic Layer Deposition
Kopalko et al., 2005	ZnO:Mn	Atomic Layer Deposition
Ceh et al., 2010	ZnO:Al	Atomic Layer Deposition
Lin et al., 2011	ZnO:Zr	Atomic Layer Deposition
Y. J. Choi & Park, 2014	ZnO:F	Atomic Layer Deposition

In conclusion, since their discovery in the early 20th century, transparent conductive oxides and their fabrication methods have advanced remarkably. There are several usages of TCOs, from solar energy to energy-efficient windows and flat panel displays. They provide energy efficiency for buildings, reduction of green gas emissions, and help to achieve advanced technology. The research and development

studies on TCO materials and their fabrication methods will open emerging applications along with their benefits.

1.2 The Electrical and Optical Properties of TCO

1.2.1 The Electrical Properties

TCOs are semiconductors that have broadband gap values. Generally, the electrical conductivity range of TCOs varies from 10^2 to 10^6 S/m. The electrical conductivity (σ) depends on the mobility of charge carriers (μe, μh) and carrier concentration (n,p). The electrical conductivity equation is given in Equation 1 (Coutts et al., 2000). The electric charge is shown by q.

$$\sigma = nq\mu_e + pq\mu_h \quad (1)$$

The Equation (1) can be simply for n-type TCOs as,

$$\sigma = nq\mu_e \quad (2)$$

The Equation (1) can be simply for p-type TCOs as,

$$\sigma = pq\mu_h \quad (3)$$

According to Equation (1), Equation (2), and Equation (3), increased carrier concentration or charge carrier will lead to enhanced electrical conductivity.

The density of carrier concentration depends on the doping level of semiconductors. In addition, the doping level affects the band structure. The donor states appear just below the conduction band for n-type TCOs, and the acceptor levels appear just above the valance band for p-type TCOs up to critical doping levels. In the case of n-type doping, the donor states combine with the conduction band at an absolute

critical value (ηc) for high doping levels. This phenomenon was explained by Mott (Mott, 1956, 1961):

$$n_c^{1/3} a_o^* \approx 0.25 \tag{4}$$

where a_o^* is the Bohr radius, and it is given as:

$$a_o^* = \frac{h^2 \varepsilon_0 \varepsilon^m}{\pi e^2 m_c^*} \tag{5}$$

In Equation 5, h is Planck's constant, ε0 is the permittivity of free space, εm is the static dielectric constant, and m_c^* is the conductivity effective mass.

Intrinsic scattering mechanisms, such as grain boundary scattering, lattice vibration scattering, and neutral and ionized impurity scattering, can affect the mobility of charge carriers. Equation 6 expresses the mobility of charge carriers (μ) (Coutts et al., 2000).

$$\mu = \frac{e.\tau}{m^*} \tag{6}$$

The electronic charge is represented by e, which is the relaxation time, and m^* is the effective mass of the electron. The relaxation time depends on the mean free path (λ) and drift velocity (Vf) as:

$$\tau = \frac{\lambda}{V_f} \tag{7}$$

As mentioned earlier, mobility depends on intrinsic scattering mechanisms, and it can be shown (D. H. Zhang & Ma, 1996):

$$\frac{1}{\mu_{total}} = \frac{1}{\mu_{GB}} + \frac{1}{\mu_L} + \frac{1}{\mu_I} + \frac{1}{\mu_N} \quad (8)$$

where μ_{GB}, μ_L, μ_I, and μ_N are representations of the mobility of grain boundary, lattice vibration, ionized impurity, and neutral impurity scattering, respectively.

1.2.1.1 Grain Boundary Scattering

In polycrystalline semiconductors that especially have small grain sizes, scattering at grain boundaries (GB) is one of the significant scattering mechanisms. Grain boundaries are separation regions of grains that have the same crystal structure but different crystal orientations. TCOs have polycrystalline nature mostly. GBs consist of significant interface states that serve as charge-trapping points. The literature states that oxygen atoms are chemisorbed onto the GBs. Subsequently, these atoms capture electrons from grains forming a negative potential at the GBs and a positive potential in the grain interiors (Seto, 1975).

Consequently, a potential difference is developed between GBs and grain interiors that inhibit electron mobility. Petritz model (Petritz & Kingston, 1956) explains the phenomenon of carrier transport behavior in polycrystalline films. The GB scattering mobility is written using the equation given below:

$$\mu_{GB} = \mu_0 T^{-1/2} \left[-\left(\frac{eV_B}{kT} \right) \right] \quad (9)$$

where μ_0 is a constant that is described as:

$$\mu_0 = \frac{el}{(2\pi m^* k)^{1/2}} \quad (10)$$

e is the electronic charge, m* is electron effective mass, k is Boltzmann constant, T is absolute temperature, V_B is the potential difference between GBs and grain interiors and described as:

$$V_B = \frac{e^2 Q_t^2}{8\varepsilon_0 \varepsilon_r N_d} \tag{11}$$

where Qt is the number of trapping centers, ε0 is the permittivity of free space, εr is the low-frequency relative permittivity, and N_d is the number of ionized donors.

If the electron mean free path and grain size are relatively in the same order, the effect of GB scattering will become more prominent. The mean free path (λ) is calculated by the given relation below (Kittel & Holcomb, 1967):

$$\lambda = V_F \tau = (3\pi^2)^{1/3} \left(\frac{\hbar \mu}{e}\right) n^{1/3} \tag{12}$$

where n is carrier concentration, μ is mobility, and h is Planck's constant.

1.2.1.2 Lattice Vibration Scattering

Lattice vibration scattering is also called acoustic phonon scattering. This type of scattering becomes more dominant when the temperature increases. The mobility of lattice vibration scattering can be derived from the corpuscular model by using deformation potential (Kireev, 1975):

$$\mu_L = \left(\frac{e\pi^2 \hbar^4 c_{11}}{2m^* (2m^*)^{3/2} \Delta_c^2 N}\right) \left(\frac{E^{-1/2}}{k}\right) \frac{1}{T} \tag{13}$$

where c11, Δ and N represent elastic compliance constant, strain divergence, and total matrix atoms concentration, respectively. In degenerate semiconductors, $E=E_F$ is constant. In this case, equation 13 can be written as:

$$\mu_L \propto \frac{1}{T} \tag{14}$$

According to Equation 14, the mobility of lattice vibration scattering is inversely proportional to temperature.

1.2.1.3 Ionized Impurity Scattering

The standard lattice structure of the crystals may contain localized imperfections at single atom positions as point defects. TCOs have point defects due to the oxygen vacancies, excess metal atoms in the undoped films, and many external dopants in the doped films. Point defects are considered as various types as vacancies, interstitials, substitutional defects, and Frenkel and Schottky defects. These defects can be ionized and act as ionized impurities. Generally, TCOs contain a large number of point defects greater than 10^{20} cm^{-3}. However, due to Coulomb's interaction, the ionized impurities are the centers of the scattering for charge carriers, strongly affecting the electrical properties.

Conwell-Weisskoft's expression (Conwell & Weisskopf, 1950) in Equation 15 explains the ionized impurity scattering mobility (μI) that depends on energy. This formula is valid when impurity ions cause the scattering of degenerate charge carriers.

$$\mu_I = \frac{e}{m^*}\tau_i(E_F) = \left(\frac{2}{m^*}\right)^{1/2} \frac{\varepsilon^{1/2} E_F^{3/2}}{\pi e^3 N_i Z^2} \frac{1}{ln\left(1 + \frac{eE_F}{N_i^{1/3} Ze^2}\right)^2} \qquad (15)$$

$\tau_i(E_F)$ represents the relaxation time that is only considered in the scattering action existing close to the Fermi energy level. ε, m*, Ze, and Ni are the static dielectric constant, the effective mass of electrons, the ion charge, and the concentration of the scattering centers, respectively. According to Equation 15, the ionized impurity scattering mobility of the degenerate semiconductors is independent of the temperature.

1.2.1.4 Neutral Impurity Scattering

The neutral impurity scattering mobility exists when the concentration of dopant exceeds the solubility limit in the metal oxide semiconductors. In this case, the dopant element stands inactive and behaves as a neutral impurity by forming various neutral complexes(Frank & Köstlin, 1982). The neutral impurity scattering mobility can be explained by Equation 16 (Shigesato & Paine, 1993).

$$\mu_N = \frac{m^* e^3}{20\varepsilon_0 \varepsilon_r N_N \hbar^3} \tag{16}$$

N_N represents the neutral impurity concentration.

1.2.2 The Optical Properties

The optical and electrical properties of a material are related to each other due to the interaction between electrons of the material and the electric field component of light that the Drude free electron model explains (Drude, 1900). Figure 1.1 demonstrates the common absorption, transmission, and reflection spectrum of TCOs (Pasquarelli et al., 2011).

There is a transmission region in the visible spectra that is considered as λ = 400-750 nm (hv=3.1-1.7 eV) of the electromagnetic spectrum for TCO materials. This region stands between two regions that do not consist of any transmission of photons as a result of dissimilar phenomena. The sudden decline in the transmission and increment in the absorption is observed at shorter wavelengths (λ<λgap). In this region, the photon energy is larger than the band gap of TCO, and photons are absorbed and altered to band-to-band transition. Thus, the photons cannot be transmitted along this region. The second drop in transmission and rise in reflection is observed at longer wavelengths (λ>λp). The region where the absorption is maximum indicates the plasma wavelength (λp) that the light frequency is equal to the frequency of the cumulative oscillation of electrons in the TCO materials.

Absorption is obtained when the oscillation of electrons and the electric field part of the light is in phase. When the wavelength of the light (λ) is smaller than the wavelength of the plasma (λp), the wavefunction shows oscillatory behavior allowing the propagation of light through the material. Thus, the material is observed as transparent. On the other hand, if the wavelength of the light (λ) is larger than the wavelength of the plasma (λp), the wavefunction has deteriorated and prevents light propagation. As a consequence, the incident light is reflected.

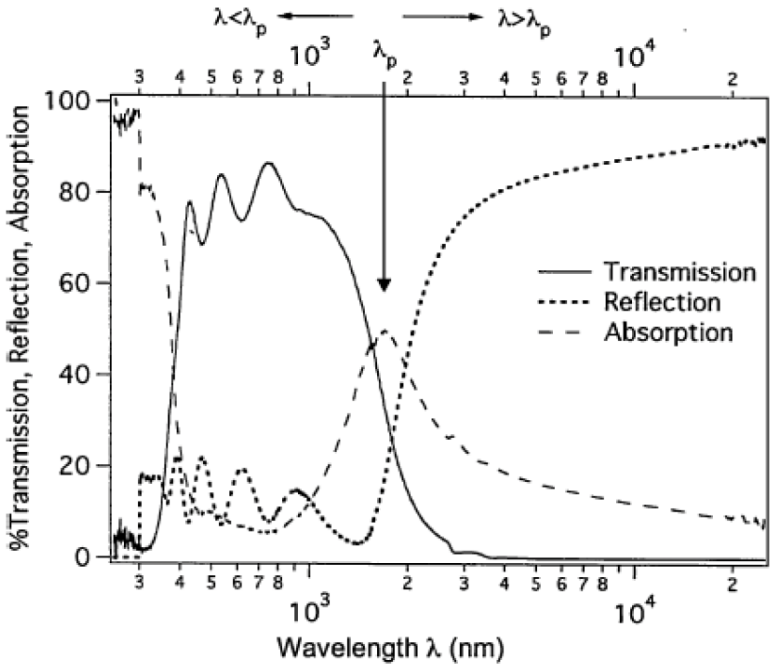

Figure 1.1 The absorption, transmission, and reflection spectrum of TCOs

The behavior of free electrons is described by Drude's free electron model. According to this model, metals and doped semiconductor materials can be considered plasma due to an equal quantity of free electrons and positive ions activated by the electrical part of electromagnetic radiation. The plasma oscillates at the plasma frequency (ωp) and plasma wavelength (λp) (Coutts et al., 2000; Gordon, 2000). The relative permittivity (ε) of the material is affected by the interaction of the electrons with electromagnetic radiation, and it is formulated as follows:

$$\varepsilon = (n - ik)^2 \tag{17}$$

where n is the refractive index and k is the extinction coefficient. The transmission (T), reflection (R), and absorption (A) values are determined through n and k parameters. The n and k parameters are expressed as (Pankove & Kiewit, 1972):

$$n = \sqrt{\frac{1}{2}(\varepsilon_1^2 + \varepsilon_2^2)^{1/2} + \frac{\varepsilon_1^2}{2}} \tag{18}$$

$$k = \sqrt{\frac{1}{2}(\varepsilon_1^2 + \varepsilon_2^2)^{1/2} - \frac{\varepsilon_1^2}{2}} \tag{19}$$

where

$$\varepsilon_1 = \varepsilon_\infty \left(1 - \frac{\omega_p^2}{\omega^2}\right) \tag{20}$$

$$\varepsilon_2 = \left(\frac{\omega_\infty \omega_p^2}{\omega^3 \tau}\right) \tag{21}$$

This model only exists for free electrons and provides the $\frac{1}{\tau} \ll \omega$ relation. Plasma frequency (ωp) is defined as:

$$\omega_p = \left(\frac{ne^2}{\varepsilon_0 \varepsilon_\infty m_c^*}\right)^{1/2} \tag{22}$$

In Equation 22, n is carrier concentration, e is the electronic charge, ε_∞ is the high-frequency permittivity, ε_0 is the permittivity of free space, and m_c^* is the conductivity effective mass.

In the IR range or low-frequency region (ω<ωp or λ>λp), n and k parameters become large values, and materials exhibit unity reflectance. In the visible range or higher frequency region (ω>ωp or λ<λp), n and k become large values and zero,

respectively. In this case, TCO materials exhibit dielectric behavior with maximum transparency (Coutts et al., 2000; Edwards et al., 2004). The TCO films are unsubstantially absorbing materials ($k^2 \ll n^2$) in a transparent regime, and the transmission can be formulated as (Manifacier et al., 1977):

$$T = (1 - R)\, exp(-\alpha d) \tag{23}$$

In Equation 23, R,α and d represent the reflectance at zero-degree incidence, absorption coefficient, and the film thickness. The absorption coefficient is expressed as:

$$\alpha = \frac{4\pi k}{\lambda} \tag{24}$$

R becomes zero at the wavelength near the band gap (λ_{gap}). Tauc relation is used for the determination of the optical band gap, which is given below (Tauc et al., 1966):

$$ahv = \beta\left(hv - E_g\right)^n \tag{25}$$

where is the probability of transition, Eg is the optical band gap energy, and n specifies the band gap as direct or indirect. The value of n becomes 1/2, 3/2, 5/2, etc., for direct bandgap and becomes 2, 3, 5, etc. for indirect bandgap.

The IR absorption edge and UV absorption edge are affected by electron concentration for degenerate semiconductors. When the carrier concentration rises, not only does the band gap (λgap) increase but also the plasma edge (λp) shifts through a shorter wavelength (Coutts et al., 2000). Figure 1.2 gives the reflectance spectrum of TCO materials having a mobility of 100 $cm^2V^{-1}s^{-1}$ with 500 nm thickness (Coutts et al., 2000). A significant increment is observed in reflectance, approaching 90%, for TCO films with large carrier concentrations that rise above plasma wavelength. On the other hand, TCOs with low carrier concentrations do not demonstrate any improvement in reflectance in that range. The interference fringes, reaching a maximum of 15% transmittance, are observed in the visible range.

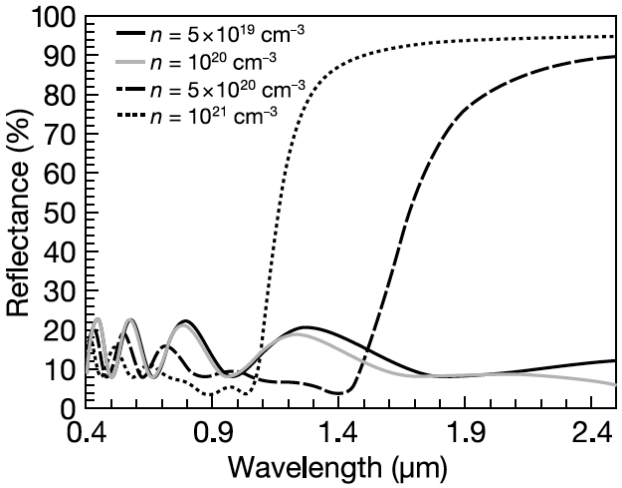

Figure 1.2 The common example of the reflectance spectrum of TCO films (Coutts et al., 2000).

The explanation of the optical band gap widening with increasing carrier concentration is done by the Burstein-Moss (BM) effect (Burstein, 1954). In the degenerately doped TCO materials, the bottom of the conduction band is entirely occupied and causes shifting of the Fermi energy level through the conduction band. Hence, the requirement for the energy that provides electron motion from the valence to the conduction band increases. This widening effect also is influenced by the curvature of conduction and valance bands that are mostly assumed as parabolic. This curvature represents the effective masses of the density of states (DOS). Consequently, both the characteristics and the shape of the bands alter the transition energy of electrons that is requisite for the movement of electrons from the valance to the conduction band, which impacts the width of the band gap. The band structures of undoped and doped TCO films are given in Figure 1.3 (Hamberg et al., 1984).

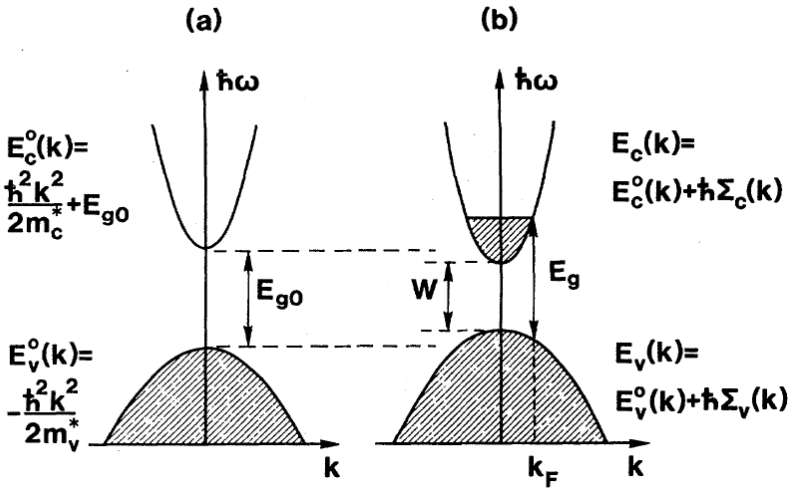

Figure 1.3 An example of the band structures of undoped and doped TCO films (Hamberg et al., 1984).

The formulation of band gap widening due to the BM effect is given as:

$$\Delta E_g^{BM} = E_g - E_{g0} + \frac{h}{2\pi}\Sigma \tag{26}$$

where ΔE_g^{BM}, Eg, Eg0, and $\frac{h}{2\pi}\Sigma$ are the shift in the optical band gap, optical band gap, intrinsic optical band gap, and scattering of electron-impurity and electron-electron, respectively. ΔE_g^{BM} is formulated as:

$$\Delta E_g^{BM} = \frac{h^2}{2m_{CV}^*}(3\pi^2 N)^{3/2} \tag{27}$$

where m_{CV}^* is the reduced effective mass. The m_{CV}^* is calculated by Equation 28.

$$\frac{1}{m_{CV}^*} = \frac{1}{m_C^*} + \frac{1}{m_V^*} \tag{28}$$

In Equation 28, m_C^* is the effective mass of the conduction band density of states, and m_V^* is the effective mass of the valance band density of states.

1.3 Doping Mechanism

The introduction of impurity atoms through the host matrix is called doping. The additional electrons (n-type) or holes (p-type), also called charge carriers, are created by doping. Figure **1.4** shows the doping of the silicon (Callister Jr. & Rethwisch, 2018).

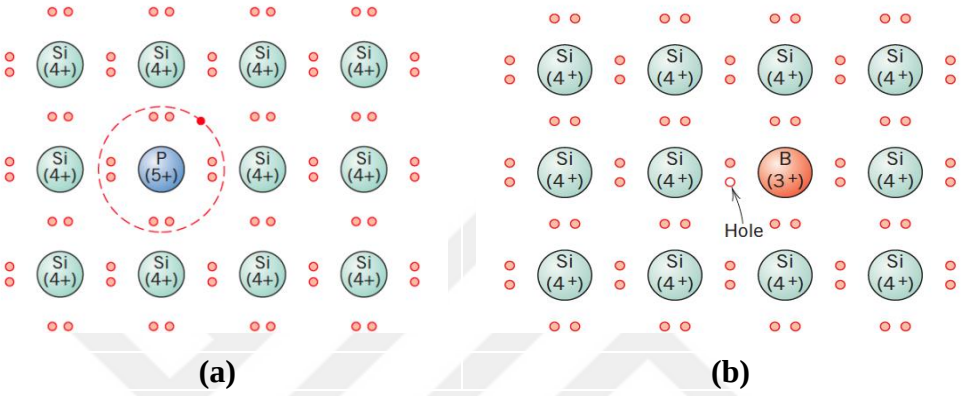

Figure 1.4 The doping of silicon a) n-type doping b) p-type doping (Callister Jr. & Rethwisch, 2018)

Each silicon atom has four valance electrons bonded covalently with neighboring silicon atoms. When an atom that has five valance electrons (i.e., P, As, and Sb) is substituted with one silicon atom, it creates one extra nonbonded electron. This electron becomes a free electron and has a part in the conduction. Now, it is n-type silicon. If an atom with three valance electrons (i.e., Al, B, and Ga) is substituted with a silicon atom, this results in electron deficiency or a hole. The created hole is in the excited state, and it also takes part in the conduction process.

In the case of TCO materials, they can be intrinsic or extrinsic (doped) semiconductors. Intrinsic semiconductors do not have any foreign atoms as dopant. Their native defects, such as interstitials and vacancies, act as dopants.

For example, ZnO is an intrinsic n-type semiconductor due to its interstitial zinc atoms and oxygen vacancies (Jagadish & Pearton, 2006; Özgür et al., 2005). It is challenging to obtain p-type ZnO by introducing impurity atoms (acceptors) by reason of the requirement of high acceptor activation energies and hydrogen impurity atoms behavior that serve as shallow donors in ZnO (Pankove & Kiewit, 1972).

The extrinsically doped n-type ZnO can be achieved by doping with group three elements (Al, Ga, and In). These elements are substituted with zinc atoms, and a free electron reveals (Maldonado & Stashans, 2010). Figure 1.5 illustrates the doping of ZnO by the aluminum atom.

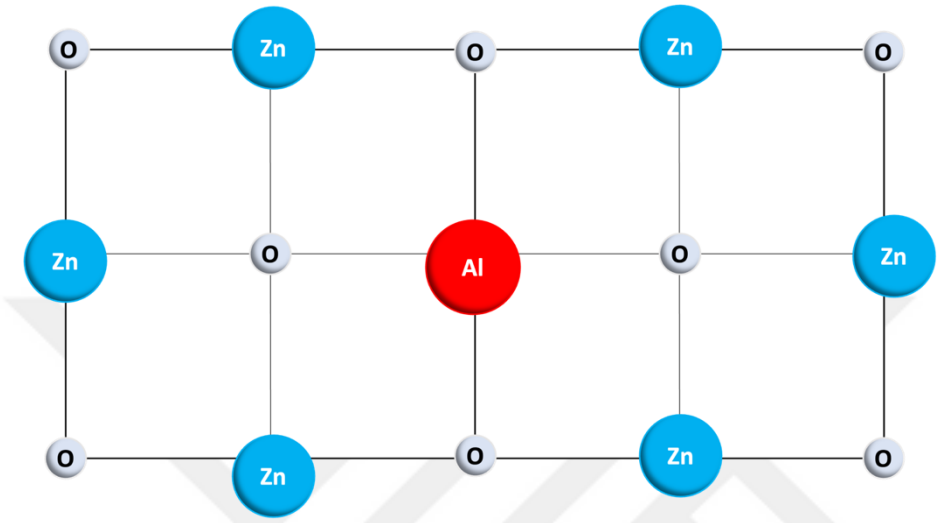

Figure 1.5 The illustration of the 2D lattice of Al-doped ZnO

Also, doping ZnO with halogen atoms (F, Cl, and Br) is another method to obtain n-type doping. In this situation, oxygen atoms substitute with halogen atoms and/or replace with oxygen vacancies. The formation of free electrons is achieved by the substitution process (Y. J. Choi, Kang, & Park, 2015). In Figure 1.6 doping ZnO with a fluorine atom is demonstrated.

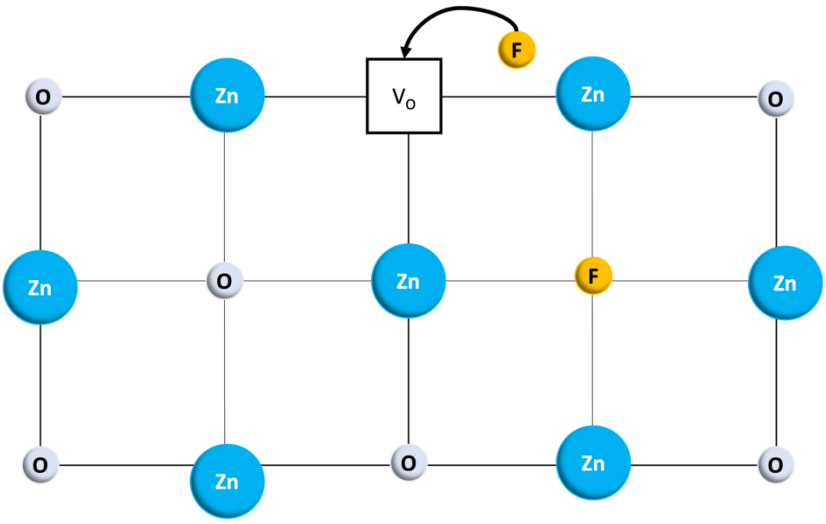

Figure 1.6 The illustration of the 2D lattice of F-doped ZnO

1.4 The Most Used TCO: Indium Tin Oxide Benefits & Drawbacks

Indium tin oxide (ITO) is the mostly used TCO from the development of flat panel displays around the 1970s (White & Feldman, 1970) up to today. The reason behind that is that ITO has the lowest resistivity with high transparency (Huang et al., 2021; Nishinaka & Yoshimoto, 2018).

The crystal structure of indium oxide (In_2O_3) is defined as cubic bixbyite (Ia3), which consists of 80 atoms. It has 32 indium atoms and 48 oxygen atoms. The indium atoms are located in two specific locations with different symmetries. According to locations, indium atoms are separated as In b (8 atoms) and In d (24 atoms) (Marezio, 1966). When the crystal structure of In_2O_3 is examined along the (001) plane, there are three distinct stacking layers the M layer (mixture of In b and In d), the D layer (only In d atoms exist), and the O layer (oxygen atoms). In Figure 1.7. this arrangement of the atoms is shown (Hagleitner et al., 2012).

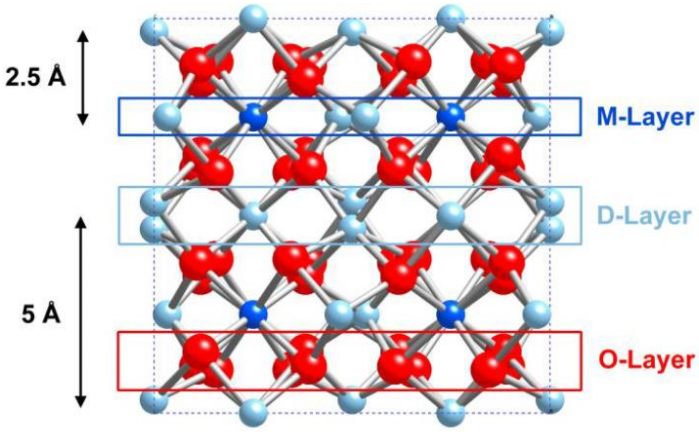

Figure 1.7 The crystal structure of indium oxide along the (001) plane (red balls: oxygen, dark blue balls: In b and light blue: In d)

ITO is obtained by n-type doping of indium oxide via a tin atom. The tin atom with four valance electrons substitutes the indium atom with three valance electrons, forming a free electron. Figure 1.8 shows the representation of the ITO crystal structure (Løvvik et al., 2014).

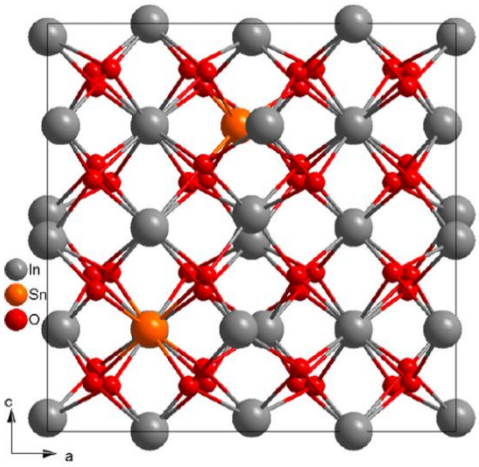

Figure 1.8 The crystal structure of ITO

The band gap of ITO is approximately 3.5 eV. The reason ITO exhibits the highest transparency in visible wavelengths is the formation of a wide band gap between O $2p^6$ and In 5s states. Also, the doping of the In 5s state degenerately via Sn^{+3} donor states provides a large density of free electrons, and as a result of this, ITO permits the most outstanding conductivity (Fan & Goodenough, 1977). The band structure of ITO is illustrated in Figure 1.9.

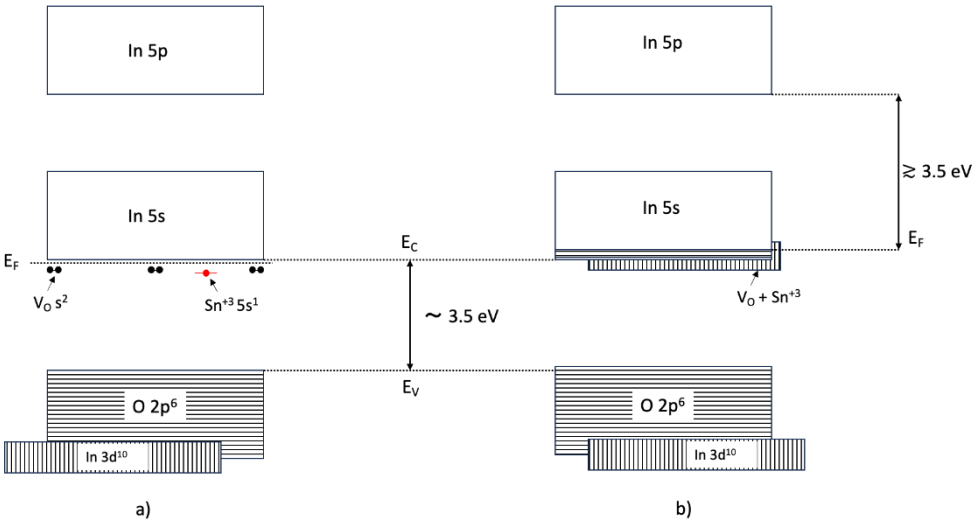

Figure 1.9 The band structure of ITO a) for low doping level b) for degenerate doping

Although ITO still holds its place as the mainly used metal oxide in the TCO market, it has several drawbacks. Most of the known indium and tin reserves are located in China, currently. For this reason, some unforeseen but likely to occur in future geopolitical crises may cause problems in the supply of indium and tin. Also, this geographical instability of mining those metals causes high and volatile market prices, as shown in Figure 1.10. The industries that depend on indium and tin sources are extremely affected by market conditions (*Mineral Commodity Summaries*, 2002; *Mineral Commodity Summaries*, 2007; *Mineral Commodity Summaries*, 2012; *Mineral Commodity Summaries*, 2017; *Mineral Commodity Summaries*, 2022; *Mineral Commodity Summaries*, 2023). Furthermore, lung disorders caused by job-related indium exposure have sharply increased in recent years, primarily from workers in Korea and Japan, some of which have proven lethal (Bomhard, 2018). Hence, the development of new TCOs as alternatives to ITO is requisite.

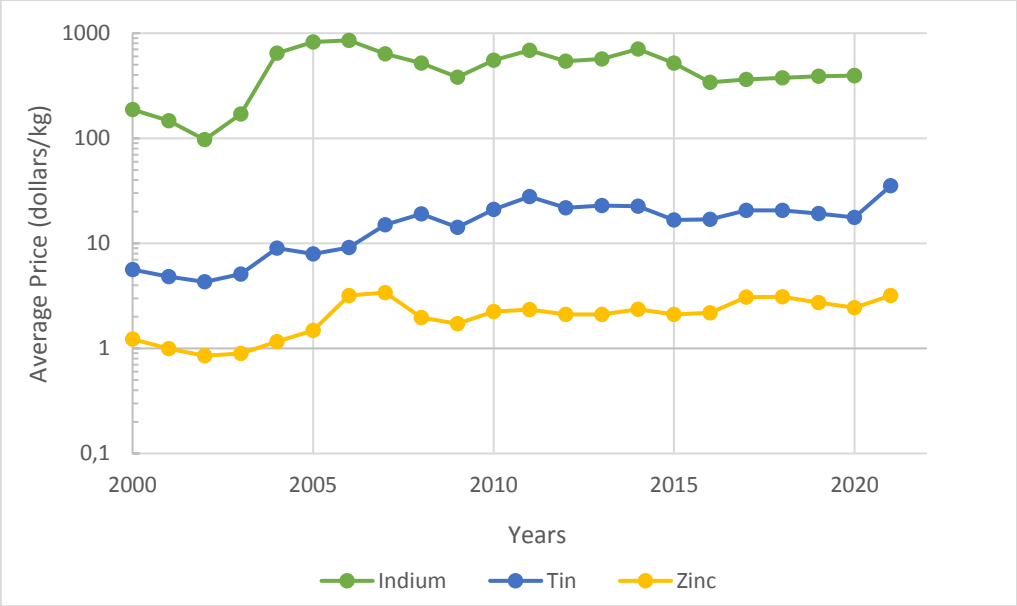

Figure 1.10 The market price comparisons of indium, tin, and zinc for the last 23 years

1.5 The Best Alternative to ITO: Fluorine doped ZnO

1.5.1 Zinc Oxide

The natural abundance of zinc is more remarkable than indium and tin (*Mineral Commodity Summaries*, 2023). Hence, the average zinc price is more stable and considerably low, as seen in Figure 1.10. Also, zinc has additional advantages, such as non-toxicity and easy fabrication (Raha & Ahmaruzzaman, 2022). Thus, zinc-based TCOs can be fabricated at a low cost in large quantities when all benefits of zinc are considered.

Zinc oxide has a thermodynamically stable hexagonal wurtzite structure ($P6_3mc$) that consists of 4 atoms. There are two hexagonal closed-packed sublattices that intersect through each other in this space group ($P6_3mc$). The cations (Zn^{+2}) and anions (O^{-2}) exist in tetrahedral sites (Morkoç & Özgür, 2008). In Figure 1.11. the crystal structure of ZnO is represented.

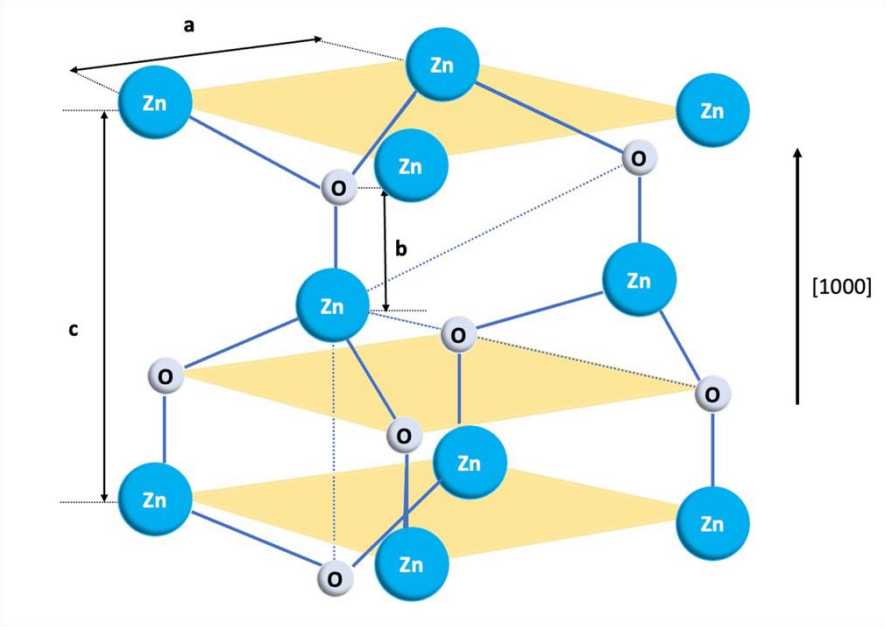

Figure 1.11 The illustration of the ZnO hexagonal wurtzite structure

In the literature, the band gap of ZnO at 4.2 K was reported as 3.437 eV. It is an n-type direct-band semiconductor (Look, 2001). The molecular orbital of ZnO is formed by overlapping of zinc 4s and oxygen 2p atomic orbitals. There is an sp^3 hybridization that results in fully occupied bonding orbitals by electrons and fully unoccupied antibonding orbitals, shown in Figure 1.12. These fully occupied bonding orbitals and fully unoccupied antibonding orbitals create the valance and conduction bands, respectively (Abdelmohsen et al., 2017).

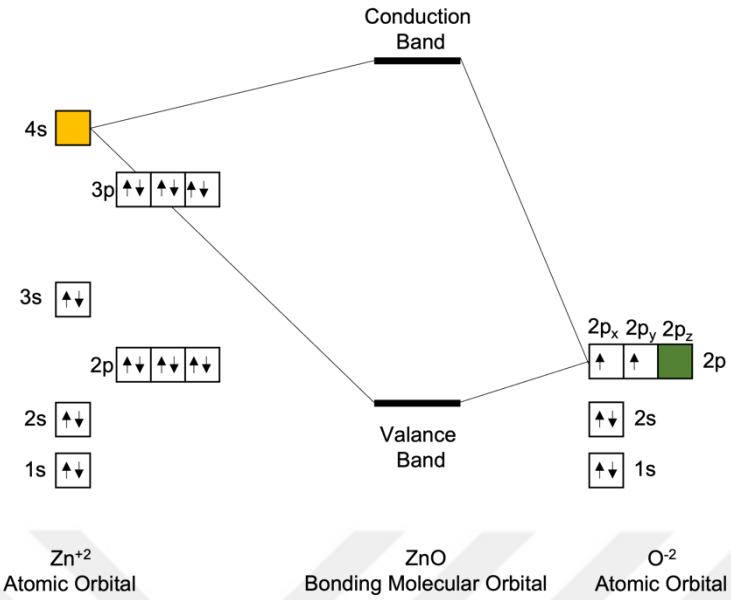

Figure 1.12 The band gap formation of ZnO

The nature of ZnO as an intrinsic n-type semiconductor was explained by the oxygen vacancies and zinc interstitials shown in Figure 1.13 up to recent years.

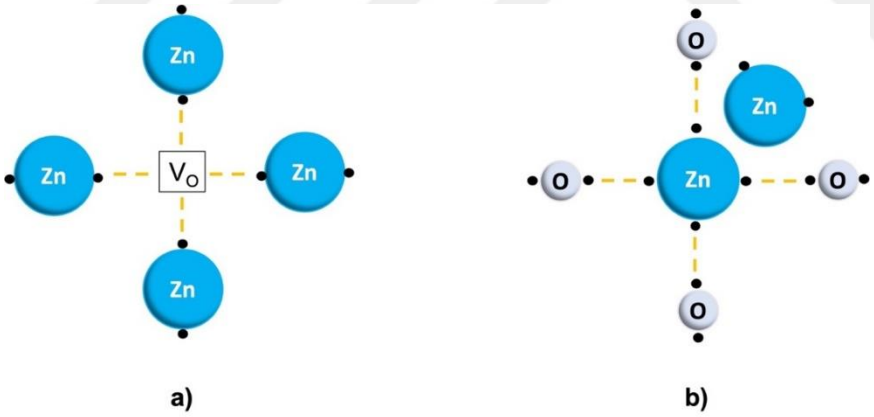

Figure 1.13 The interstitial donor defects of ZnO a) oxygen vacancy b) zinc interstitial

Zinc oxide has several point defects as oxygen vacancies (VO), oxygen intersititals (Oi), zinc vacancies (VZn), zinc intersitials (Zni), oxygen antisites (O_{Zn}), zinc antisites (Zn_O) and impurity atom (e.g., hydrogen and carbon) intersitials or substitions. Janotti A and Van de Walle C ((Janotti & Van De Walle, 2009)) carried out a defect formation energy calculation for these defects with respect to Fermi energy level shown in Figure 1.14. In this graph, zero point indicates valance band

maximum and other side indicates conduction band minimum. Oxygen vacancies (V_O), zinc interstitials (Zn_i) and zinc antisites (Zn_O) are dominated defects under zinc rich region and they appear as donors. On the other hand, zinc vacancies (V_{Zn}), oxygen interstitials (O_i) and oxygen antisites (O_{Zn}) that are observed under oxygen-rich regions behave as acceptors. The formation energies of these defects from lowest to highest are V_O, V_{Zn}, Zn_i, Zn_O, O_i and O_{Zn}, respectively.

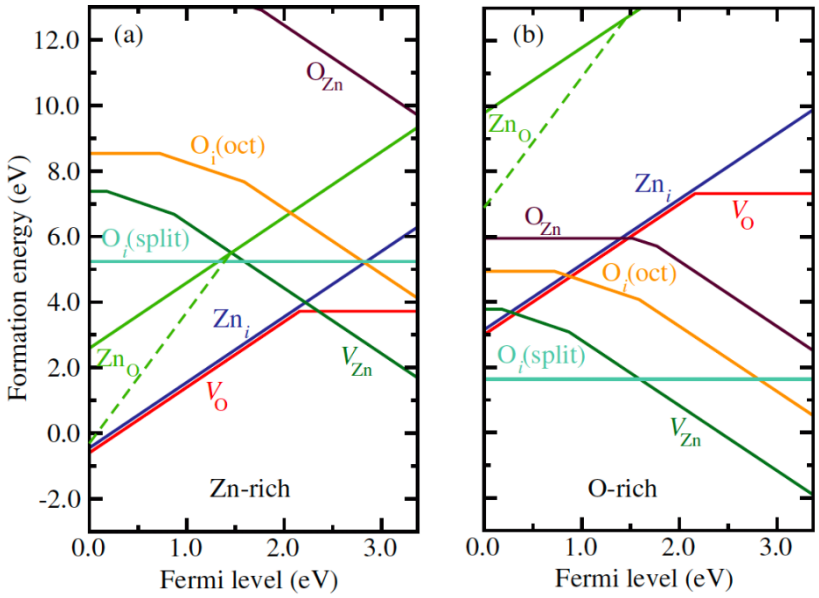

Figure 1.14. The formation energy of ZnO defects with respect to fermi energy level a) Zinc rich region b) Oxygen rich region (Janotti & Van De Walle, 2009).

However, the latest investigations on ZnO defects revealed both oxygen vacancies and zinc interstitials are not responsible for n-type conductivity. These native defects create additional energy levels in the band gap, illustrated in Figure 1.15. The i and V terms indicate interstitial site and vacancy. The dot represents a positive charge, while X represents a zero charge (Schmidt-Mende & MacManus-Driscoll, 2007).

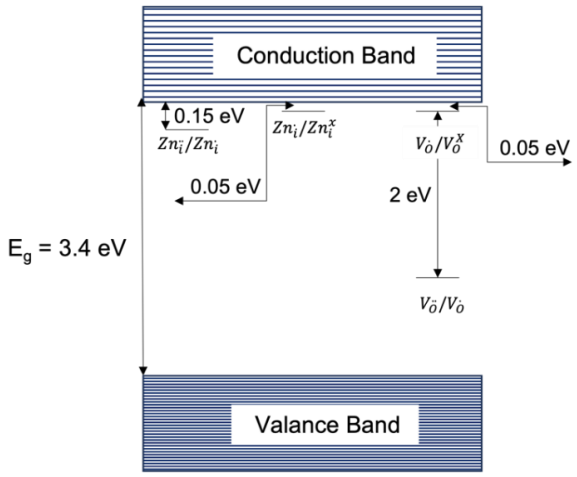

Figure 1.15 The energy band of ZnO with donor defects

Oxygen vacancies (V_O) are present in the deep donor state. They could not contribute to an n-type conductivity, but they compensate p-type doping of ZnO. Even though zinc interstitials (Zn_i) are located at shallow donor states where the fermi energy level (E_f) is close to the conduction band, they have high formation energy. If the E_F is close to the valance band, Zn_i provides compensated p-type doping. Hence, Vo and Zn_i defects do not contribute to n-type conductivity.

The uncertainty of the n-type conductivity of ZnO was tried to explain by hydrogen impurity. The hydrogen impurity in ZnO act as an unintentional dopant and donor source caused by the growth atmosphere. Both interstitial hydrogen and substitutional hydrogen defects have low formation energies shown in Figure 1.16, and that leads to large contents of hydrogen impurities in ZnO. The interstitial hydrogen defects are placed sites near oxygen atoms to form strong O-H bonds. These interstitial hydrogen defects are always showing donor behavior. The hydrogen impurity also can substitute with oxygen in ZnO. These substitutional hydrogen defects are shallow donors. Thus, both interstitial and substitutional hydrogen defects have contributions to n type conductivity of ZnO (Janotti & Van De Walle, 2009).

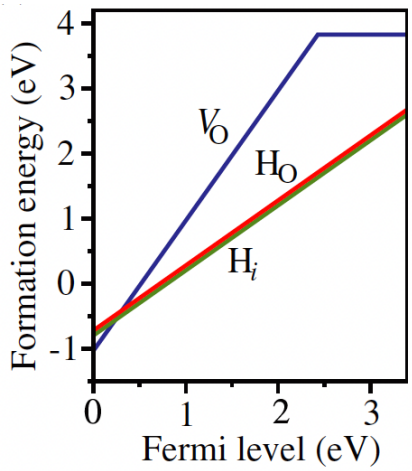

Figure 1.16. The comparison of formation energies of interstitial and substitutional hydrogen and oxygen vacancies with respect to the Fermi energy level under zinc-rich region in ZnO (Janotti & Van De Walle, 2009).

1.5.2 Fluorine doped ZnO (FZO)

The conductivity of ZnO could not achieve the conductivity of ITO, which is commonly in the order of 10^4 S/cm (Gordon, 2000; Minami, 2000). Both electrical and optical properties of ZnO are enhanced by doping, and the doped forms are revealed as indium-free TCOs. The doping mechanism of ZnO is explained in the Doping Mechanism section and shown in Figure 1.5 and Figure 1.6.

The most efficient dopant for metal oxide semiconductors is halogen elements, especially fluorine (F), among the numerous dopant candidates. The ionic radii of fluorine (0.136 nm) and oxygen (0.140 nm) ions are very close to each other, and the electronegativity of fluorine (3.98) is higher than that of oxygen (3.44). Therefore, fluorine easily substitutes oxygen sites (Liu et al., 2010a). As a consequence of substituting fluorine ion with oxygen, an increase in free electrons in the system and a reduction in the electrical resistance of the oxide-based films can be observed (Şennik et al., 2015). In addition, by fluorine doping, defects related to intrinsic oxygen can be eliminated (Xu et al., 2005). In Table 1.3 the doped form of ZnO produced as indium-free TCOs are compared through their electrical and optical properties. According to this comparison, FZO is the best alternative TCO material.

Table 1.3. The comparison of the electrical and optical properties of doped ZnO with ITO

TCO Material	Deposition Technique	Resistivity (Ω.cm)	Carrier concentration (cm^{-3})	Mobility ($cm^2.(Vs)^{-1}$)	Transmission (%) in vis range	References
ITO	DC Magnetron Sputtering	$3.274x10^{-4}$	$8.158x10^{20}$	21.23	~ 79%	(Her & Chang, 2017)
	RF Sputtering	5.52×10^{-4}	$2.27x10^{20}$	30.72	**	(Lebbad et al., 2018)
	MOCVD	$2.8x10^{-4}$	8.9×10^{20}	30	90-100%	(Zhuo et al., 2018)
	ALD	0.015	**	**	> 92%	(Salami et al., 2019)
FTO	APCVD	5.11×10^{-4}	3.91×10^{20}	31.2	> 70%	(Gao et al., 2013)
	Evaporating	1×10^{-2}	0.75×10^{20}	5.9	~ 83 %	(Zhou et al., 2019)
	Mid-frequency pulsed DC magnetron sputtering	67×10^{-4}	1.5×10^{20}	15.1	~ 83 %	(Banyamin et al., 2014)
FZO	APCVD	5×10^{-4}	1.2×10^{20}	40	~ 85%	(Liang & Gordon, 2007)
	Aerosol Assisted CVD	3.70×10^{-4}	5.31×10^{20}	32	~ 76%	(Bhachu et al., 2012)
	PLD	4.83×10^{-4}	5.43×10^{20}	23.8	> 90 %	(Cao et al., 2011)
	ALD	1.876×10^{-3}	1.375×10^{20}	24.20	~ 90 %	(Y. J. Choi & Park, 2014)

Table 1.3 (continued)

AZO	Evaporating	2 x 10^{-3}	7 × 10^{20}	58	~ 80 %	(Ma et al., 2000)
	Solgel	0.27	4 × 10^{15}	26	> 80 %	(Majumder et al., 2003)
	Reactive Magnetron Sputtering	4 x 10^{-4}	4.9 × 10^{20}	35	~ 90 %	(Calnan et al., 2008)
	Hot Wire CVD	1.22 x 10^{-3}	0.99 × 10^{20}	52	~ 90 %	(Abrutis et al., 2015)
	RF Magnetron Sputtering	1.16 x 10^{-3}	4.8 × 10^{20}	11.1	88 %	(Khan & Stamate, 2022)
GZO	PLD	1.4 x 10^{-3}	9.7 × 10^{20}	5	> 80 %	(Mitsugi et al., 2010)
	E beam evaporation	20 × 10^{-4}	**	**	~ 80 %	(Nagarani & Sanjeeviraja, 2011)
	Hot Wire CVD	1.36 x 10^{-3}	1.01 × 10^{20}	45.5	~ 90 %	(Abrutis et al., 2015)
	RF Magnetron Sputtering	1.5 x 10^{-3}	4.5 × 10^{20}	8.9	~ 90 %	(Khan & Stamate, 2022)
	RF Magnetron Sputtering	1.6 x 10^{-3}	6 × 10^{19}	1.7	~ 85%	(Wu et al., 2018)
Cl-doped ZnO	PLD	6.12 x 10^{-4}	5.77 × 10^{20}	17.8	92 %	(J. C. Lee et al., 2013)
	ALD	1.215 x 10^{-2}	5.715 × 10^{19}	31.81	~ 88%	(Y. J. Choi, Kang, Lee, et al., 2015)

The change in electrical and optical properties of FZO films with fluorine concentration that produced by different deposition techniques is given by Table 1.4. The best electrical and optical properties of FZO films were achieved at up to 2 at.%

F doping. The desired electrical and optical properties of FZO films for TCO applications were achieved at up to 2 at.% F doping. The reason behind that is, at low fluorine concentrations, fluorine ions passivate oxygen relevant defects and improve the crystallinity of ZnO (Muhammad et al., 2021; Polydorou et al., 2016). Also, the grain size of ZnO increases up to certain fluorine concentration (Samanta et al., 2022). The larger grains indicate lower grain boundaries and decrease in grain boundary scattering. Hence, the carrier concentration and mobility of FZO films are enhanced by fluorine at low concentrations and whereby the conductivity of films is improved (Pawar et al., 2008). However, towards higher fluorine concentrations, the crystallinity of ZnO decreases. The substitution of fluorine ions with oxygen causes a decrease in the grain size of ZnO. Because of fluorine's diminished effect on ZnO planes through higher fluorine content, the conductivity of FZO films decreases (Gunasekaran et al., 2018; Papari et al., 2017; Sanchez-Juarez et al., 1998). At excessive fluorine concentrations, fluorine atoms present at interstitial sites in ZnO lattice cause a larger density of dislocations (Pawar et al., 2008; Sanchez-Juarez et al., 1998). Thus, the excessive fluorine content causes creation of scattering centers, formation of unwanted compounds, erosion of ZnO planes, and inhibiting n-type doping of ZnO.

Table 1.4. The effect on fluorine doping concentration on electrical and optical properties of FZO films that produced by different deposition techniques.

Deposition Technique	**Fluorine Concentration (at.%)**	**Resistivity (Ω.cm)**	**Mobility ($cm^2(Vs)^{-1}$)**	**Carrier concentration (cm^{-3})**	**Transmission (%)**	**References**
Aerosol Assisted CVD	2	3.70×10^{-4}	32	5.31×10^{20}	~76% at 550 nm	(Bhachu et al., 2012)
RF magnetron sputtering	1.16	0.2	0.3	9×10^{19}	> 80 % in vis range	(X. Zhang et al., 2014)
	1.34	7.66×10^{-2}	0.62	1.31×10^{20}		
	0.99	0.4	0.2	8×10^{19}		
	1.02	1.1	0.08	7×10^{19}		

Table 1.4 (continued)

DC magnetron sputtering	0.81	1.75 x 10^{-3}	40	9.6 x 10^{19}	80.6 % in vis range	(Pham et al., 2021)
	1.27	1.3 x 10^{-3}	45.3	9.8 x 10^{19}	82% in vis range	
	1.91	2.1 x 10^{-3}	37	9.5 x 10^{19}	80.1% in vis range	
	2.5	2.8 x 10^{-3}	12	1.8 x 10^{20}	72.1% in vis range	
ALD	0.2	3.98 x 10^{-3}	43.66	3.589 × 10^{19}	~90	(Y. J. Choi & Park, 2014)
	0.5	3.51 x 10^{-3}	32.49	5.467 × 10^{19}		
	0.7	2.18 x 10^{-3}	25.04	1.243 × 10^{20}		
	1	1.88 x 10^{-3}	24.2	1.375 × 10^{20}		
	1.2	2.19 x 10^{-3}	19.49	1.462 × 10^{20}		
ALD	0.1	4.25 x 10^{-3}	25.2	5.8 × 10^{19}	~90	(Y. J. Choi, Kang, & Park, 2015)
	0.5	2.89 x 10^{-3}	21.9	9.9 × 10^{19}		
	0.7	2.38 x 10^{-3}	18.5	1.4 × 10^{20}		
ALD	0.8	0.4	15	1 × 10^{19}	81.6	(K. M. Kang & Park, 2018)
	0.9	0.08	18	3 × 10^{19}	83	
	1.1	0.06	20	1 × 10^{20}	83.4	
	1.2	0.04	22	2 × 10^{20}	81.5	
	1.3	0.02	24	2 × 10^{20}	80.4	

1.5.2.1 The Defect Mechanism in FZO

The first principal calculation for FZO applied by Lui et al. ((Liu et al., 2010)). In this study, the only identified impurity atom was fluorine. The fluorine impurity could be interstitial or substitutional, like hydrogen atoms. The formation energies of these impurities are shown with respect to fermi energy where (a) is O and F rich region, (b) is O rich and F poor region, and (c) is both O and F poor region in Figure 1.17. The formation energy of F_O is lowest in O poor or Zn rich region (c) when compared with O rich regions (a and b). Accordingly, the required energy for occupation of fluorine ion to oxygen vacancies is relatively low. But F_O has low formation energy in p type ZnO and acts as deep donor in both n and p type ZnO. In addition, F_i can be present in both octahedral and tetrahedral sites of ZnO. However, even in F rich region (a) the formation energy of F_i is high and acts as deep acceptors.

Although F_O acts as donor and F_i acts as acceptor, both have deep states. Because of that they could not provide any conductivity, only compensate p type and n type ZnO respectively. This study concluded that F_O minimizes oxygen vacancies and enchance optical properties. The reason behind improvement of electrical properties of ZnO via fluorine doping explained by saturation of dangling bonds on the surface with fluorine located at grain boundaries (Liu et al., 2010).

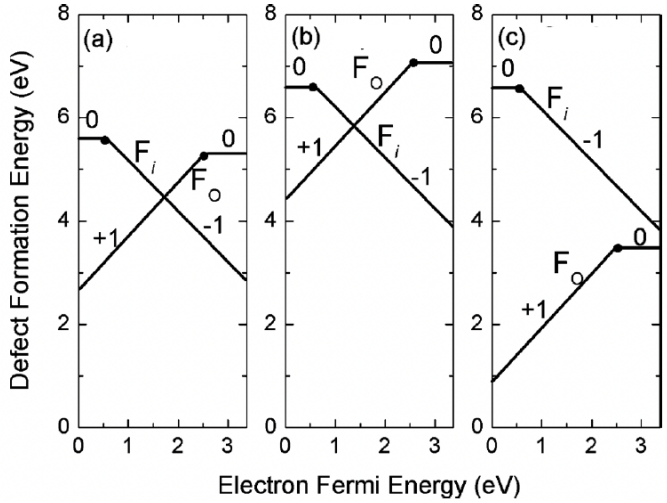

Figure 1.17. The representation of calculated defect formation energies of Fi and Fo (a) in O and F rich region (b) O rich and F poor region and (c) O and F poor region with respect to fermi energy (Liu et al., 2010)

On the other hand, Guo et. al. (Guo et al., 2015) conducted a first principle calculations for intentionally hydrogen doped FZO films. As explained before, unintentional doping of hydrogen is observed in ZnO films because of the growth environment. Thus, this case is more proper even though hydrogen was intentionally doped to FZO. According to this study, hydrogen defects are located oxygen vacancies that far from fluorine substitution to oxygen (H-V_O) , the interstitial sites adjacent to fluorine substitution to oxygen (H_i-F_O) and interstitial sites (H_i-ZnO) as shown in **Figure 1.18** (Guo et al., 2015).

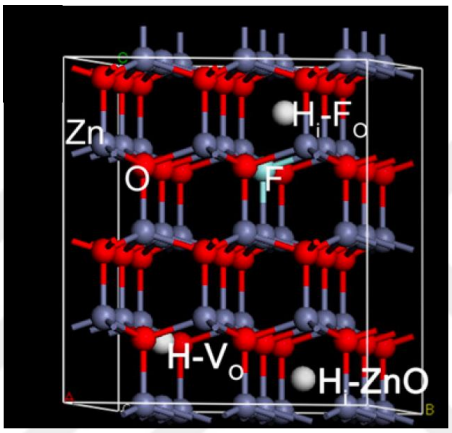

Figure 1.18. The calculated positions of the defects (Guo et al., 2015).

The formation energy of defects with respect to fermi energy are shown in Figure 1.19 for HFZO (Guo et al., 2015). The hydrogen located interstitial sites next to F_O (H_i-F_O) has the lowest energy of formation. Although H-V_O is the most stable in ZnO, in FZO H_i-F_O is the most stable one. In HFZO films both H_i-F_O and H-V_O hydrogen defects are present.

According to this study, H-V_O defect helps to enhance crystallization and act as shallow donors that improve electrical properties. Also, H_i-F_O is a stable defect that contains the electrostatic attraction of fluorine. It is useful for passivation of recombination locations such as grain boundaries. They conclude that the reason behind raise in mobility and conductivity in FZO films is containing stable defects as H-V_O and H_i-F_O(Guo et al., 2015).

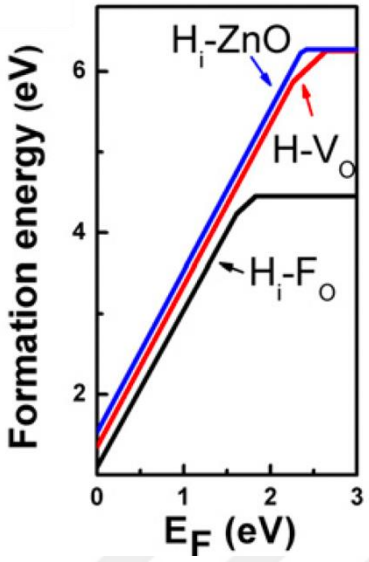

Figure 1.19. The formation energy of defects with respect to fermi energy for HFZO (Guo et al., 2015).

1.6 The Deposition Techniques of FZO

The properties of FZO entirely depend on fabrication methods, as with all TCO materials. From the materials science point of view, these fabrication processes lead to an extensive variety of carrier concentrations and band gap values that affect both conductivity and transmittance of these oxides.

The deposition of FZO thin films has been conducted by various physical vapor deposition techniques such as sputtering (Tsai et al., 2009), pulsed laser deposition (Cao et al., 2011), electron beam evaporation (Xu et al., 2005), and chemical methods such as solution-based spray pyrolysis (De La et al., 2002) and chemical vapor deposition (CVD) (Hu & Gordon, 1991).

Physical vapor deposition (PVD) techniques consist of the vaporization of atoms or molecules from a source that can be solid or liquid, transportation as a vapor form in a vacuum environment (10^{-5}-10^{-9} Torr), and condensation on the surface of the substrate (Mattox, 2002). Even though FZO films produced by PVD techniques have remarkable electrical and optical properties, such as resistivities lower than $8x10^{-4}$

Ω.cm and transmittance in visible light higher than 85%, there is a necessity for additional oxidation or post-annealing processes (Tsai et al., 2009; Xu et al., 2005).

The spray pyrolysis method is based on the spraying of a solution on the heated surface of the substrate and forming a layer of desired chemical compounds through the reaction of the components (Lončarević & Čupić, 2019). The resistivity values of the films deposited by spray pyrolysis have varied from 10 to 10^{-2} Ω.cm (Hu & Gordon, 1991; Hurma & Caglar, 2020). Although spray pyrolysis is a relatively cheap and easy method, the films produced by this method cannot provide the required electrical properties for TCO applications.

In the chemical vapor deposition (CVD) process, volatile precursors are vaporized in a bubbler at high temperatures, then transported by a carrier gas onto the heated surface of the substrate. These precursors are finally subjected to a chemical reaction, resulting in the formation of a thin film (Pierson, 1992). In literature, the lowest resistivity of CVD-grown FZO film was reported as $4x10^{-4}$ Ω.cm with a mobility of 40 $cm^2 V^{-1}s^{-1}$. However, this film was deposited above 450 °C (Hu & Gordon, 1991).

Atomic layer deposition (ALD) is a CVD-like thin film deposition technique with self-limiting surface reactions. The self-limiting reactions occur between gaseous reactants, also known as precursors and active sites of the surface. The precursors are isolated from each other via purging with inert gas to provide a surface reaction only (Suntola, 1989). There are two different ALD systems as plasma ALD and thermal ALD. In the literature, there are only three studies on ALD-grown FZO, and the lowest resistivity is 1.876 x 10^{-3} Ω.cm with 24.2 $cm^2 V^{-1}s^{-1,}$ and it has above 90% transmission at the visible range (Y. J. Choi & Park, 2014).

ALD is an excellent thin film deposition technique for micro and nanoelectronics because of its ability to provide conformal coverage over complex-shaped surfaces, production of highly uniform films at low temperatures, and sub-nanometre thickness control (Leskela & Ritalä, 2002). In Table 1.5 a comparison of ALD with PVD and CVD techniques is given.

Table 1.5. The comparison of the deposition techniques

	Deposition Techniques		
Properties	**CVD**	**PVD**	**ALD**
Low coating temperature		✓	✓
No requirement for ultra-high vacuum	✓		✓
Low installation and maintenance cost			✓
Good film coverage	✓		✓
Large area uniformity	✓		✓
Highest deposition rate	✓		
Reproducibility	✓		✓
Suitable for polymeric substrates		✓	✓

Within the scope of this study, FZO films were produced by thermal ALD and attempted to improve the optoelectronic properties of the produced films.

1.7 Atomic Layer Deposition

The atomic layer deposition (ALD) technique was introduced during the 1960s by Russian scientists as "molecular layering." In this study, layer-by-layer growth by using sequential surface reactions was demonstrated for the first time (Shevjakov et al., 1965). Later, this technique was reported and patented as “atomic layer epitaxy” (ALE) by Dr. Tuomo Suntola and Dr. Jorma Antson in the late 1970s (Suntola & Antson, 1977). These two pioneering studies impact the improvement and commercialization of ALD. Today, ALD has become a vital film deposition

technique utilized in various industries such as catalysis, electronics, energy storage, etc.

A cycle of ALD consists of the introduction of reactive gases into a reaction chamber sequentially, chemisorption of reactants onto the heated substrate surface, the separation of these gases and prevention of physisorbed unwanted by-products and excessive precursors by inert gas purges, self-limiting reactions between reactive gases, and as a result formation of an atomic layer. The thickness of the films is controlled precisely by reason of a certain deposition rate per cycle. Due to a self-limiting reaction mechanism, molecules are only absorbed by unoccupied sites, and it provides conformal coverage. The ALD-grown films have a tendency to be pinhole-free and continuous (George, 2010; Suntola, 1989).

For example, one cycle of ZnO deposition by ALD is given in Figure 1.20. As an oxygen source, deionized (DI) water (H_2O) and as a zinc source, diethyl zinc (DEZ) ($(C_2H_5)_2Zn$) is used. Firstly, the DI water is pulsed and reacts with the hydroxyl groups on the substrate surface (Figure 1.20 a.). Then, by-products and physisorbed surface species are evacuated by inert gas from the chamber. This step is called purging (Figure 1.20 b.). DEZ is pulsed and reacts with the surface chemisorbed species, and by-products and physisorbed surface species are purged again (Figure 1.20 c.). As a result of these steps, one ZnO layer is formed (Figure 1.20 d.). The reaction cycle can be repeated Until the desired thickness of the layer.

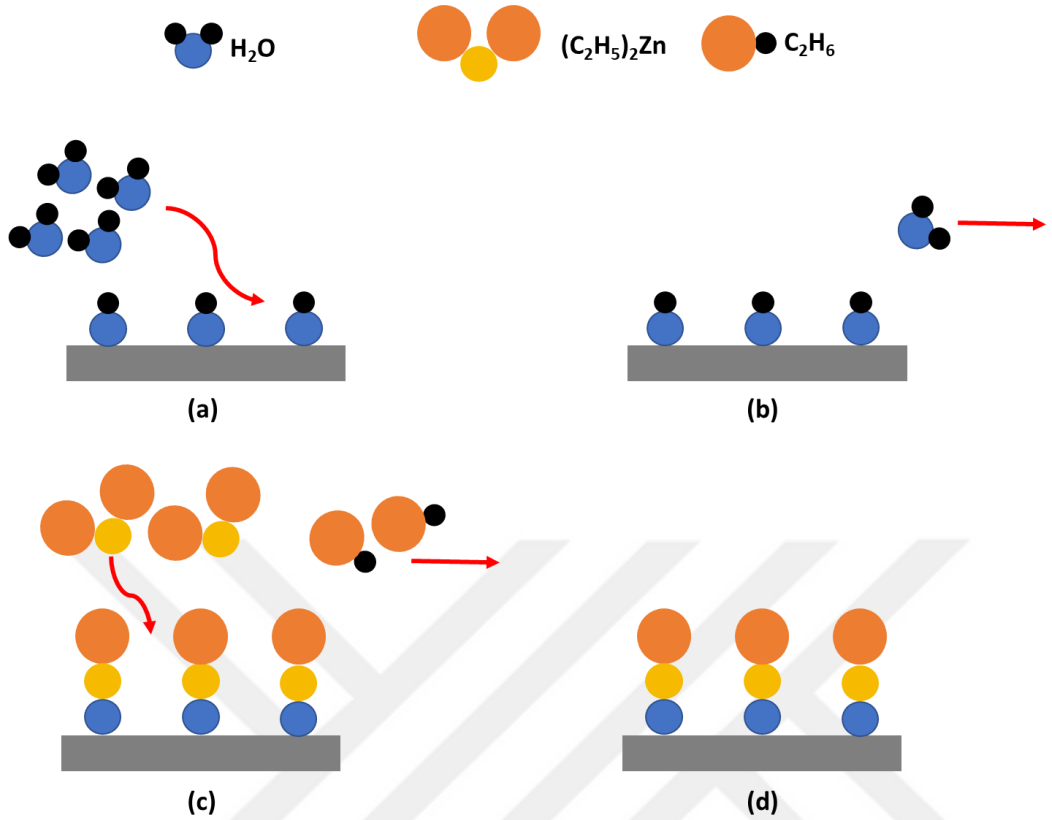

Figure 1.20 A cycle of ZnO deposition via ALD

The chemisorption mechanism consists of three aspects: ligand exchange, dissociation, and association, as shown in Figure 1.21. The ligand exchange can be considered a split of a reactant molecule and a reaction of one of its ligands with the surface species. Then the remaining ligands from the reactant react with the surface site and are coupled with the remaining surface species. The byproducts that are formed during the reaction are eliminated by purging. The molecule that is obtained consequent on the reaction is chemisorbed onto the surface of the substrate. In specific situations, ligand exchange can be observed between surface-bounded molecules and surface species. In this case, the reaction occurs between the two surface-bounded molecules resulting in a byproduct releasing in a gas phase. However, due to this reaction, no new metal species are binding to the surface. Dissociation takes place when the reaction molecules are split apart and, afterward, connect with the reaction sites on the surface. Association occurs when adsorbed species are very close to each other and form new chemical bonds with reactions. In this case, no gaseous byproducts and ligands are released (Puurunen, 2003).

The growth per cycle (GPC) is inversely proportional to both the amount and size of the ligands. Since the reaction equilibrium can be attained by eliminating gaseous byproducts by purging, the ligand exchange is commonly regarded as the preferred reaction approach (Puurunen, 2003).

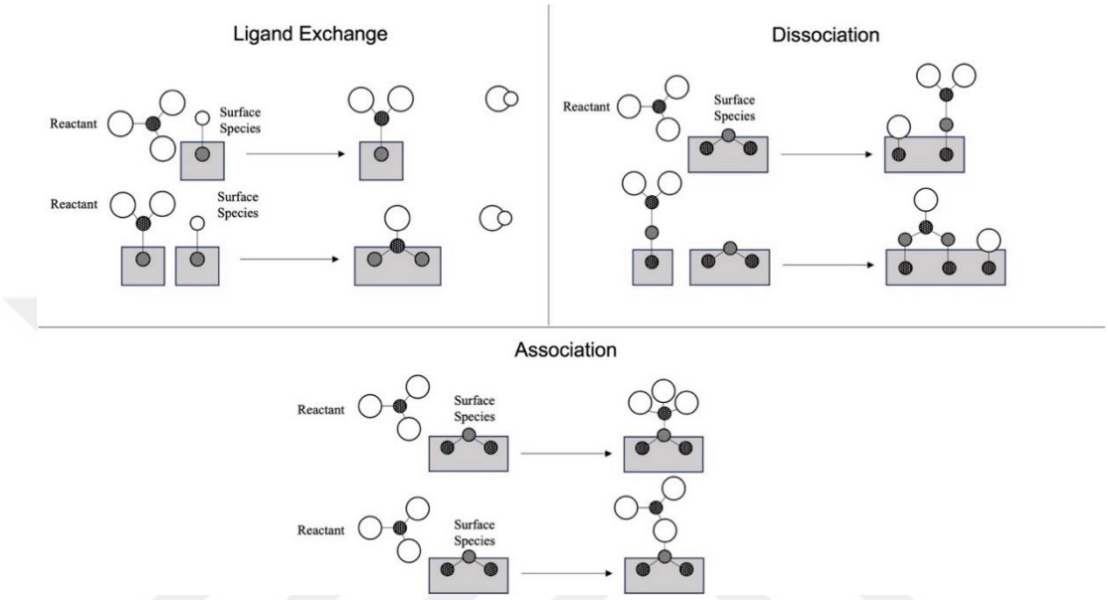

Figure 1.21 The illustration of potential chemisorption mechanisms in ALD

In the ALD technique, thin films are deposited at low temperatures as 50-300°C (Min et al., 2010; Profijt et al., 2011). The GPC is frequently related to growth temperature, as shown in Figure 1.22 (Tomer et al., 2021).

ALD behavior is observed only in the ALD window where the self-limiting growth is observed. In this region, the growth rate does not change with the temperature, and deposition of a monolayer per cycle is achieved.

At low temperatures, the growth rate is low because the activation energy required for completing the reaction is not sufficient, and the reactants desorb from the substrate surface. Also, low temperatures may lead to condensation of desorbed molecules on the surface of the substrate, and an increase in the growth rate can be observed.

High temperatures can cause the desorption of the first reactant from the substrate surface before the pulsing of the second reactant through the surface, and the growth rate reduces. Also, the first reactant's adsorption and the second reactant's

decomposition in the gas phase may occur earlier than any reaction is obtained. This results in the deposition of the first reactant onto the substrate surface without a self-limiting regime, and the growth rate increases (Kääriäinen et al., 2013).

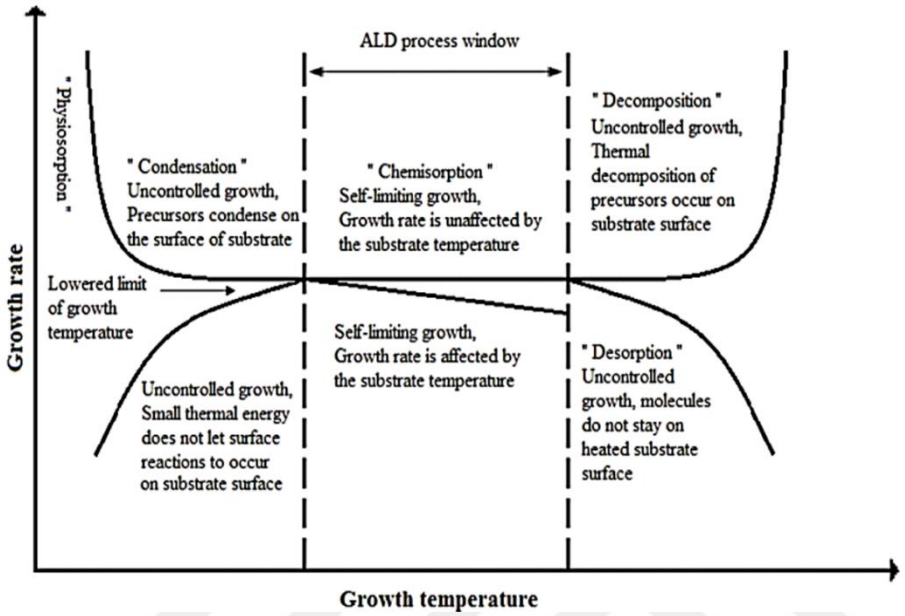

Figure 1.22 The growth behavior of the thin films in ALD (Tomer et al., 2021)

1.8 ALD Grown FZO by NH_4F

The NH_4F dissolve in water as:

$NH_4F + H_2O \leftrightarrow NH_4OH + HF$

$HF \leftrightarrow H^+ + F^-$

$NH_4OH \leftrightarrow NH_3 + H_2$

The possible half reactions after DEZ and NH4F/DI mixture pulses as:

-DEZ Pulse:

$Si\text{-}H^* + Zn(CH_2CH_3)_2 \rightarrow Si\text{-}ZnCH_2CH_3^* + C_2H_6$

-NH4F/DI mixture Pulse:

$Si\text{-}ZnCH_2CH_3^* + NH_3 \rightarrow Si\text{-}ZnNH_2^* + C_2H_6$

$Si\text{-}ZnCH_2CH_3^* + H_2O \rightarrow Si\text{-}ZnOH^* + C_2H_6$

$Si\text{-}ZnCH_2CH_3^* + HF \rightarrow Si\text{-}ZnF + C_2H_6$

Although, all half reactions in NH4F/DI mixture pulse thermodynamically favorable, ZnF and $ZnOH^*$ species replace ethyl group on surface easily than $ZnNH_2^*$. Nitrogen doping can affect the n type doping destructively. But this reaction is less thermodynamically favorable (Y. J. Choi & Park, 2014; Dong et al., 2009).

1.9 The Characterization of ALD-grown FZO Films

The characterization techniques and applications used in this thesis are given in Table 1.6.

Table 1.6 The characterization methods and their usage for ALD-grown FZO films.

The Characterization Technique	Application
Grazing Incidence X-ray Diffraction (GIXRD)	Identifying the crystal phases of produced films
Secondary Ion Mass Spectrometry (SIMS)	Analyze the composition of films by depth
X-ray Photoelectron Spectroscopy (XPS)	The compositional analysis of the surface of the films
Spectroscopic Ellipsometry (SE)	Measuring the refractive index and thickness of the films
Hall Measurement	Measuring the resistivity, mobility, and the carrier concentration
UV-Vis Spectroscopy	Measuring the optical transparency of the films in the UV-VIS spectra

1.10 Motivation of Thesis

In this work, in-situ fluorination of ZnO films was conducted in ALD using a new homemade precursor, a mixture of ammonium fluoride (NH_4F/H_2O) solution, as a fluorine source for the first time in literature. Ammonium fluoride (NH_4F) is not as strong an acid as HF, and when it is used in low concentrations, there is no requirement to make any adjustments in the parts of the ALD system. The practical and economic advantages can be obtained in this way.

CHAPTER 2

EXPERIMENTAL PROCEDURE

2.1 Experiment Details

In this study, FZO films were grown over silicon (p-type SSP (100)) wafers by the OkyayTechALD reactor shown in Figure 2.1.

Figure 2.1 The ALD system used in the thesis

All experimental procedure is summarized in Figure 2.2.

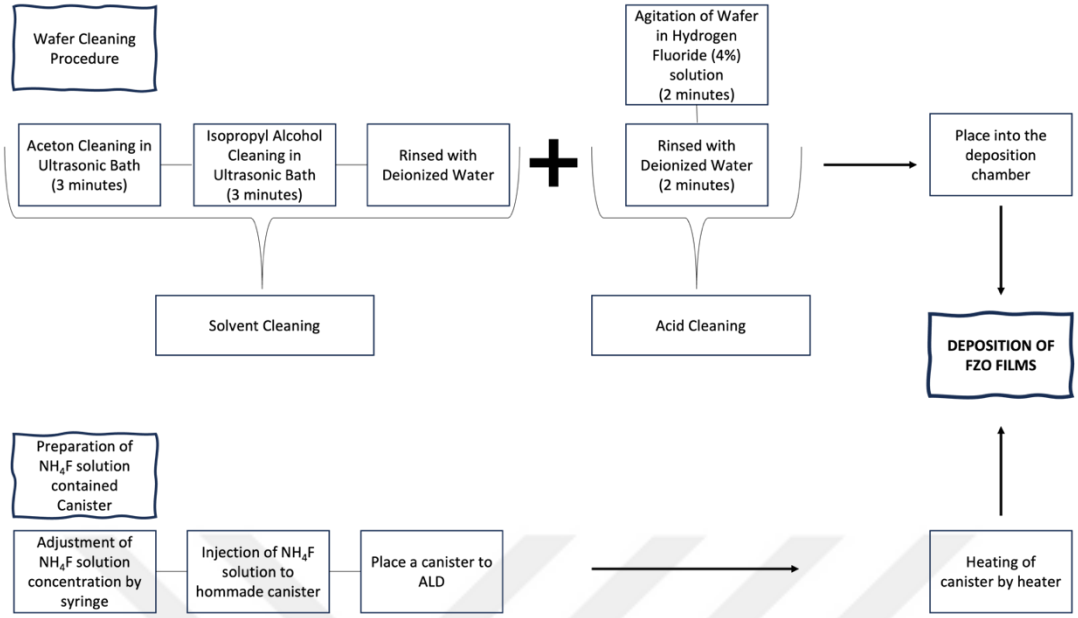

Figure 2.2 The summary of the experimental procedure

The wafers were cleaned with acetone (≥99.9%), ethanol (≥99.9%), and deionized (DI) water in an ultrasonic bath before the deposition, respectively. In order to remove the native oxide layers on the wafers, a 4% hydrofluoric acid (HF)/DI water solution was used. All cleaning procedure steps are shown in Figure **2.3**.

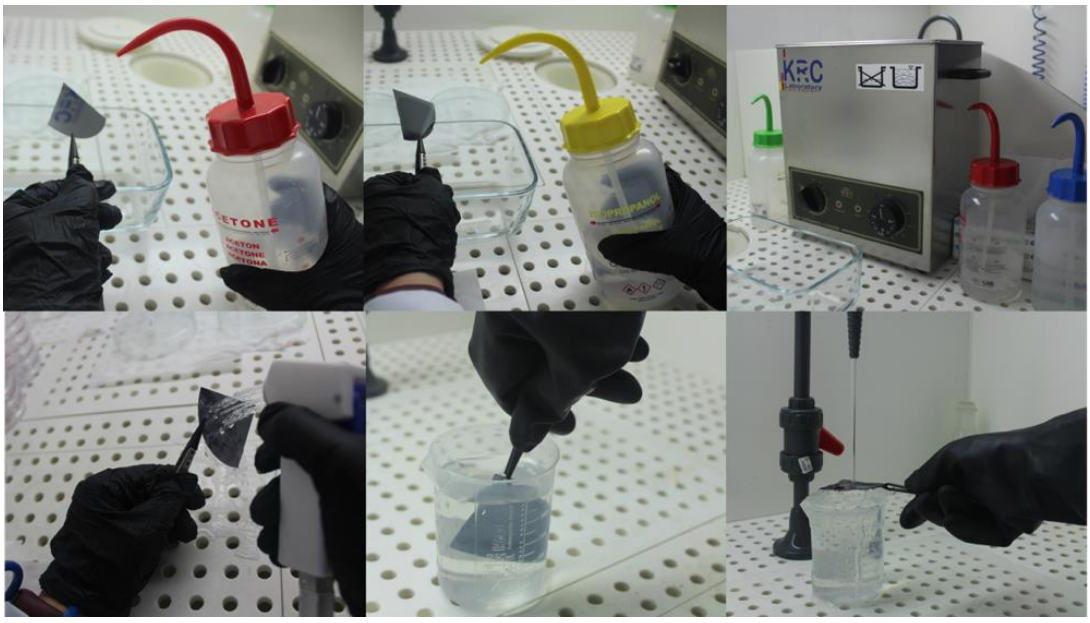

Figure 2.3 The cleaning procedure of the Si wafer

The precursors that are used in ALD must have certain properties as volatility, reactivity, thermal stability, purity, forming volatile and unreactive byproducts, cheap and not etch of the substrate and the produced film etc. Only Park et al. achieved to produce FZO thin film via ALD by using hydrofluoric acid (HF) and deionized (DI) water (Y. J. Choi, Kang, & Park, 2015; Y. J. Choi & Park, 2014; K. M. Kang & Park, 2018). However, HF is an extremely corrosive material, and there is a necessity for a protective coating such as Teflon for all parts of the ALD system that will come into contact with HF (Park et al., 2015). Thus, a new fluorine-based precursor must be introduced to both cause any impurities and corrosion.

In this study, for fluorine and oxygen source NH_4F/DI water mixture was used as precursor. NH_4F solution has several advantages as weaker acid than HF, the vapor pressure is close to water, easy to handle etc. In order to compare etching rate of NH_4F with HF an experiment was designed. ALD grown ZnO films on Si substrate with 100 nm thicknesses were etched by different NH_4F concentration as 1%, 5% and 10% for a minute. After that, the thickness difference was measured by DEKTAK.

The etch rate of HF on AZO film (Al content is about 3 at.%) (Owen et al., 2012) and the etch rate of NH_4F on ZnO film are given in Table 2.1 and

Table **2.2**. The concentration of 0.125 % HF has the same etch rate as 10% NH_4F. Thus, as a new fluorine-based precursor NH_4F is suitable for ALD.

Table 2.1. The etch rate of HF on AZO film (Owen et al., 2012)

Film	**HF concentration (%)**	**Etch rate (nm/s)**
AZO	0.125	1.1
	0.25	1.1
	0.5	1.2
	1	1.4

Table 2.2. The etch rate of NH_4F on ZnO film (In this study)

Film	**NH_4F concentration (%)**	**Etch rate (nm/s)**
ZnO	1	0.5
	5	0.8
	10	1.1

Diethylzinc (Sigma-Aldrich, Inc.) as a zinc source and a mixture of NH_4F/DI water solutions with different concentrations (20-40% NH_4F) as both fluorine and oxygen sources were used. As a carrier gas, N2 (≥99.99%) was used with of 20 sccm flow rate. The pulse time for DEZ and NH_4F/H_2O solution was selected as 100 ms to achieve the surface saturation. Nitrogen purge time was chosen as 10s. Before the deposition process, some of the canister containing a mixture of NH_4F/H_2O solution was heated to 40 °C, 50 °C and kept at this temperature during the deposition. Films were grown at various temperatures between 160°C-200°C.

The preparation steps of NH_4F/DI water solutions and the canister heater system are shown in Figure 2.4. 40% NH_4F solution (Honeywell Fluka) was used. The concentration of prepared solutions is calculated by Equation 29 where C_1 is 40% as concentration of NH_4F solution, V_1 is volume of NH_4F solution, C_2 is desired concentration of NH_4F solution and V_2 is volume of final solution. The concentration of prepared solutions, volume of 40% NH_4F solution and DI water are given in Table 2.3.

$$C_1 \, x \, V_1 = \, C_2 \, x \, V_2 \tag{29}$$

Table 2.3. The NH_4F/DI mixture concentration, volume of 40% NH_4F solution and DI water

NH_4F/DI Mixture (%)	**40% NH_4F (mL)**	**DI Water (mL)**
1	0.5	19.5
5	2.5	17.5
10	5	15
20	10	10
30	15	5
40	20	0

Figure 2.4 The NH_4F/DI solution adjustments for each experiment and the heater system for the canisters

The experiments conducted for this thesis are given in Table 2.4. The samples were named as deposition temperature/ NH4Fconcentration / canister temperature respectively. As an example FZO(160/1/50) sample were deposited at 160 °C with 1%NH_4F concentration and the canister held to 50 °C during deposition.

Table 2.4 The experiments and their deposition conditions

Sample I.D.	Temperature (°C)	NH4F concentration (%)	Precursor Temp. (°C)	Cycle ZnO:ZnO/F	Cycle
FZO(160/1/50)	160	1	50	0:1	300
FZO(180/1/50)	180				
FZO(160/5/RT)	160	5	RT		
FZO(160/5/50)	160		50		
FZO(180/5/50)	180				
FZO(160/10/50)	160	10	50		
FZO(160/20/50)	160	20			
FZO(180/20/50)	180				
FZO(200/20/50)	200				
FZO(160/30/50)	160	30	50		
FZO(180/30/RT)	180		RT		
FZO(180/30/40)	180		40		
FZO(180/30/50)	180		50		
FZO(200/30/50)	200				
FZO(160/40/50)	160	40			
FZO(180/40/50)	180				
FZO(200/40/50)	200				

2.2 Characterization Techniques

Grazing Incidence X-ray diffraction (GIXRD): The structural analysis was done by GIXRD measurement. The measurements were carried out by CuKα radiation with 40 kV and 30 mA. The scan range was chosen as 25º-65º(2θ) with 1º/min scan speed with fixed angle as 0.3º.

XPS: The spot size of X-ray was 400 μ and flood gun was open during the analysis. High resolution (HR) mode was used. F1s, survey, F1s, Si2p, C1s, Zn2p and O1s was done respectively. Partial scan for F1s, Si2p, C1s, Zn2p and O1s was conducted

with 50 eV pass energy, 50 ms dwell time and 0.1 eV step size. Survey scan was conducted with 200 eV, pass energy, 50 ms dwell time and 1 eV step size. After the collection of data from both partial and survey scan, etching was applied to the surface for the removal of carbon on the surface. For etching, 1000 eV with high current during 120 s was used.

SIMS: O_2 gun was used to detect Si and Zn. The emission of O_2 gun 10 mA with 4000V ion energy and the sensitivity of the detector was 100 nA/V. The chamber pressure was $4.5x10^{-9}$ Torr before the analysis. During the analysis pressure of the chamber $1.3x10^{-8}$ Torr. Cs gun was used to detect Si,F,O and C. The emission of Cs gun 2.19 mA with 5000V ion energy and the sensitivity of the detector was 10 nA/V. The chamber pressure was $7.2x10^{-9}$ Torr before the analysis. During the analysis pressure of the chamber $1.7x10^{-8}$ Torr.

Hall Measurement: The Hall mobility, carrier concentration and resistivity of the films were measured by Hall measurement system by using van der Pauw Method at the room temperature. Aluminum was coated by evaporation technique (around 35 nm) onto the edge of films grown on quartz substrate. The magnetic field was 2000 Gauss.

Ellipsometry: The thickness of films grown on quartz substrate was determined by ellipsometry.

DEKTAK: The thickness of films grown on silicon substrate was determined by DEKTAK.

UV-VIS: The transmittance and absorbance of the films at 190-1000 nm region were measured.

CHAPTER 3

RESULTS AND DISCUSSION

3.1 Effect of Canister Temperature on Fluorine Doping

The effect of canister temperature on fluorination was observed by experiments given in Table 3.1.

Table 3.1. The experiments that conducted to identify effect of canister temperature on fluorine doping.

Sample I.D.	Temperature (°C)	NH_4F concentration (%)	Precursor Temperature (°C)	Cycle ZnO:ZnO/F	Cycle
FZO(160/5/RT)	160	5	RT	0:1	300
FZO(160/5/50)			50		
FZO(180/30/RT)	180	30	RT		
FZO(180/30/40)			40		
FZO(180/30/50)			50		

3.1.1 Effect of Canister Temperature on Structural and Compositional Properties at 160 °C with 5% NH_4F/DI mixture

Firstly, at 160 °C, the canister with 5% NH_4F/DI concentration was used to produce FZO films held at room temperature, and the other was heated up to 50 °C and held at that temperature during the process. The XRD patterns of FZO(160/5/RT) and

FZO(160/5/50) are given in Figure 3.1. The XRD pattern of FZO(160/5/RT) and FZO(160/5/50) and information of XRD patterns are tabulated in Table 3.2. The grain size (D) was calculated from The Debye Scherrer equation ($D(2\theta)=K\lambda/\beta\cdot\cos\theta$).

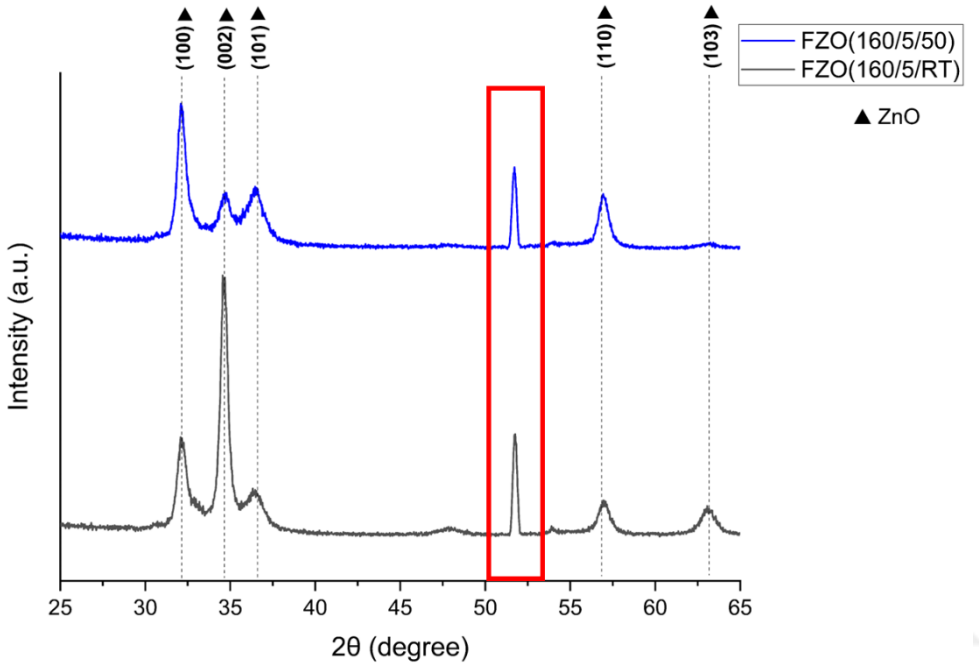

Figure 3.1. The XRD pattern of FZO(160/5/RT) and FZO(160/5/50)

Table 3.2. The 2 Theta positions, planes, crystal size (D), d spacing, dislocation density and internal stress of FZO(160/5/RT) and FZO(160/5/50)

Sample I.D.	2 THETA (°)	FWHM	Peak Intesity	D (nm)	d-spac.	disloc. den.	internal stress (GPa)
FZO(160/5/RT)	32.11	0.58	293	14.3	2.79	0.005	2.00
	34.62	0.49	998	16.9	2.59	0.003	1.15
	51.71	0.22	507	39.8	1.77	0.001	
FZO(160/5/50)	32.10	0.58	530	14.2	2.79	0.005	1.90
	34.67	0.63	128	13.2	2.59	0.006	1.50
	51.68	0.23	391	39.1	1.77	0.001	

Both samples have an additional peak at around 51.7° alongside ZnO pattern. In order to investigate that peak, the phases that may occur during the process were taken into account.

Zinc hydroxide ($Zn(OH)_2$) has an orthorhombic structure and at 51.55 º it has (123) plane. Zinc hydroxide fluoride (Zn(OH)F) has an orthorhombic symmetry, and it has a (411) plane at 50.05 º and (212) plane at 51.8º. Also, zinc fluoride (ZnF_2) has a rutile tetragonal structure, and it has a (211) plane at 52º shown in Figure 3.2. The peak at around 51.7° could be mixture of ($Zn(OH)_2$) (123) plane and (Zn(OH)F) (212) plane. In both sample, the grain size is similar to each other for peak at around 51.7°.

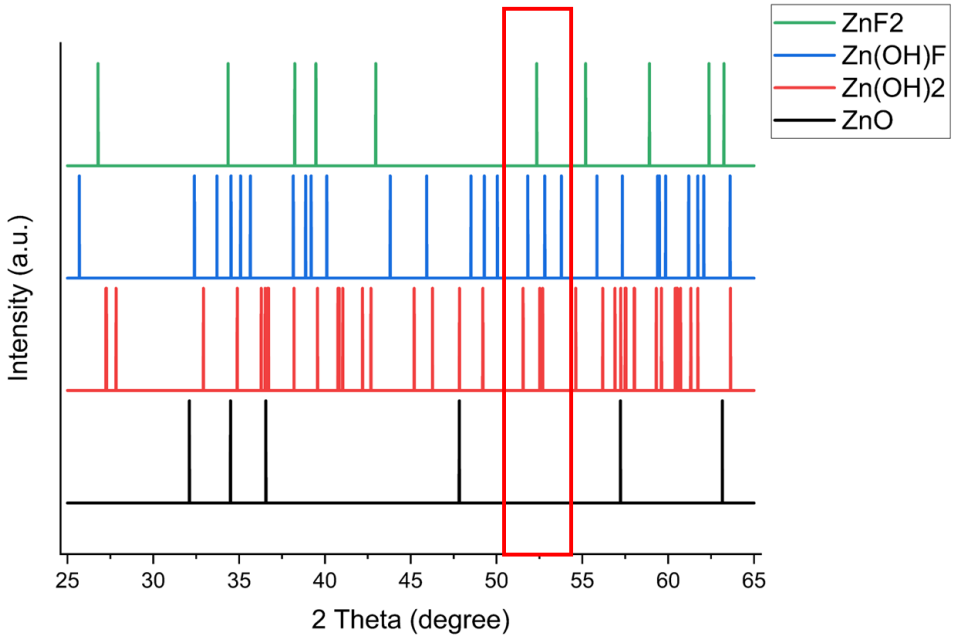

Figure 3.2. The XRD patterns of ZnO, ZnF2 and Zn(OH)F

In, Kang et al. study the pulse time for DEZ, H_2O and HF/DI water was chosen as 100 ms and purge time as 10s to maintain surface saturation as in this work. ZnO film that deposited at 160 ºC revealed (002) preferential growth orientation. On the other hand, with fluorine doping the preferential growth orientation change from (002) to (100) (K. M. Kang & Park, 2018). The reason behind that is filling oxygen vacancies by fluorine atoms or substitution of oxygen sites with fluorine ions.

As seen in Figure 3.1, for FZO(160/5/RT) (002) plane is preferential growth orientation while for FZO(160/5/50) (001) plane become preferential growth orientation. The fluorine incorporation could lead to that change because of ionic radius of fluorine is smaller than oxygen. Also, fluorine doping caused a decrease in grain size in (002) direction. Heating of canister room temperature to 50 °C caused decreasing grain size in (002) direction from 16.9 nm to 13.2 nm and internal stress is increased. Fluorine was incorporated more in heated canister.

In order to identify the concentration of fluorine incorporation XPS measurement were done. However, in both cases there were no peaks identified at F1s region shown in Figure 3.3

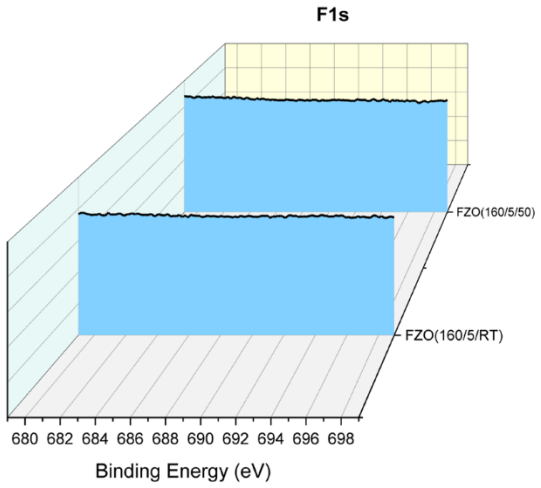

Figure 3.3. The F1s spectra of FZO(160/5/RT) and for FZO(160/5/50)

In Figure 3.4 the fluorine counts normalized to surface is shown. Fluorine atom dispersion in films could be observed. The heated cannister had more fluorine in film interface when compared to other. The XRD results and SIMS results were compatible. The vapor pressure of precursor is an important parameter as explained before. The high vapor pressure provides ease delivery of gas onto the substrate surface. Thus, the heating of the cannister caused a rise in vapor pressure of NH_4F/DI mixture and fluorine incorporation to the films. Also, the reactivity of the precursor is another essential property to provide fast surface reactions whereby film

uniformity. Increasing temperature of canister ensured more volatile and reactive precursor. As a result, more fluorine incorporated with increasing canister temperature.

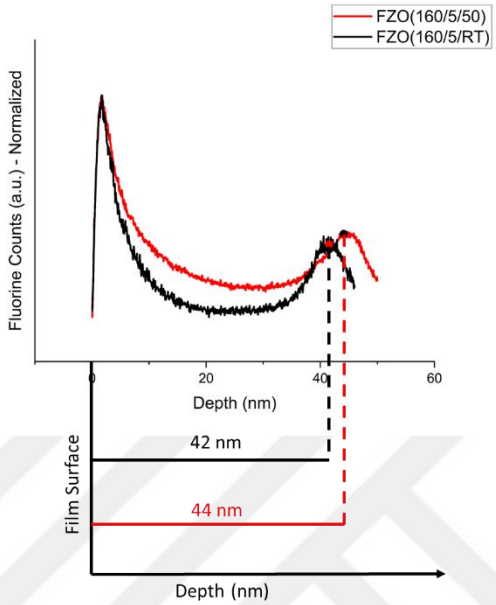

Figure 3.4. The fluorine counts that normalized on the film surface of FZO(160/5/RT) and for FZO(160/5/50)

3.1.2 Effect of Canister Temperature on Structural and Compositional Properties at 180 °C with 30% NH_4F/DI mixture

Another experiment was designed to observe canister temperature on fluorine incorporation at 180 ºC in 30% NH_4F/DI mixture with three different temperatures as room temperature (FZO(180/30/RT)), 40 ºC (FZO(180/30/40)) and 50 ºC (FZO(180/30/50)). The XRD pattern of these samples shown in Figure 3.5 and parameters are shown in Table 3.3.

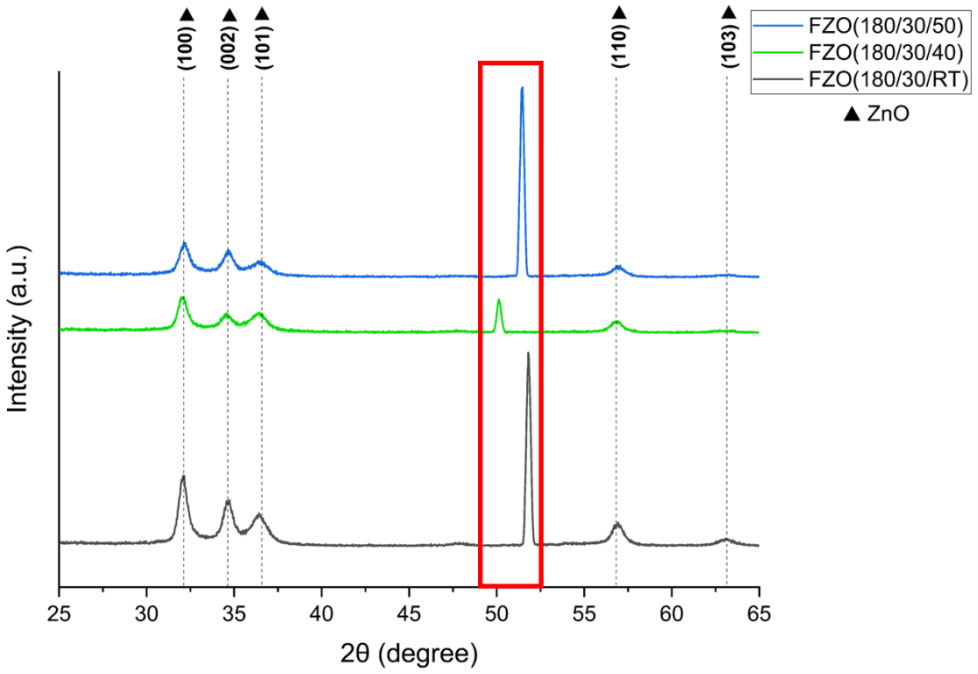

Figure 3.5. The XRD pattern of FZO(180/30/RT) , FZO(180/30/40) and FZO(180/30/50)

Table 3.3. The 2 Theta positions, planes, crystal size (D), d spacing, dislocation density and internal stress of FZO(180/30/RT) , FZO(180/30/40) and FZO(180/30/50)

Sample ID	2 THETA (°)	FWHM	Peak Intesity	D (nm)	d-spac	disloc den	internal stress (GPa)
FZO(180/30/RT)	32.06	0.57	556	14.4	2.79	0.005	1.61
	34.60	0.62	314	13.4	2.59	0.006	1.03
	51.79	0.23	1998	39.2	1.76	0.001	
FZO(180/30/40)	32.01	0.62	277	13.3	2.79	0.006	1.32
	34.52	0.70	106	11.9	2.60	0.007	0.52
	50.11	0.24	317	36.4	1.82	0.001	
FZO(180/30/50)	32.13	0.66	255	12.6	2.78	0.006	2.15
	34.62	0.66	154	12.6	2.59	0.006	1.17
	51.45	0.19	1824	46.4	1.77	0.000	

In Figure 3.5, all samples the peak at around 51° is dominated. The electronegativity of fluorine is very high and with high NH4F/DI mixture concentrations led to

formation of ZnOHF compound that has stability at around 390 °C (Srivastava & Secco, 1967). The ZnOHF has hydrogen bonding that provides thermal stability. Even though the canister held at room temperature FZO(180/30/RT), (212) plane of ZnOHF compound was dominated. Heated cannister at 40 °C FZO(180/30/40) (411) plane of ZnOHF compound became dominated. In FZO(180/30/50), the dominant peak appears at 51.4° and it can be (123) plane of Zn(OH)2.

For FZO(180/30/RT) sample the grain size was 39.2 nm in (212) plane of ZnOHF and similar with FZO(160/5/RT) and FZO(160/5/50). For FZO(180/30/40), ZnOHF changed its direction (212) to (411) and its grain size was smaller than (212) as 36.4 nm. However, in FZO(180/30/50) sample, (123) plane of Zn(OH)2 is dominated instead of ZnOHF and its grain size was larger than ZnOHF as 46.4 nm.

The grain size in (002) decreased from FZO(180/30/RT) to FZO(180/30/40) as 13.4 nm to 11.9 nm. Fluorine atoms could prefer forming of ZnOHF in FZO(180/30/40) instead of passivation of oxygen defects and results in decreased grain size. Then, the grain size increased from FZO(180/30/40) to FZO(180/30/50) as 11.9 nm to 12.6 nm. In FZO(180/30/50) fluorine atoms could prefer passivating oxygen defects and resulted in increased grain size and crystallinity.

The compositional analysis of these films was done by XPS and F1s regions are shown in Figure 3.6. As canister temperature increased fluorine concentration increased as expected.

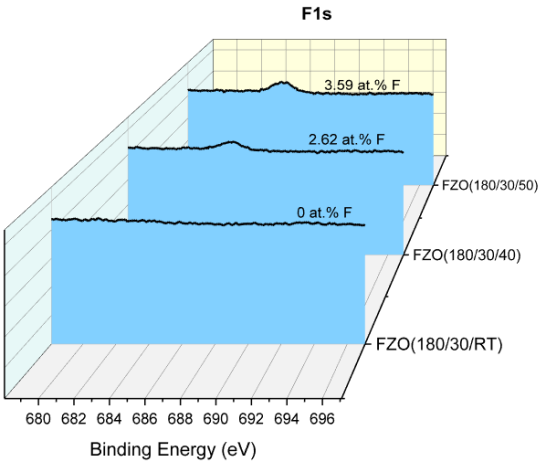

Figure 3.6. F1s regions of of FZO(180/30/RT) , FZO(180/30/40) and FZO(180/30/50)

The fluorine distribution in the films was observed by SIMS. Fluorine counts normalized to the film surface were compared for three samples as temperature rises fluorine distribution in the interface of films increases shown in Figure 3.7.

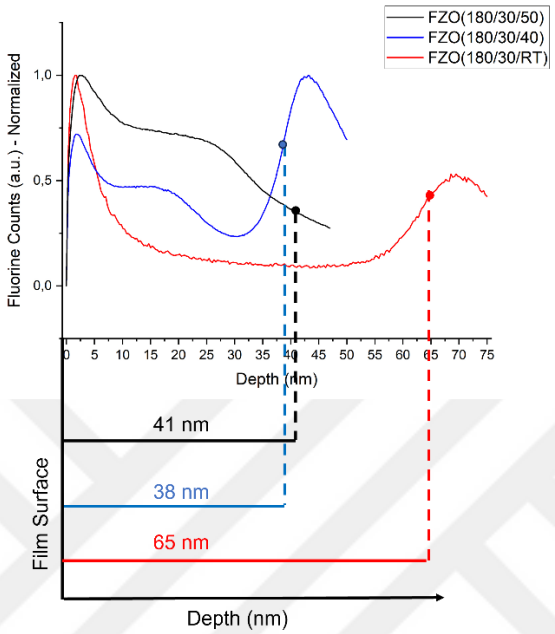

Figure 3.7. The fluorine counts normalized to films surface along the FZO(180/30/RT) , FZO(180/30/40) and FZO(180/30/50) films

The better understanding, the compositional analysis investigated. The Table 3.4 shows the Zn, O, F atomic percentages, Zn/O ratio and and Zn/F ratio. All samples were zinc rich. F/Zn ratio increased with increasing canister temperature as expected.

Table 3.4. The Zn, O, F atomic percentages Zn/O ratio and Zn/F ratio of FZO(180/30/RT) , FZO(180/30/40) and FZO(180/30/50) films.

Sample I.D.	Zn (at.%)	O (at.%)	F (at.%)	Zn/O	F/Zn
FZO(180/30/RT)	51.107	48.893	-	1.045	-
FZO(180/30/40)	49.433	47.944	2.62	1.031	0.053
FZO(180/30/50)	49.416	46.996	3.59	1.051	0.073

The O1s and Zn2$p_{3/2}$ regions were examined with CASA XPS programme. The programme interface is shown in Figure 3.8.

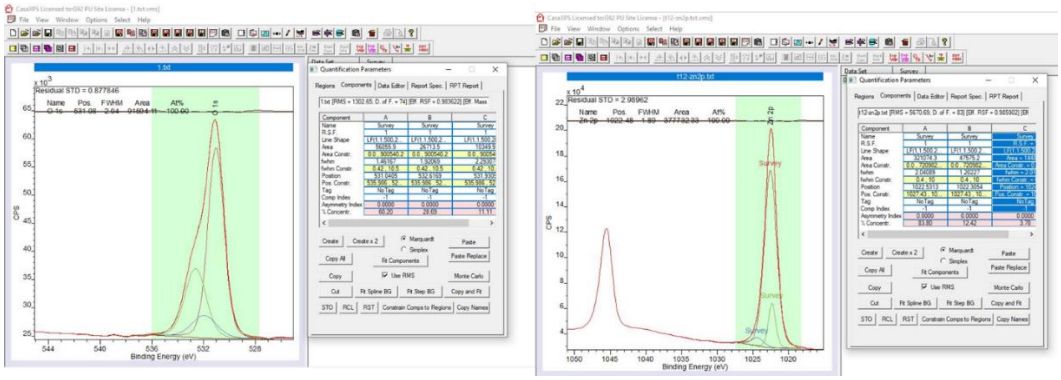

Figure 3.8. The interior of CASA XPS programme

O1s peak consists of 3 peaks OI, OII, and OIII. The percentage of OI area indicates metal oxide (ZnO) bonding, OII area indicates oxygen vacancies (Vo), and OIII area indicates hydroxide (-OH). Zn2p3/2 peak is composed of Zn^{+2}, ZnOH, and Zn^{0} (zinc intersitital) areas. The percentage of M-O/O total (M-O%), Voc/O total (Voc%), -OH/O total (-OH%), Zn^{0}/Zn total (Zn%), Zn^{+2}/Zn total (Zn+2%) and ZnOH/Zn total (ZnOH%) is tabulated in Table 3.5.

Table 3.5. The M-O%, Voc%, OH%, Zn%, Zn^{+2}% and ZnOH% with fluorine concentration for FZO(180/30/RT) , FZO(180/30/40) and FZO(180/30/50) films.

Sample I.D.	F (at.%)	M-O %	Voc %	OH %	Zn %	Zn+2 %	ZnOH %
FZO(180/30/RT)	-	69.11	29.65	1.24	12.91	83.22	3.86
FZO(180/30/40)	2.62	66.11	29.53	4.36	10.10	82.74	7.16
FZO(180/30/50)	3.59	72.61	22.53	4.86	9.99	81.36	8.65

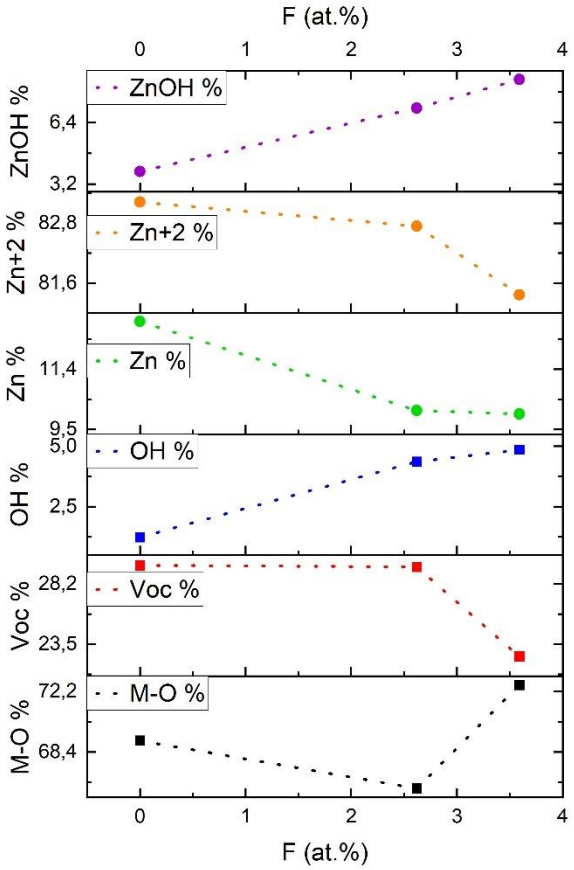

Figure 3.9. The change in M-O%, Voc%, OH%, Zn%, Zn^{+2}% and ZnOH% with fluorine concentration

Voc% did not change much from FZO(180/30/RT) (0 at.% F) to FZO(180/30/40) (2.62 at.% F). M-O% , Zn% , Zn+2% decreased while OH% and ZnOH% increased from 0 to 2.62 at.% F. In FZO(180/30/40), zinc atoms could bonded with OH instead of only O and fluorine ions attached to $Zn(OH)_2$ to form ZnOHF instead of filling oxygen vacancies. This can be the reason behind change in direction (212) plane to (411) of ZnOHF for FZO(180/30/40) (Figure 3.5). From FZO(180/30/40) (2.62 at.% F) to FZO(180/30/50) (3.59 at.% F) M-O% , OH% and $Zn(OH)_2$ increased while Voc%, Zn% , Zn+2% decreased. In FZO(180/30/50) zinc atom preferred both bonded with oxygen and OH group but fluorine ion preferred to fill oxygen vacancies and bond with zinc interstitials. In XRD pattern of FZO(180/30/50) $Zn(OH)_2$ peak ((123)) was observed instead of ZnOHF ((212) or (411)) and the reason behind that was fluorine occupy oxygen vacancies and bonding with zinc interstitials.

As a result, heating of canisters provided more fluorine doping to the ZnO films. The vapor pressure of precursor increased with temperature and the gas mixture could be transported onto surface easily (Dezelah, 2015). Also, reactivity of gas increased with temperature and more gas species could interact with the surface. This led to obtaining more fluorine doping. After these experiments, all canisters were heated to 50 °C.

3.2 Effect of NH_4F/DI Concentrations on Fluorine Doping Concentration

The ALD window for ZnO is described as between 100-200 °C in several studies (Guziewicz et al., 2020; Pilz et al., 2020; J. Zhang et al., 2013). As mentioned in previous section, through 200 °C the ZnO films were produced as zinc rich and has (002) preferential growth orientation. But, with fluorine doping preferential growth orientation changes to (100) shown by Kang et al. study (K.-M. Kang et al., 2016). Also, in another study, at 140 °C from 300 cycles to 1200 cycles as grown ZnO films had (002) growth orientation while fluorine doped ZnO films have (100) orientation.

In this study, the number of cycles were selected as 300, the deposition temperatures varied as 160,180 and 200 °C. In all temperatures, concentration of NH_4F/DI mixture varied from 1% to 40%. The designed experiments are shown in Table 3.6.

Table 3.6. The designed experiments and their details

Sample I.D.	Temperature (°C)	NH_4F concentration (%)	Precursor Temp. (°C)	Cycle ZnO:ZnO/F	Cycle
FZO(160/1/50)	160	1	50	0:1	300
FZO(160/5/50)		5			
FZO(160/10/50)		10			
FZO(160/20/50)		20			
FZO(160/30/50)		30			
FZO(160/40/50)		40			
FZO(180/1/50)	180	1			
FZO(180/5/50)		5			

Table 3.6 (continued)

FZO(180/20/50)		20			
FZO(180/30/50)		30			
FZO(180/40/50)		40			
FZO(200/20/50)	200	20			
FZO(200/30/50)		30			
FZO(200/40/50)		40			

3.2.1 Effect of NH_4F/DI Concentrations on Structural and Compositional Properties at 160 °C with 50 °C Heated Canister

Firstly, samples that have a deposition temperature as 160 °C was examined for structural and compositional properties. In Figure 3.10 the XRD patterns of FZO(160/1/50), FZO(160/5/50), FZO(160/10/50), FZO(160/20/50), FZO(160/30/50) and FZO(160/40/50). The XRD parameters are tabulated in Table 3.7.

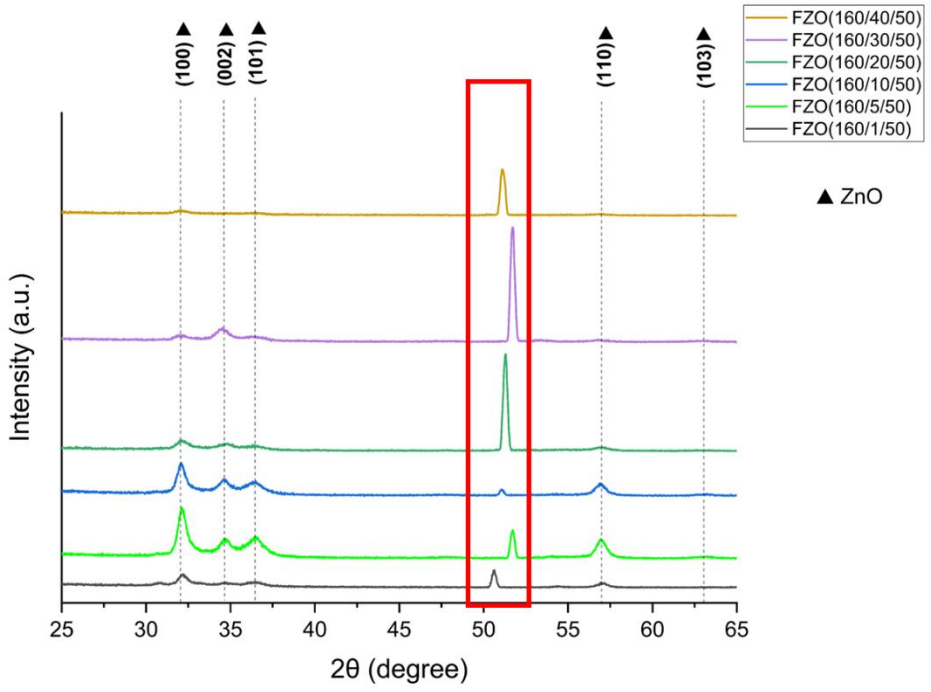

Figure 3.10. The XRD pattern of FZO(160/1/50), FZO(160/5/50), FZO(160/10/50), FZO(160/20/50), FZO(160/30/50) and FZO(160/40/50).

Table 3.7. The 2 Theta positions, planes, grain size (D), d spacing, dislocation density and internal stress of FZO(160/1/50), FZO(160/5/50), FZO(160/10/50), FZO(160/20/50), FZO(160/30/50) and FZO(160/40/50).

Sample I.D.	2 THETA (°)	FWHM	Peak Intesity	D (nm)	d-spac.	disloc. den.	internal stress (GPa)
FZO(160/1/50)	32.11	0.60	113	13.78	2.79	0.005	2.00
	34.54	0.90	20	9.24	2.59	0.012	0.65
	50.58	0.24	216	36.61	1.80	0.001	
FZO(160/5/50)	32.10	0.58	530	14.23	2.79	0.005	1.90
	34.67	0.63	128	13.21	2.59	0.006	1.50
	51.68	0.23	391	39.06	1.77	0.001	
FZO(160/10/50)	32.05	0.57	323	14.60	2.79	0.005	1.56
	34.56	0.62	110	13.42	2.59	0.006	0.78
	51.05	0.21	77	41.72	1.79	0.001	
FZO(160/20/50)	32.09	0.82	91	10.08	2.79	0.010	1.86
	34.74	1.15	60	7.24	2.58	0.019	1.95
	51.25	0.23	1354	38.46	1.78	0.001	
FZO(160/30/50)	31.92	1.05	49	7.87	2.80	0.016	0.66
	34.46	0.91	126	9.14	2.60	0.012	0.13
	51.61	0.21	1707	42.63	1.77	0.001	
FZO(160/40/50)	31.98	0.85	32	9.72	2.80	0.011	1.08
	50.97	0.19	240	46.32	1.79	0.000	
	51.14	0.21	551	41.94	1.78	0.001	

At 160 °C, up to 10% NH_4F/DI mixture ZnO peaks were prominent in XRD patterns. The mixture of (100) and (002) grains of ZnO were dominant for 1-10% NH_4F/DI mixture. In between 20-40% NH_4F/DI mixture XRD pattern of ZnO could not appear.

FZO(160/1/50) to FZO(160/5/50) both grains in (100) and (002) got enlarged and crystallinity was enhanced with fluorine incorporation. FZO(160/5/50) to FZO(160/10/50) grains in (100) and (002) continued to enlarge slightly with enhancing crystallinity. For FZO(160/20/50), FZO(160/30/50) and FZO(160/40/50)

both (100) and (002) was diminished because of the excessive fluorine doping. FZO(160/1/50) contained mixture of (411)/(212) ZnOHF grains at 50.58°. FZO(160/5/50) contained the mixture (212) plane of ZnOHF and (123) plane of ZnOH2 at 51.68°. FZO(160/10/50) contained the mixture (411) plane of ZnOHF and (123) plane of $Zn(OH)_2$ at 51.05°. FZO(160/20/50) contained (123) plane of $ZnOH_2$ at 51.25°. FZO(160/30/50) contained the mixture (212) plane of ZnOHF and (123) plane of $Zn(OH)_2$ at 51.61°. FZO(160/40/50) contained both mixture of (203) and (123) plane of $Zn(OH)_2$ at 50.97° and 51.14°.As fluorine concentration increased, (100) and (002) planes were diminished and ZnOHF and $Zn(OH)_2$ planes were getting dominant.

The XPS analysis were conducted for 10% NH_4F/DI mixture and above shown in Figure 3.11. Even though 10% NH4F/DI mixture was seen as high, fluorine concentration could not be detected by XPS. FZO (160/20/50) had more fluorine concentration than FZO(160/30/50). But HR-XPS were conducted on the surface of the films. The depth profile for fluorine concentration could not be observed because fluorine was very sensitive to radiation.

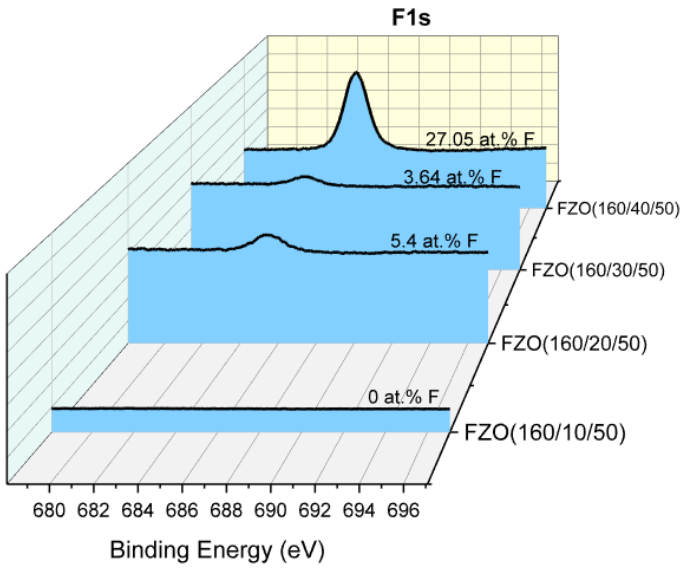

Figure 3.11. F1s regions of FZO(160/10/50), FZO(160/20/50), FZO(160/30/50) and FZO(160/40/50).

The fluorine counts normalized on film surface are compared for FZO(160/5/50) and FZO(160/10/50) is Figure 3.12. As expected, FZO(160/10/50) had more fluorine than FZO(160/5/50) in film interface.

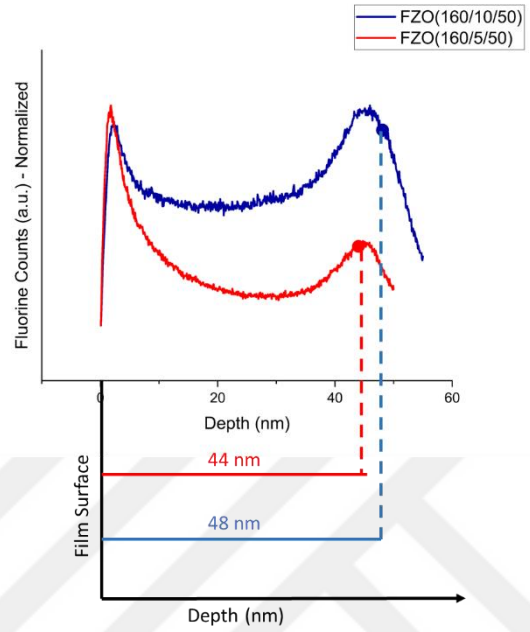

Figure 3.12 The fluorine counts normalized to films surface along the FZO(160/5/50) and FZO(160/10/50)

In Table 3.8, the atomic percentages of Zn, O and, ratio of Zn/O and Zn/F for FZO(160/20/50), FZO(160/30/50) and FZO(160/40/50) films are tabulated. 40% NH_4F/DI mixture caused excessive fluorine concentration. FZO(160/20/50) had more fluorine concentration than FZO(160/30/50) at surface. The reason behind that could be on the surface of FZO(160/20/50) sample fluorine bonded with carbon (C-F %) more than FZO(160/30/50).

Table 3.8. The Zn, O, F atomic percentages Zn/O ratio and Zn/F ratio of FZO(160/20/50), FZO(160/30/50) and FZO(160/40/50) films.

Sample I.D.	Zn (at.%)	O (at.%)	F (at.%)	Zn/O	F/Zn
FZO(160/20/50)	49.06	45.54	5.41	1.08	0.11
FZO(160/30/50)	48.35	48.02	3.64	1.01	0.08
FZO(160/40/50)	38.74	34.21	27.05	1.13	0.70

The O1s and $Zn2p_{3/2}$ regions for 20% NH_4F/DI, 30% NH_4F/DI and 40% NH_4F/DI were examined with CASA XPS program. The percentages of the O regions and Zn regions as a function of the surface fluorine concentration are given in Table 3.9 and Figure 3.13.

Table 3.9. The M-O%, Voc%, OH%, Zn%, Zn^{+2}% and ZnOH% with fluorine concentration for FZO(160/20/50), FZO(160/30/50) and FZO(160/40/50) films.

Sample I.D.	F (at.%)	M-O %	Voc %	OH %	Zn %	Zn+2 %	ZnOH %
FZO(160/20/50)	5.41	66.40	26.47	7.12	9.82	86.94	3.24
FZO(160/30/50)	3.64	60.83	32.96	6.21	12.88	83.00	4.12
FZO(160/40/50)	27.05	9.75	3.59	86.66	2.65	89.95	7.40

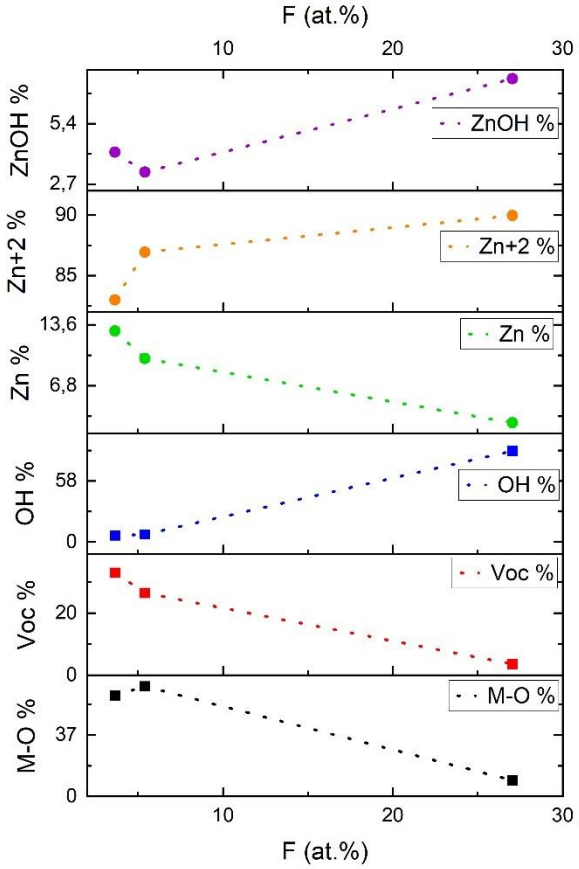

Figure 3.13. The change in M-O%, Voc%, OH%, Zn%, Zn^{+2}% and ZnOH% with fluorine concentration for FZO(160/20/50), FZO(160/30/50) and FZO(160/40/50).

FZO(160/30/50) (3.64 at.% F) to FZO(160/20/50) (5.41 at.% F) M-O% and Zn^{+2}% increased while Voc%, Zn%, and ZnOH% decreased and OH% did not change much. In FZO(160/20/50) (5.41 at.% F) fluorine ions preferred filling oxygen vacancies and bonding with fluorine interstitials while zinc atom preferred bonding with oxygen. FZO(160/20/50) (5.41 at.% F) to FZO(160/40/50) (27.05 at.% F) M-O% , Voc%, Zn% decreased drastically while OH%, Zn^{+2}% and ZnOH% increased. In FZO(160/40/50) (27.05 at.% F) fluorine anions preferred filling oxygen vacancies, bonding with zinc interstitials while zinc atoms preferred bonding with OH to produce ZnOH compound.

3.2.2 Effect of NH_4F/DI Concentrations on Structural and Compositional Properties at 180 °C with 50 °C Heated Canister

The samples that have a growth temperature as 180 °C were examined for structural and compositional properties. In Figure 3.14 the XRD patterns of FZO(180/1/50), FZO(180/5/50), FZO(180/20/50), FZO(180/30/50) and FZO(180/40/50). The XRD parameters are tabulated in Table 3.10.

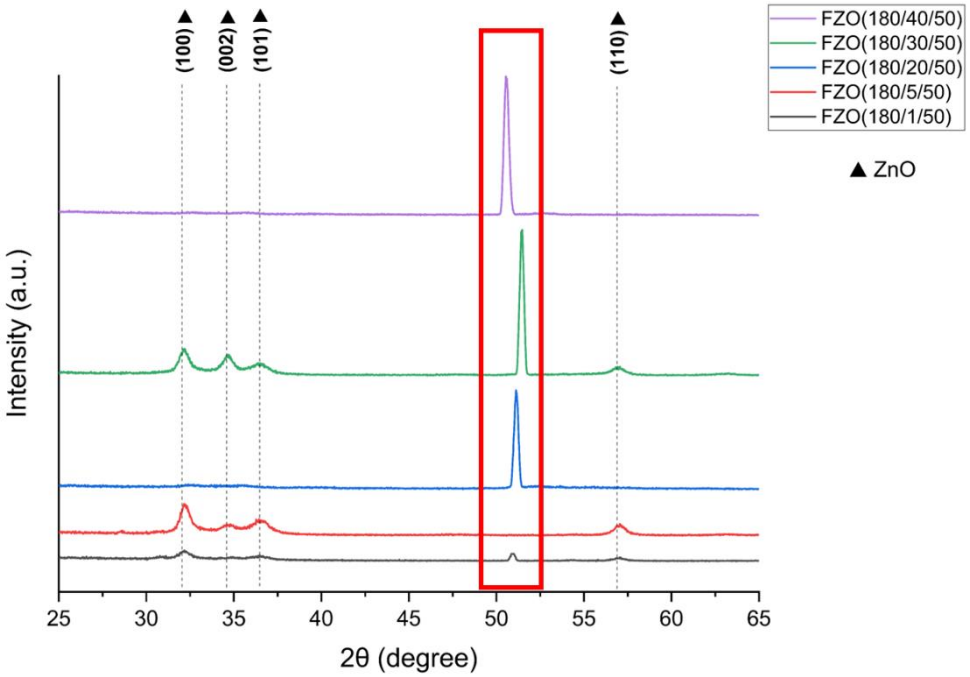

Figure 3.14. The XRD pattern of FZO(180/1/50), FZO(180/5/50), FZO(180/20/50), FZO(180/30/50) and FZO(180/40/50).

Table 3.10. The 2 Theta positions, planes, grain size (D), d spacing, dislocation density and internal stress of FZO(180/1/50), FZO(180/5/50), FZO(180/20/50), FZO(180/30/50) and FZO(180/40/50).

Sample I.D.	2 THETA (°)	FWHM	Peak Intesity	D (nm)	d-spac.	disloc. den.	internal stress (GPa)
FZO(180/1/50)	32.12	0.77	92	10.74	2.78	0.009	1.56
	34.83	0.60	12	13.88	2.57	0.005	2.53
	50.89	0.23	101	37.60	1.79	0.001	
FZO(180/5/50)	32.17	0.65	323	12.70	2.78	0.006	2.44
	34.60	1.45	95	5.74	2.59	0.030	1.04
FZO(180/20/50)	32.47	1.10	19	7.52	2.76	0.018	4.49
	51.11	0.23	1323	38.62	1.79	0.001	
FZO(180/30/50)	32.13	0.66	255	12.56	2.78	0.006	2.15
	34.62	0.66	154	12.61	2.59	0.006	1.17
	51.45	0.19	1824	46.41	1.77	0.000	
FZO(180/40/50)	32.67	1.30	9	6.37	2.74	0.025	5.85
	50.51	0.28	1757	31.14	1.81	0.001	

The (002) plane of ZnO was getting diminished by increasing concentration of NH_4F/DI mixture. FZO(180/20/50) had mixture of (203) and (123) planes of $Zn(OH)_2$. FZO(180/30/50) had a (123) plane of $Zn(OH)_2$. But, in FZO(180/40/50) only ZnOHF planes of (411) and (212) were observed.

In Figure 3.15 the F1s regions of FZO(180/20/50), FZO(180/30/50) and FZO(180/40/50) is given. FZO(180/20/50) had more fluorine concentration than FZO(180/30/50). The case was similar with FZO(160/20/50) and FZO(160/30/50). As explained earlier, the HR-XPS were conducted on surface. We could not identify the depth profile of fluorine.

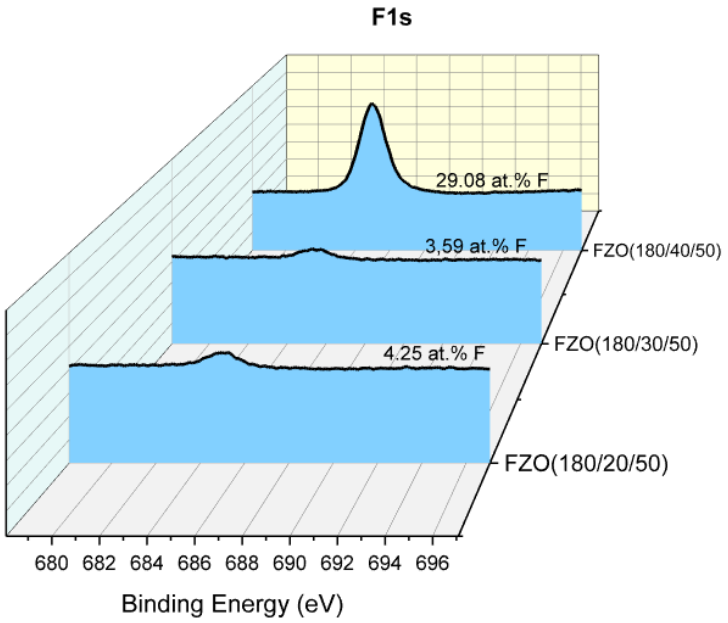

Figure 3.15. F1s regions of FZO(180/20/50), FZO(180/30/50) and FZO(180/40/50).

In Table 3.11, the atomic percentages of Zn, O and, ratio of Zn/O and Zn/F for FZO(180/20/50), FZO(180/30/50) and FZO(180/40/50) films are tabulated. 40% NH_4F/DI mixture caused excessive fluorine concentration. FZO(180/20/50) had more fluorine concentration than FZO(180/30/50) at surface. The reason behind that could be on the surface of FZO(180/20/50) sample fluorine bonded with carbon (C-F %) more than FZO(180/30/50). The case was similar to FZO(160/20/50) and FZO(160/30/50).

Table 3.11. The Zn, O, F atomic percentages Zn/O ratio and Zn/F ratio of FZO(180/20/50), FZO(180/30/50) and FZO(180/40/50) films.

Sample I.D.	Zn (at.%)	O (at.%)	F (at.%)	Zn/O	F/Zn
FZO(180/20/50)	49.06	46.68	4.25	1.0509	0.09
FZO(180/30/50)	49.42	47.00	3.59	1.0515	0.07
FZO(180/40/50)	39.47	31.43	29.08	1.256	0.74

In Figure 3.16 the fluorine counts normalized to films surface is compared for FZO(180/20/50), FZO(180/30/50) and FZO(180/40/50). Even though

FZO(180/20/50) had more fluorine concentration on the surface, in interface FZO(180/30/50) had more fluorine distribution in film interface than FZO(180/20/50).

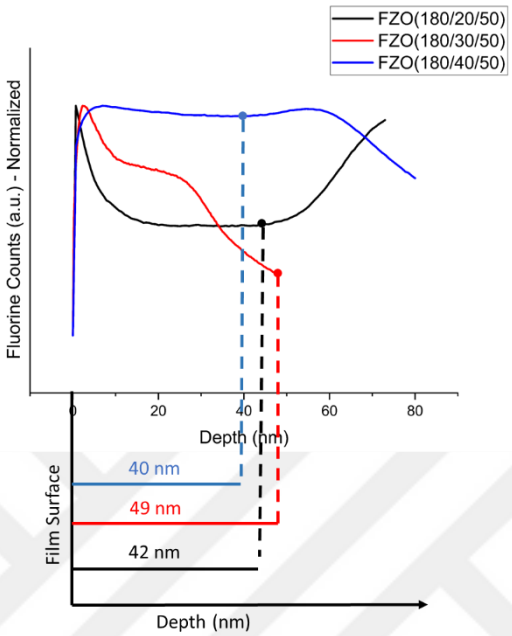

Figure 3.16. The fluorine counts normalized to films surface along the FZO(180/20/50), FZO(180/30/50) and FZO(180/40/50).

The O1s and $Zn2p_{3/2}$ regions for FZO(180/20/50), FZO(180/30/50) and FZO(180/40/50) were examined and shown in Figure 3.17. The percentages of the O regions and Zn regions as a function of the surface fluorine concentration are given in Table 3.12.

Table 3.12. The M-O%, Voc%, OH%, Zn%, Zn^{+2}% and ZnOH% with fluorine concentration for FZO(180/20/50), FZO(180/30/50) and FZO(180/40/50) films.

Sample I.D.	F (at.%)	M-O %	Voc %	OH %	Zn %	Zn+2 %	ZnOH %
FZO(180/20/50)	4.25	65.17	23.57	11.26	1.73	73.82	24.44
FZO(180/30/50)	3.59	72.61	22.53	4.86	9.99	81.36	8.65
FZO(180/40/50)	29.08	7.68	8.56	83.76	12.35	82.91	4.74

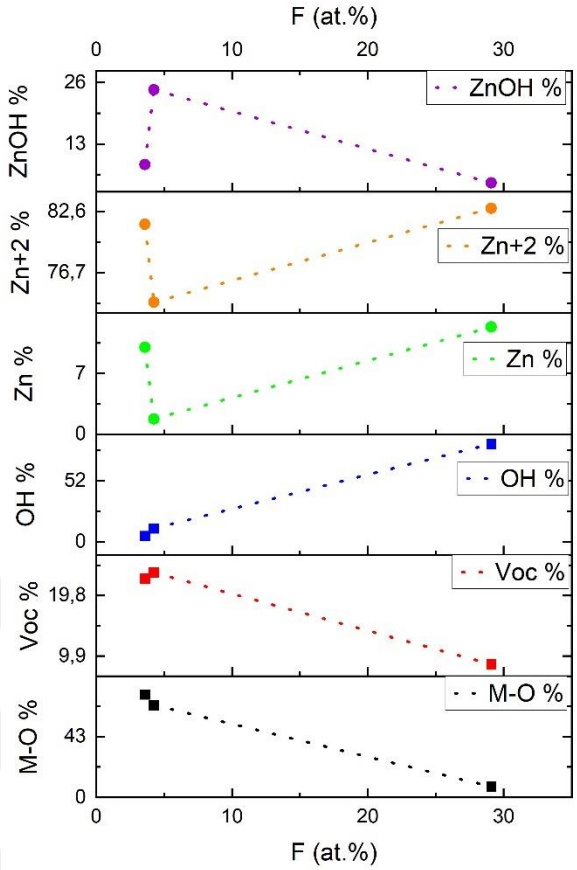

Figure 3.17. The change in M-O%, Voc%, OH%, Zn%, Zn^{+2}% and ZnOH% with fluorine concentration for FZO(180/20/50), FZO(180/30/50) and FZO(180/40/50).

FZO(180/30/50) (3.59 at.%) to FZO(180/20/50) (4.25 at.%) M-O%, Zn%, Zn^{+2}% decreased while Voc% and ZnOH% increased. In FZO(180/20/50) fluorine ions preferred bonded with zinc interstitials and zinc ions instead of occupy oxygen vacancies. FZO(180/20/50) (4.25 at.%) to FZO(180/40/50) (29.08 at.%) M-O%, Voc% and ZnOH% decreased while OH%, Zn%, Zn+2% decreased. In FZO(180/40/50) fluorine anions preferred occupy oxygen vacancies, bonding with zinc interstitials and zinc ions.

3.2.3 Effect of NH_4F/DI Concentrations on Structural and Compositional Properties at 200 °C with 50 °C Heated Canister

In Figure 3.18 the XRD patterns of FZO(200/20/50), FZO(200/30/50) and FZO(200/40/50). The XRD parameters are tabulated in Table 3.13.

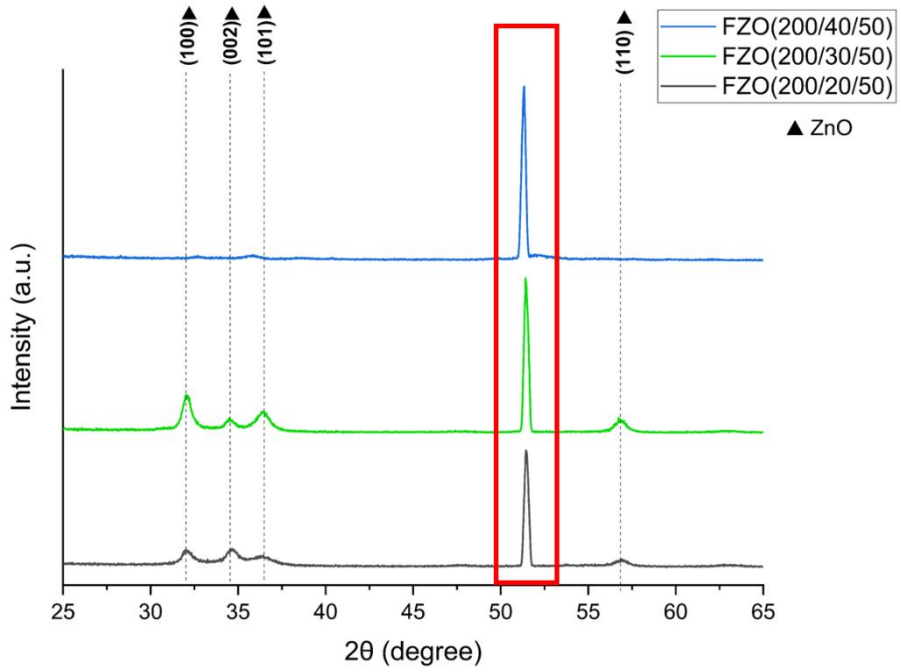

Figure 3.18. The XRD pattern of FZO(200/20/50), FZO(200/30/50) and FZO(200/40/50).

Table 3.13. The 2 Theta positions, planes, grain size (D), d spacing, dislocation density and internal stress of FZO(200/20/50), FZO(200/30/50) and FZO(200/40/50).

Sample I.D.	2 THETA (°)	FWHM	Peak Intesity	D (nm)	d-spac.	disloc. den.	internal stress (GPa)
FZO(200/20/50)	31.99	0.70	135	11.81	2.80	0.007	1.15
	34.59	0.77	135	10.81	2.59	0.009	0.98
	51.44	0.22	1454	40.38	1.77	0.001	
FZO(200/30/50)	32.05	0.57	341	14.42	2.79	0.005	1.56
	34.42	0.63	87	13.20	2.60	0.006	0.13
	51.43	0.22	1893	39.95	1.78	0.001	
FZO(200/40/50)	32.52	0.89	12	9.30	2.75	0.012	
	51.30	0.21	2075	41.34	1.78	0.001	

In all samples, the dominant peak belongs to (123) plane of Zn(OH)2. As fluorine concentration increases ZnO peaks disappear.

F1s peak regions of FZO(200/20/50), FZO(200/30/50) and FZO(200/40/50) is given Figure 3.19.

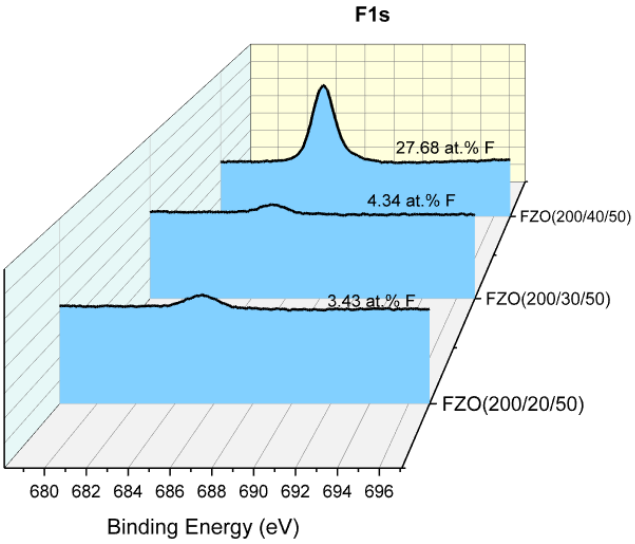

Figure 3.19. F1s peak areas of FZO(200/20/50), FZO(200/30/50) and FZO(200/40/50).

In Table 3.14, the atomic percentages of Zn, O and, ratio of Zn/O and Zn/F for FZO(200/20/50), FZO(200/30/50) and FZO(200/40/50) films are tabulated. 40% NH4F/DI mixture caused excessive fluorine concentration. FZO(200/30/50) had more fluorine concentration than FZO(200/20/50) at surface as expected.

Table 3.14. The Zn, O, F atomic percentages Zn/O ratio and Zn/F ratio of FZO(200/20/50), FZO(200/30/50) and FZO(200/40/50) films.

Sample I.D.	Zn (at.%)	O (at.%)	F (at.%)	Zn/O	F/Zn
FZO(200/20/50)	48.59	47.99	3.43	1.01	0.07
FZO(200/30/50)	48.72	46.96	4.34	1.04	0.09
FZO(200/40/50)	35.65	36.65	27.68	0.97	0.78

The O1s and Zn2$p_{3/2}$ regions for FZO(200/20/50), FZO(200/30/50) and FZO(200/40/50) were examined and shown in Figure 3.20. The percentages of the O regions and Zn regions as a function of the surface fluorine concentration are given in Table 3.15.

Table 3.15. The M-O%, Voc%, OH%, Zn%, Zn^{+2}% and ZnOH% with fluorine concentration for FZO(200/20/50), FZO(200/30/50) and FZO(200/40/50).

Sample I.D.	F (at.%)	M-O %	Voc %	OH %	Zn %	Zn+2 %	ZnOH %
FZO(200/20/50)	3.43	66.37	5.78	27.85	2.13	84.07	13.80
FZO(200/30/50)	4.34	66.54	28.30	5.16	10.14	85.65	4.21
FZO(200/40/50)	27.68	7.72	81.76	10.52	80.74	13.77	5.49

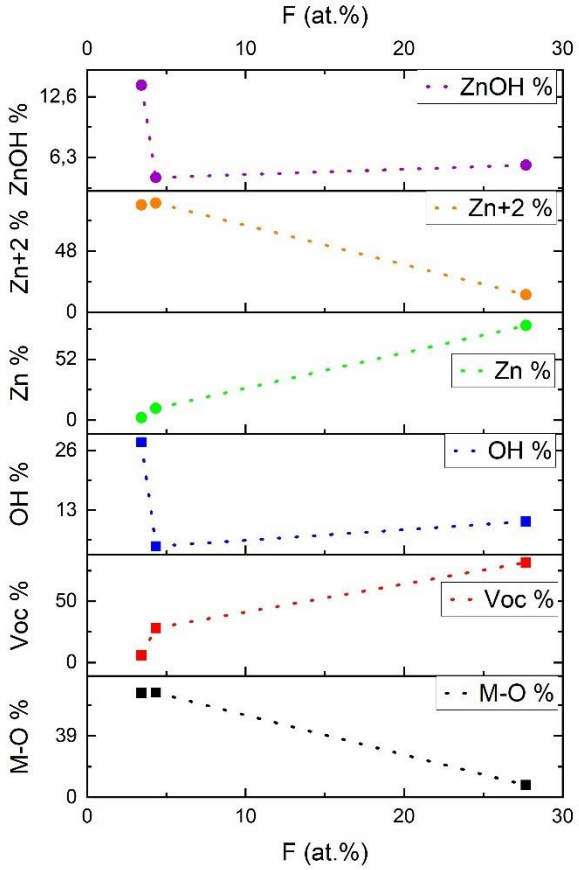

Figure 3.20. The change in M-O%, Voc%, OH%, Zn%, Zn^{+2}% and ZnOH% with fluorine concentration for FZO(200/20/50), FZO(200/30/50) and FZO(200/40/50).

FZO(200/20/50) to FZO(200/30/50) OH% and ZnOH% decreased while Voc%, Zn% and Zn^{+2}% slightly increased. In FZO(200/30/50) fluorine ions preferred bonding with zinc ions instead of filling oxygen vacancies. FZO(200/30/50) to FZO(200/40/50) M-O%, Zn^{+2}% decreased while Voc% and Zn% increased. OH%

and ZnOH% did not change much. In FZO(200/40/50) fluorine ions preferred bonding with zinc ions instead of filling oxygen vacancies.

3.3 The Effect of Fluorine Doping Concentration and Deposition Temperature on Electrical and Optical Properties of FZO Films

3.3.1 The Electrical Properties

The electrical properties of FZO films strongly depend on the crystal quality. The defects in crystals act as trap states for charge carriers and the grain boundaries are scattering centers. The density of charge carriers decreases with number of defects and the mobility of these charge carriers also decreases due to scattering centers (Gunasekaran et al., 2018; Noirfalise et al., 2011).

The fluorine concentration affects crystallinity. At low fluorine concentrations (1 at.%), fluorine ions passivate oxygen related defects and enhance the crystallinity of ZnO (Muhammad et al., 2021; Polydorou et al., 2016). Also, up to certain fluorine concentration, grain size of ZnO increases (Samanta et al., 2022). The larger grains indicate lower grain boundaries. The carrier concentration and mobility of FZO films are enhanced by fluorine at low concentrations and whereby the conductivity of films is improved (Pawar et al., 2008).

However, towards higher fluorine concentrations, the crystallinity of ZnO decreases. The substitution of fluorine ions with oxygen causes a decrease in the grain size of ZnO due to ionic radius difference of oxygen and fluorine. This difference indicates Zn-F has a smaller bond length than Zn-O and causes grain size and crystallinity to decrease. Because of fluorine's diminished effect on ZnO planes through higher fluorine content, the conductivity of FZO films decreases (Gunasekaran et al., 2018; Papari et al., 2017; Sanchez-Juarez et al., 1998).

At excessive fluorine concentrations, fluorine atoms present at interstitial sites in ZnO lattice cause a larger density of dislocations (Pawar et al., 2008; Sanchez-Juarez et al., 1998). Unwanted compounds as $Zn(OH)_2$, ZnOHF and ZnF_2 are obtained

(Muhammad et al., 2021; Papari et al., 2017; Polydorou et al., 2016). Although interaction with F^- more thermodynamically favored, at excessive NH_4F concentrations, both NH_3^+ and F^- ions can interact with zinc. In Dong et al. study, DFT calculations show that NH_4OH can be used for p type doping of ZnO (Dong et al., 2009). Thus, the excessive usage of NH_4F concentration causes excessive fluorine content, creation of scattering centers, formation of unwanted compounds, erosion of ZnO planes, and inhibiting n-type doping of ZnO by Zn-NH_3^+ interaction.

Since FZO films that are used as TCO are utilized in optoelectronic applications frequently, the optical and electrical properties of these films are very important. According to the literature, the best electrical properties of FZO films were achieved at up to 2 at.% F doping (Bhachu et al., 2012; Y. J. Choi, Kang, & Park, 2015; Y. J. Choi & Park, 2014; Pham et al., 2021; X. Zhang et al., 2014) due to enhanced crystallinity, the absence of formation of different compounds that has detrimental effects on electrical properties and having low density of scattering centers (fluorine interstitials, grain boundaries etc.).

In literature the resistivity and optical transmittance at 400-800 nm for CVD-grown FZO film with 3 at. % F doping was reported as 18.57 Ω.cm and 84% respectively (Anusha & Arivuoli, 2013). In this thesis, the lowest fluorine concentration was achieved as 2.62 at.% in FZO(180/30/40). Although the fluorine concentration is higher than the desired content, the electrical properties of FZO(180/30/40) were identified by Hall measurement. The resistivity, number of charge carriers and mobility values are 2.14 ohm.cm, 1.24×10^{18} 1/cm^3 and 2.36 cm^2/(V.s), respectively. Further investigation must be carried out at around 1-2 at.% F concentration. In order to obtain around 1-2 at.% F doping low NH_4F concentration must be used.

3.3.2 The Optical Properties

The transmittance of FZO films depends on Zn/[O+F] ratio. The more zinc content leads to higher light scattering and results in the reduction of transmittance (Gunasekaran et al., 2018; Noirfalise et al., 2011; Sanchez-Juarez et al., 1998). The transmittance percentages of FZO films are given in Figure 3.21. The average

transmittance values 400 nm to 700 nm of all FZO films were above 80% except FZO(180/30/40) that has 78% transmittance with high Zn/[O+F] ratio.

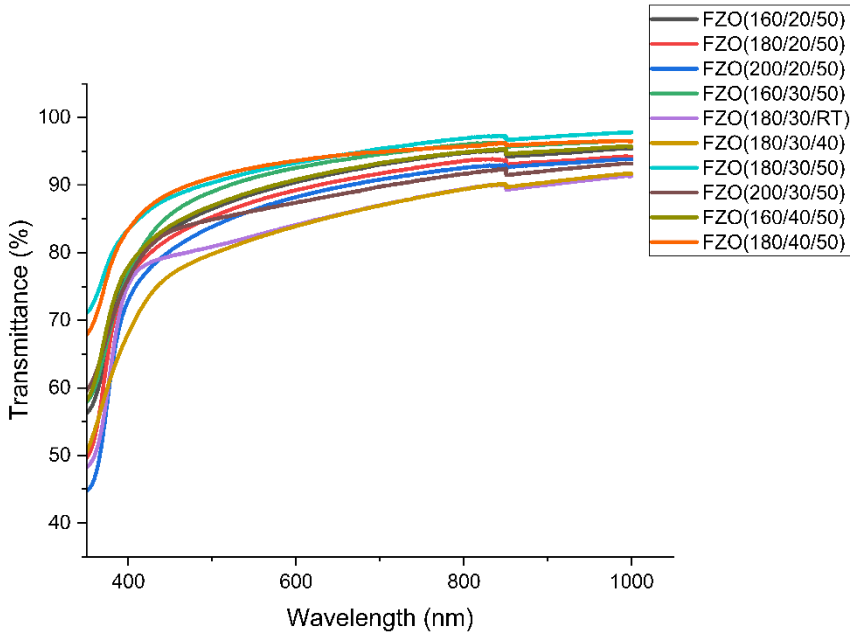

Figure 3.21. The transmittance percentages of all FZO samples.

3.4 The Effect of Fluorine Concentration on Growth per Cycle

The thickness of the films that grown on Si substrate were measured by DEKTAK and grown on quartz substrate were measured by ellipsometry. According to thickness results, GPC for each sample calculated and shown in **Table 3.16**. High fluorine concentrations led to unwanted compounds that affect the growth of rate of FZO films (Muhammad et al., 2021; Papari et al., 2017). GPC cycle decreased with increasing fluorine concentration at all temperatures.

Table 3.16. GPC for each sample on silicon and quartz substrate

Sample I.D.	F at.%	GPC on Silicon	GPC on Quartz
FZO(180/30/RT)	0	0.25	0.21
FZO(180/30/40)	2.62	0.15	0.20
FZO(180/30/50)	3.59	0.16	0.20
FZO(160/20/50)	5.41	0.18	0.15

Table 3.16 (continued)

FZO(160/30/50)	3.64	0.18	0.05
FZO(160/40/50)	27.05	0.13	0.18
FZO(180/20/50)	4.25	0.14	0.17
FZO(180/30/50)	3.59	0.16	0.20
FZO(180/40/50)	29.08	0.14	0.10
FZO(200/20/50)	3.43	0.15	0.12
FZO(200/30/50)	4.34	0.23	0.22
FZO(200/40/50)	27.68	0.16	-

3.5 Conclusion

In this thesis, the in-situ doped FZO films were produced by ALD. NH_4F/DI mixture was used for the first time as a fluorine doping source for ALD. The fluorine incorporation to ZnO films were optimized with different deposition temperatures (160-200 °C), NH_4F/DI mixture concentrations (1-40%) and canister temperatures (RT, 40 and 50 °C). The conclusions of this study are given as follows:

- Fluorine doping concentration increased with increasing canister temperature.
- The minimum fluorine concentration was achieved for deposition temperature at 180 °C with a 30% NH4F/DI mixture, 40 °C canister temperature as 2.62 at.% and the highest fluorine doping was achieved at 180 °C with a 40% NH_4F/DI mixture, 50 °C canister temperature as 29.08 at.%
- The usage of NH_4F concentration excessively caused excessive fluorine concentration, creation of scattering centers (grain boundaries, fluorine interstitials etc.), formation of unwanted compounds ($Zn(OH)_2$ and ZnOHF etc.), erosion of ZnO planes, and inhibiting n-type doping of ZnO by Zn-NH_3^+ interaction. All of them had destructive effects on the electrical properties of FZO films.

- Fluorine concentration was higher for 20% NH_4F/DI mixture than 30% NH_4F/DI mixture at 160 and 180 C. The reason here was explained as more fluorine ions bonded with carbon on the surface for 20% NH_4F/DI mixture and led to high detection of fluorine with XPS.
- Fluorine doping was higher with deposition temperature at 160 °C than 200 °C for 20% and 30% NH_4F/DI mixture. The reason behind that was founded as at 160 C fluorine preferred filling oxygen vacancies and bonding with zinc interstitials while at 200 C fluorine preferred only bonding with zinc metal.
- The growth per cycle (GPC) was also affected by fluorine doping concentration. Since the high fluorine concentration led to unwanted compounds, GPC decreased with increasing fluorine concentration at all temperatures.
- In this study, the best electrical properties were achieved at 2.62 at. % fluorine doping deposition temperature at 180 °C with a 30% NH_4F/DI mixture, 40 °C canister with 2.14 Ω.cm resistivity, 1.24 $x10^{18}$ $1/cm^3$ carrier concentration, and 2.36 Hall mobility cm^2/Vs. The average transmittance values 400 nm to 800 nm of all FZO films are approximately 80% and above. In literature, the CVD-grown FZO film with 3 at. % F doping has a resistivity of 18.57 Ω.cm and average transmission in 400-800 nm of 84% respectively. Thus, our new precursor, the NH_4F/DI mixture for ALD, at low fluorine concentrations was successful.
- In literature the best electrical properties of FZO achieved up to 2 at. % as approximately 10^{-4} Ω.cm resistivity and above 80% average transmission in 400-800 nm. In order to achieve that doping level, the concentration of NH_4F/DI mixture must be used up to 10%, the canister must be heated up to 50 °C. In this study, more fluorine doping was obtained with deposition temperature at 160 °C than 200 °C for 20% and 30% NH_4F/DI mixture. So, 10% NH_4F/DI mixture can be used for 200 °C and lower concentrations of NH_4F/DI mixture can be used for lower deposition temperatures.

CHAPTER 4

FUTURE WORKS

4.1 Future Works

As future works, further investigation must be done to optimize electrical and optical properties of ALD grown FZO films that produced by NH_4F/DI mixture for TCO application. According to literature the best electrical properties of FZO achieved up to 2 at.% and the optimization of FZO films must be done at that range.

Also, fluorine doped SnO_2 (FTO) will be produced via ALD by using NH_4F/DI mixture for the first time in the world. Firstly, SnO_2 deposition will be optimized by using different temperatures, pulse and purge times and number of cycles. Then, fluorine doping concentration will be optimized like in this study. Finally, electrical and optical properties of FTO will be optimized as a function of fluorine concentration.

REFERENCES

Abdelmohsen, A. H., Rouby, W. M. A. E., Ismail, N., & Farghali, A. A. (2017). Morphology Transition Engineering of ZnO Nanorods to Nanoplatelets Grafted Mo8O23-MoO2 by Polyoxometalates: Mechanism and Possible Applicability to other Oxides. *Scientific Reports*, *7*(1). https://doi.org/10.1038/s41598-017-05750-x

Abrutis, A., Silimavicius, L., Kubilius, V., Murauskas, T., Saltyte, Z., & Plausinaitiene, V. (2015). Doped zinc oxide films grown by hot-wire chemical vapour deposition. *Thin Solid Films*, *576*, 88–97. https://doi.org/10.1016/j.tsf.2015.01.010

Anusha, M., & Arivuoli, D. (2013). High intense violet luminescence in fluorine doped zinc oxide (FZO) thin films deposited by aerosol assisted CVD. *Journal of Alloys and Compounds*, *580*, 131-136.

Baboian, R., Hibner, E., & Martin, J. (2004). Chapter 51—Stainless Steels. In *Corrosion Tests and Standards: Application and Interpretation—Second Edition* (pp. 585-585–586). ASTM International. https://doi.org/10.1520/MNL11057M

Bädeker, K. (1907). Über die elektrische Leitfähigkeit und die thermoelektrische Kraft einiger Schwermetallverbindungen. *Annalen Der Physik*, *327*(4), 749–766. https://doi.org/10.1002/andp.19073270409

Banyamin, Z. Y., Kelly, P. J., West, G., & Boardman, J. (2014). Electrical and optical properties of fluorine doped tin oxide thin films prepared by magnetron sputtering. *Coatings*, *4*(4), 732–746. https://doi.org/10.3390/coatings4040732

Bernal-Correa, R., Morales-Acevedo, A., Montes-Monsalve, J., & Pulzara-Mora, A. (2016). Design of the TCO (ZnO:Al) thickness for glass/TCO/CdS/CIGS/Mo solar cells. *Journal of Physics D: Applied Physics*, *49*(12). https://doi.org/10.1088/0022-3727/49/12/125601

Betz, U., Kharrazi Olsson, M., Marthy, J., Escolá, M. F., & Atamny, F. (2006). Thin films engineering of indium tin oxide: Large area flat panel displays application.

Surface and Coatings Technology, *200*(20–21), 5751–5759. https://doi.org/10.1016/j.surfcoat.2005.08.144

Bhachu, D. S., Sankar, G., & Parkin, I. P. (2012). Aerosol assisted chemical vapor deposition of transparent conductive zinc oxide films. *Chemistry of Materials*, *24*(24), 4704–4710. https://doi.org/10.1021/cm302913b

Bomhard, E. M. (2018). The toxicology of indium oxide. In *Environmental Toxicology and Pharmacology* (Vol. 58, pp. 250–258). Elsevier B.V. https://doi.org/10.1016/j.etap.2018.02.003

Burstein, E. (1954). Anomalous Optical Absorption Limit in InSb. *Physical Review*, *93*(3), 632–633. https://doi.org/10.1103/PhysRev.93.632

Callister Jr., W. D., & Rethwisch, D. G. (2018). *Materials Science and Engineering: An Introduction, 10th Edition*. Hachette Livre - D. partement Pratique. https://www.wiley.com/en-sg/Materials+Science+and+Engineering:+An+Introduction,+10th+Edition-p-9781119405498

Calnan, S., Hüpkes, J., Rech, B., Siekmann, H., & Tiwari, A. N. (2008). High deposition rate aluminium-doped zinc oxide films with highly efficient light trapping for silicon thin film solar cells. *Thin Solid Films*, *516*(6), 1242–1248. https://doi.org/10.1016/j.tsf.2007.06.006

Cao, L., Zhu, L., Jiang, J., Zhao, R., Ye, Z., & Zhao, B. (2011). Highly transparent and conducting fluorine-doped ZnO thin films prepared by pulsed laser deposition. *Solar Energy Materials and Solar Cells*, *95*(3), 894–898. https://doi.org/10.1016/j.solmat.2010.11.012

Ceh, M., Chen, H.-C., Chen, M.-J., Yang, J.-R., & Shiojiri, M. (2010). Structure and Electro-Optical Properties of Thin Films Grown by Alternate Atomic Layer Deposition of ZnO and Al2O3 on the Sapphire Substrate. *MATERIALS TRANSACTIONS*, *51*(2), 219–226. https://doi.org/10.2320/matertrans.MC200902

Chae, G. S. (2001). A Modified Transparent Conducting Oxide for Flat Panel Displays Only. *Japanese Journal of Applied Physics*, *40*(3R), 1282. https://doi.org/10.1143/JJAP.40.1282

Choi, B. H., Im, H. B., Song, J. S., & Yoon, K. H. (1990). Optical and electrical properties of Ga2O3-doped ZnO films prepared by r.f. sputtering. *Thin Solid Films*, *193–194*, 712–720. https://doi.org/10.1016/0040-6090(90)90223-Z

Choi, Y. J., Kang, K. M., Lee, H. S., & Park, H. H. (2015). Non-laminated growth of chlorine-doped zinc oxide films by atomic layer deposition at low temperatures. *Journal of Materials Chemistry C*, *3*(32), 8336–8343. https://doi.org/10.1039/c5tc01763g

Choi, Y. J., Kang, K. M., & Park, H. H. (2015). Anion-controlled passivation effect of the atomic layer deposited ZnO films by F substitution to O-related defects on the electronic band structure for transparent contact layer of solar cell applications. *Solar Energy Materials and Solar Cells*, *132*, 403–409. https://doi.org/10.1016/j.solmat.2014.09.029

Choi, Y. J., & Park, H. H. (2014). A simple approach to the fabrication of fluorine-doped zinc oxide thin films by atomic layer deposition at low temperatures and an investigation into the growth mode. *Journal of Materials Chemistry C*, *2*(1), 98–108. https://doi.org/10.1039/c3tc31478b

Colegrove, E., Banai, R., Blissett, C., Buurma, C., Ellsworth, J., Morley, M., Barnes, S., Gilmore, C., Bergeson, J. D., Dhere, R., Scott, M., Gessert, T., & Sivananthan, S. (2012). High-efficiency polycrystalline CdS/CdTe solar cells on buffered commercial TCO-coated glass. *Journal of Electronic Materials*, *41*(10), 2833–2837. https://doi.org/10.1007/s11664-012-2100-z

Conwell, E., & Weisskopf, V. F. (1950). Theory of Impurity Scattering in Semiconductors. *Physical Review*, *77*(3), 388–390. https://doi.org/10.1103/PhysRev.77.388

Coutts, T. J., Young, D. L., & Li, X. (2000). Characterization of Transparent Conducting Oxides. *MRS Bulletin*, *25*(8), 58–65. https://doi.org/10.1557/mrs2000.152

Dagkaldiran, Ü., Gordijn, A., Finger, F., Yates, H. M., Evans, P., Sheel, D. W., Remes, Z., & Vanecek, M. (2009). Amorphous silicon solar cells made with SnO2:F TCO films deposited by atmospheric pressure CVD. *Materials Science and Engineering B: Solid-State Materials for Advanced Technology*, *159–160*(C), 6–9. https://doi.org/10.1016/j.mseb.2008.10.037

Dates, H. F., & Davis, J. K. (1967). *Iridizing Method*. https://patents.google.com/patent/US3331702A/en?oq=H.F.+Dates+and+J.K.+Davis%2c+U.S.+Patent+No.+3%2c331%2c702

De La, M., Olvera, L., Maldonado, A., & Asomoza, R. (2002). ZnO:F thin films deposited by chemical spray: effect of the fluorine concentration in the starting solution. In *Solar Energy Materials & Solar Cells* (Vol. 73).

Dezelah, C. L. (2015). Atomic Layer Deposition. In *Encyclopedia of Nanotechnology* (pp. 1–13). Springer Netherlands. https://doi.org/10.1007/978-94-007-6178-0_372-2

Dong, L., Sun, Q. Q., Shi, Y., Guo, H. W., Liu, H., Wang, C., Ding, S. J., & Zhang, D. W. (2009). Initial reaction mechanism of nitrogen-doped zinc oxide with atomic layer deposition. *Thin Solid Films*, *517*(15), 4355–4359. https://doi.org/10.1016/j.tsf.2009.03.014

Drude, P. (1900). Zur Elektronentheorie der Metalle; II. Teil. Galvanomagnetische und thermomagnetische Effecte. *Annalen Der Physik*, *308*(11), 369–402. https://doi.org/10.1002/andp.19003081102

Edwards, P. P., Porch, A., Jones, M. O., Morgan, D. V., & Perks, R. M. (2004). Basic materials physics of transparent conducting oxides. In *Dalton Transactions* (Issue 19, pp. 2995–3002). https://doi.org/10.1039/b408864f

Ellmer, K., Klein, A., & Rech, B. (Eds.). (2008). *Transparent Conductive Zinc Oxide* (Vol. 104). Springer Berlin Heidelberg. https://doi.org/10.1007/978-3-540-73612-7

Enoki, H., Nakayama, T., & Echigoya, J. (1992). The Electrical and Optical Properties of the ZnO-SnO2 Thin Films Prepared by RF Magnetron Sputtering. *Physica Status Solidi (a)*, *129*(1), 181–191. https://doi.org/10.1002/pssa.2211290116

Fan, J. C. C., & Goodenough, J. B. (1977). X-ray photoemission spectroscopy studies of Sn-doped indium-oxide films. *Journal of Applied Physics*, *48*(8), 3524–3531. https://doi.org/10.1063/1.324149

Frank, G., & Köstlin, H. (1982). Electrical properties and defect model of tin-doped indium oxide layers. *Applied Physics A Solids and Surfaces*, *27*(4), 197–206. https://doi.org/10.1007/BF00619080

Gao, Q., Jiang, H., Li, C., Ma, Y., Li, X., Ren, Z., Liu, Y., Song, C., & Han, G. (2013). Tailoring of textured transparent conductive SnO2:F thin films. *Journal of Alloys and Compounds*, *574*, 427–431. https://doi.org/10.1016/j.jallcom.2013.05.108

George, S. M. (2010). Atomic layer deposition: An overview. *Chemical Reviews*, *110*(1), 111–131. https://doi.org/10.1021/cr900056b

Gordon, R. G. (1979). *Method of depositing electrically conductive, infra-red reflective, transparent coatings of stannic oxide*.

Gordon, R. G. (2000). Criteria for Choosing Transparent Conductors. *MRS Bulletin*, *25*(8), 52–57. https://doi.org/10.1557/mrs2000.151

Granqvist, C. G. (2009). Transparent conductors for solar energy and energy efficiency: a broad-brush picture. In *Int. J. Nanotechnol* (Vol. 6, Issue 9).

Gunasekaran, E., Ezhilan, M., Mani, G. K., Shankar, P., Kulandaisamy, A. J., Rayappan, J. B. B., & Babu, K. J. (2018). Fluorine doped ZnO thin film as acetaldehyde sensor. *Semiconductor Science and Technology*, *33*(9). https://doi.org/10.1088/1361-6641/aad2ab

Guo, Y., Zhu, L., Li, Y., Niu, W., Zhang, X., & Ye, Z. (2015). Interaction of H and F atoms - Origin of the high conductive stability of hydrogen-incorporated F-doped ZnO thin films. *Thin Solid Films*, *589*, 85–89. https://doi.org/10.1016/j.tsf.2015.05.003

Guziewicz, E., Krajewski, T. A., Przezdziecka, E., Korona, K. P., Czechowski, N., Klopotowski, L., & Terziyska, P. (2020). Zinc Oxide Grown by Atomic Layer Deposition: From Heavily n-Type to p-Type Material. *Physica Status Solidi (B) Basic Research*, *257*(2). https://doi.org/10.1002/pssb.201900472

Hagleitner, D. R., Menhart, M., Jacobson, P., Blomberg, S., Schulte, K., Lundgren, E., Kubicek, M., Fleig, J., Kubel, F., Puls, C., Limbeck, A., Hutter, H., Boatner, L. A., Schmid, M., & Diebold, U. (2012). Bulk and surface characterization of In 2O3 (001) single crystals. *Physical Review B - Condensed Matter and Materials Physics*, *85*(11). https://doi.org/10.1103/PhysRevB.85.115441

Hamberg, I., & Granqvist, C. G. (1986). Evaporated Sn-doped In2O3 films: Basic optical properties and applications to energy-efficient windows. *Journal of Applied Physics*, *60*(11). https://doi.org/10.1063/1.337534

Hamberg, I., Granqvist, C. G., Berggren, K.-F., Sernelius, B. E., & Engström, L. (1984). Band-gap widening in heavily Sn-doped In2O3. *Physical Review B*, *30*(6), 3240–3249. https://doi.org/10.1103/PhysRevB.30.3240

Her, S. C., & Chang, C. F. (2017). Fabrication and characterization of indium tin oxide films. *Journal of Applied Biomaterials and Functional Materials*, *15*(2), e170–e175. https://doi.org/10.5301/jabfm.5000345

Hu, J., & Gordon, R. G. (1991). Textured fluorine-doped ZnO films by atmospheric pressure chemical vapor deposition and their use in amorphous silicon solar cells. *Solar Cells*, *30*(1–4), 437–450. https://doi.org/10.1016/0379-6787(91)90076-2

Hu, J., & Gordon, R. G. (1992). Atmospheric pressure chemical vapor deposition of gallium doped zinc oxide thin films from diethyl zinc, water, and triethyl gallium. *Journal of Applied Physics*, *72*(11), 5381–5392. https://doi.org/10.1063/1.351977

Huang, G., Yu, Q., Kou, S., Zhai, P., & Li, G. (2021). Epitaxial indium tin oxide films deposited on yttrium stabilized zirconia substrate by DC magnetron sputtering. *Physica B: Condensed Matter*, *601*. https://doi.org/10.1016/j.physb.2020.412667

Hurma, T., & Caglar, M. (2020). Effect of anionic fluorine incorporation on structural, optical and electrical properties of ZnO nanocrystalline films. *Materials Science in Semiconductor Processing*, *110*. https://doi.org/10.1016/j.mssp.2020.104949

Hutson, A. R. (1960). Piezoelectricity and Conductivity in ZnO and CdS. *Physical Review Letters*, *4*(10), 505–507. https://doi.org/10.1103/PhysRevLett.4.505

Jagadish, C., & Pearton, S. (Eds.). (2006). *Zinc Oxide Bulk, Thin Films and Nanostructures_ Processing, Properties, and Applications* (1st ed.).

Janotti, A., & Van De Walle, C. G. (2009). Fundamentals of zinc oxide as a semiconductor. *Reports on Progress in Physics*, *72*(12). https://doi.org/10.1088/0034-4885/72/12/126501

Kääriäinen, T., Cameron, D., Kääriäinen, M. L., & Sherman, A. (2013). *Atomic layer deposition: principles, characteristics, and nanotechnology applications*. John Wiley & Sons. https://www.wiley.com/en-ie/Atomic+Layer+Deposition:+Principles,+Characteristics,+and+Nanotechnology+Applications,+2nd+Edition-p-9781118062777

Kang, K. M., & Park, H. H. (2018). Effect of Atomic Layer Deposition Temperature on the Growth Orientation, Morphology, and Electrical, Optical, and Band-Structural Properties of ZnO and Fluorine-Doped ZnO Thin Films. *Journal of Physical Chemistry C*, *122*(1), 377–385. https://doi.org/10.1021/acs.jpcc.7b08943

Kang, K.-M., Choi, Y.-J., Yeom, G. Y., & Park, H.-H. (2016). Thickness-dependent growth orientation of F-doped ZnO films formed by atomic layer deposition. *Journal of Vacuum Science & Technology A: Vacuum, Surfaces, and Films*, *34*(1). https://doi.org/10.1116/1.4938180

Katayama, M. (1999). TFT-LCD technology. *Thin Solid Films*, *341*(1–2), 140–147. https://doi.org/10.1016/S0040-6090(98)01519-3

Khan, S., & Stamate, E. (2022). Comparative Study of Aluminum-Doped Zinc Oxide, Gallium-Doped Zinc Oxide and Indium-Doped Tin Oxide Thin Films Deposited by Radio Frequency Magnetron Sputtering. *Nanomaterials*, *12*(9). https://doi.org/10.3390/nano12091539

Kireev, P. S. (1975). *Semiconductor Physics*. Mir Publishers.

Kittel, C., & Holcomb, D. F. (1967). Introduction to Solid State Physics. *American Journal of Physics*, *35*(6), 547–548. https://doi.org/10.1119/1.1974177

Kopalko, K., Wójcik, A., Godlewski, M., Łusakowska, E., Paszkowicz, W., Domagała, J. Z., Godlewski, M. M., Szezerbakow, A., Świątek, K., & Dybko, K. (2005). Growth by atomic layer epitaxy and characterization of thin films of ZnO. *Physica Status Solidi C: Conferences*, *2*(3), 1125–1130. https://doi.org/10.1002/pssc.200460660

Köstlin, H., Jost, R., & Lems, W. (1975). Optical and electrical properties of doped In2O3 films. *Physica Status Solidi (a)*, *29*(1), 87–93. https://doi.org/10.1002/pssa.2210290110

Lampert, C. M. (1981). Heat mirror coatings for energy conserving windows. *Solar Energy Materials*, *6*(1), 1–41. https://doi.org/10.1016/0165-1633(81)90047-2

Lebbad, A., Kerkache, L., Layadi, A., Leroy, F., Alshehri, B., & Dogheche, E. (2018). Surface morphology, structural and electrical properties of RF-sputtered ITO thin films on si substrates. *Bulletin of Materials Science*, *41*(3). https://doi.org/10.1007/s12034-018-1595-1

Lee, J. C., Subramaniam, N. G., Lee, J. W., Lee, J. C., & Kang, T. W. (2013). Evaluation of optimal chlorine doping concentration in zinc oxide on glass for application as new transparent conductive oxide. *Physica Status Solidi (A) Applications and Materials Science*, *210*(12), 2638–2643. https://doi.org/10.1002/pssa.201330042

Lee, Y. J., Kim, J. H., Park, J. C., Kim, Y. H., Jung, D., & Kim, T. W. (2014). Characteristics of AZO electrode with high transmittance in near infrared range. *Journal of Nanoscience and Nanotechnology*, *14*(12), 9285–9288. https://doi.org/10.1166/jnn.2014.10110

Leskela, M., & Ritalä, M. R. (2002). Atomic layer deposition (ALD): from precursors to thin film structures. In *Thin Solid Films* (Vol. 409).

Lewis, B. G., & Paine, D. C. (2000). Applications and Processing of Transparent Conducting Oxides. *MRS Bulletin*, *25*(8), 22–27. https://doi.org/10.1557/mrs2000.147

Liang, H., & Gordon, R. G. (2007). Atmospheric pressure chemical vapor deposition of transparent conducting films of fluorine doped zinc oxide and their application to amorphous silicon solar cells. *Journal of Materials Science*, *42*(15), 6388–6399. https://doi.org/10.1007/s10853-006-1255-5

Liao, B.-H., Kuo, C.-C., Chen, P.-J., & Lee, C.-C. (2011). Fluorine-doped tin oxide films grown by pulsed direct current magnetron sputtering with an Sn target. *Applied Optics*, *50*(9), C106. https://doi.org/10.1364/AO.50.00C106

Lin, M.-C., Chang, Y.-J., Chen, M.-J., & Chu, C.-J. (2011). Characteristics of Zr-Doped ZnO Thin Films Grown by Atomic Layer Deposition. *Journal of The Electrochemical Society*, *158*(6), D395. https://doi.org/10.1149/1.3575161

Liu, B., Gu, M., Liu, X., Huang, S., & Ni, C. (2010a). First-principles study of fluorine-doped zinc oxide. *Applied Physics Letters*, *97*(12). https://doi.org/10.1063/1.3492444

Liu, B., Gu, M., Liu, X., Huang, S., & Ni, C. (2010b). First-principles study of fluorine-doped zinc oxide. *Applied Physics Letters*, *97*(12). https://doi.org/10.1063/1.3492444

Lončarević, D., & Čupić, Ž. (2019). The perspective of using nanocatalysts in the environmental requirements and energy needs of industry. In *Industrial Applications of Nanomaterials* (pp. 91–122). Elsevier. https://doi.org/10.1016/B978-0-12-815749-7.00004-9

Look, D. C. (2001). Recent advances in ZnO materials and devices. In *Materials Science and Engineering* (Vol. 80). www.elsevier.com/locate/mseb

Løvvik, O. M., Diplas, S., Romanyuk, A., & Ulyashin, A. (2014). Initial stages of ITO/Si interface formation: In situ x-ray photoelectron spectroscopy measurements upon magnetron sputtering and atomistic modelling using density functional theory. *Journal of Applied Physics*, *115*(8). https://doi.org/10.1063/1.4866991

Lytle, W. O., Junge, A. E., & Ken, N. (1951). *ELECTROCONDUCTIVE PRODUCTS AND PRODUCTION THEREOF*.

Ma, J., Ji, F., Ma, H., & Li, S. (2000). Preparation and properties of transparent conducting zinc oxide and aluminium-doped zinc oxide films prepared by evaporating method. *Solar Energy Materials and Solar Cells*, *60*(4), 341–348. https://doi.org/10.1016/S0927-0248(99)00076-8

Major, S., Banerjee, A., & Chopra, K. L. (1984). Annealing studies of undoped and indium-doped films of zinc oxide. *Thin Solid Films*, *122*(1), 31–43. https://doi.org/10.1016/0040-6090(84)90376-6

Majumder, S. B., Jain, M., Dobal, P. S., & Katiyar, R. S. (2003). Investigations on solution derived aluminium doped zinc oxide thin films. *Materials Science and Engineering B: Solid-State Materials for Advanced Technology*, *103*(1), 16–25. https://doi.org/10.1016/S0921-5107(03)00128-4

Maldonado, F., & Stashans, A. (2010). Al-doped ZnO: Electronic, electrical and structural properties. *Journal of Physics and Chemistry of Solids*, *71*(5), 784–787. https://doi.org/10.1016/j.jpcs.2010.02.001

Manifacier, J. C., De Murcia, M., Fillard, J. P., & Vicario, E. (1977). Optical and electrical properties of SnO2 thin films in relation to their stoichiometric deviation and their crystalline structure. *Thin Solid Films*, *41*(2), 127–135. https://doi.org/10.1016/0040-6090(77)90395-9

Marezio, M. (1966). Refinement of the crystal structure of In2O3 at two wavelengths. *Acta Crystallographica*, *20*(6), 723–728. https://doi.org/10.1107/S0365110X66001749

Mattox, D. M. (2002). Physical vapor deposition (PVD) processes. *Metal Finishing*, *100*, 394–408. https://doi.org/10.1016/S0026-0576(02)82043-8

Mcgraw, J. M., Parilla, P. A., Schulz, D. L., Alleman, J., Wu, X., Mulligan, W. P., Ginley, D. S., & Coutts, T. J. (1995). Pulsed Laser Deposition of Cadmium Stannate, a Spinel-Type Transparent Conducting Oxide. *MRS Proceedings*, *388*, 51. https://doi.org/10.1557/PROC-388-51

Mcmaster, H. A. (1947). *CONDUCTIVE COATING FOR GLASS AND METHOD OF APPLICATION*.

McMaster, H. A. (1947). *Electrically conducting films and method of application*.

Mehmood, U., Afzaal, M., Al-Ahmed, A., Yates, H. M., Hakeem, A. S., Ali, H., & Al-Sulaiman, F. A. (2017). Transparent Conductive Oxide Films for High-Performance Dye-Sensitized Solar Cells. *IEEE Journal of Photovoltaics*, *7*(2), 518–524. https://doi.org/10.1109/JPHOTOV.2016.2641303

Min, Y. S., An, C. J., Kim, S. K., Song, J., & Hwang, C. S. (2010). Growth and characterization of conducting ZnO thin films by atomic layer deposition. *Bulletin of the Korean Chemical Society*, *31*(9), 2503–2508. https://doi.org/10.5012/bkcs.2010.31.9.2503

Minami, T. (2000). New n-Type Transparent Conducting Oxides. *MRS Bulletin*, *25*(8), 38–44. https://doi.org/10.1557/mrs2000.149

Minami, T. (2005). Transparent conducting oxide semiconductors for transparent electrodes. *Semiconductor Science and Technology*, *20*(4). https://doi.org/10.1088/0268-1242/20/4/004

Minami, T., Sato, H., Nanto, H., & Takata, S. (1985). Group III Impurity Doped Zinc Oxide Thin Films Prepared by RF Magnetron Sputtering. *Japanese Journal of Applied Physics*, *24*(10A), L781. https://doi.org/10.1143/JJAP.24.L781

Mineral Commodity Summaries. (2002). https://doi.org/10.3133/mineral2002

Mineral Commodity Summaries. (2007). https://doi.org/10.3133/mineral2007

Mineral Commodity Summaries. (2012). https://doi.org/10.3133/mineral2012

Mineral Commodity Summaries. (2017). https://doi.org/10.3133/70180197

Mineral commodity summaries. (2022). https://doi.org/10.3133/mcs2022

Mineral commodity summaries. (2023). https://doi.org/10.3133/mcs2023

Mitsugi, F., Umeda, Y., Sakai, N., & Ikegami, T. (2010). Uniformity of gallium doped zinc oxide thin film prepared by pulsed laser deposition. *Thin Solid Films*, *518*(22), 6334–6338. https://doi.org/10.1016/j.tsf.2010.03.044

Mo, G., Liu, J., Lin, G., Zou, Z., Wei, Z., Liu, Y., He, H., Fu, Y., & Shen, X. (2019). Characterization of low resistivity Ga-doped ZnO thin films on Si substrates prepared by pulsed laser deposition. *Materials Research Express*, *6*(10). https://doi.org/10.1088/2053-1591/ab3a6c

Moehel, J. M. (1951). *Electrically conducting coatings on glass and other ceramic bodies*.

Morkoç, H., & Özgür, Ü. (2008). *Zinc Oxide: Fundamentals, Materials and Device Technology*. John Wiley & Sons.

Mott, N. F. (1956). On The Transition to Metallic Conduction In Semiconductors. *Canadian Journal of Physics*, *34*(12A), 1356–1368. https://doi.org/10.1139/p56-151

Mott, N. F. (1961). The transition to the metallic state. *Philosophical Magazine*, *6*(62), 287–309. https://doi.org/10.1080/14786436108243318

Muhammad, A., Hassan, Z., Mohammad, S. M., & Rajamanickam, S. (2021). Enhanced sensitivity of low-cost fabricated fluorine doped ZnO metal semiconductor metal photodetector. *Optical Materials*, *122*. https://doi.org/10.1016/j.optmat.2021.111771

Nagarani, S., & Sanjeeviraja, C. (2011). Structural, electrical and optical properties of gallium doped zinc oxide thin films prepared by electron beam evaporation technique. *AIP Conference Proceedings*, *1349*(PART A), 589–590. https://doi.org/10.1063/1.3605995

Nishinaka, H., & Yoshimoto, M. (2018). Mist Chemical Vapor Deposition of Single-Phase Metastable Rhombohedral Indium Tin Oxide Epitaxial Thin Films with High Electrical Conductivity and Transparency on Various α-Al2O3 Substrates. *Crystal Growth and Design*, *18*(7), 4022–4028. https://doi.org/10.1021/acs.cgd.8b00387

Noirfalise, X., Godfroid, T., Guisbiers, G., & Snyders, R. (2011). Synthesis of fluorine doped zinc oxide by reactive magnetron sputtering. *Acta Materialia*, *59*(20), 7521–7529. https://doi.org/10.1016/j.actamat.2011.07.068

Nordberg, G. F., Fowler, B. A., & Nordberg, M. (2007). *Handbook on the Toxicology of Metals*. Elsevier. https://doi.org/10.1016/B978-0-12-369413-3.X5052-6

Nozik, A. J. (1974). *Light-transmitting electrically conducting cadmium stannate and methods of producing same*.

Nozik, A. J., & Haacke, G. (1976). *Greenhouse window for solar heat absorbing systems derived from Cd2 SnO4*.

Ott, A. W., & Chang, R. P. H. (1999). Atomic layer-controlled growth of transparent conducting ZnO on plastic substrates. *Materials Chemistry and Physics*, *58*(2), 132–138. https://doi.org/10.1016/S0254-0584(98)00264-8

Owen, J. I., Pust, S. E., Bunte, E., & Hüpkes, J. (2012). ZnO Etch-Feature Control via Concentration and Temperature of Various Acids. *ECS Journal of Solid State Science and Technology*, *1*(1), P11–P17. https://doi.org/10.1149/2.013201jss

Özgür, Ü., Alivov, Y. I., Liu, C., Teke, A., Reshchikov, M. A., Doğan, S., Avrutin, V., Cho, S. J., & Morkǫ, H. (2005). A comprehensive review of ZnO materials and devices. In *Journal of Applied Physics* (Vol. 98, Issue 4, pp. 1–103). https://doi.org/10.1063/1.1992666

Pankove, J. I., & Kiewit, D. A. (1972). Optical Processes in Semiconductors. *Journal of The Electrochemical Society*, *119*(5), 156C. https://doi.org/10.1149/1.2404256

Papari, G. P., Silvestri, B., Vitiello, G., De Stefano, L., Rea, I., Luciani, G., Aronne, A., & Andreone, A. (2017). Morphological, Structural, and Charge Transfer Properties of F-Doped ZnO: A Spectroscopic Investigation. *Journal of Physical Chemistry C*, *121*(29), 16012–16020. https://doi.org/10.1021/acs.jpcc.7b04821

Park, H., Choi, Y., & Kang, K. (2015). *HALOGEN DOPING SOURCE FOR DOPING OXIDE THIN FILM WITH HALOGEN USING ATOMIC LAYER DEPOSITION, METHOD FOR MANUFACTURING THE HALOGEN DOPING SOURCE,*

METHOD FOR DOPING OXIDE THIN FILM WITH HALOGEN USING ATOMIC LAYER DEPOSITION, AND OXIDE THIN FILM DOPED WITH HALOGEN MANUFACTURED BY USING THE METHOD FOR DOPING OXIDE THIN FILM WITH HALOGEN (Patent US20150184000A1). Patent Application Publication. https://patents.google.com/patent/US20150184000A1/en?oq=US+2015%2f0184000+A1

Park, H., Lee, Y. J., Park, J., Kim, Y., Yi, J., Lee, Y., Kim, S., Park, C. K., & Lim, K. J. (2018). Front and Back TCO Research Review of a-Si/c-Si Heterojunction with Intrinsic Thin Layer (HIT) Solar Cell. In *Transactions on Electrical and Electronic Materials* (Vol. 19, Issue 3, pp. 165–172). Korean Institute of Electrical and Electronic Material Engineers. https://doi.org/10.1007/s42341-018-0026-8

Pasquarelli, R. M., Ginley, D. S., & O'hayre, R. (2011). Solution processing of transparent conductors: From flask to film. *Chemical Society Reviews*, *40*(11), 5406–5441. https://doi.org/10.1039/c1cs15065k

Pawar, B. N., Ham, D. H., Mane, R. S., Ganesh, T., Cho, B. W., & Han, S. H. (2008). Fluorine-doped zinc oxide transparent and conducting electrode by chemical spray synthesis. *Applied Surface Science*, *254*(20), 6294–6297. https://doi.org/10.1016/j.apsusc.2008.02.088

Petritz, R. L., & Kingston, R. H. (1956). Theory of Photoconductivity in Semiconductor Films. In *J. Chem. Phys* (Vol. 104). John Wiley and Sons.

Pham, A. T. T., Ngo, N. M., Le, O. K. T., Hoang, D. Van, Nguyen, T. H., Phan, T. B., & Tran, V. C. (2021). High-mobility sputtered F-doped ZnO films as good-performance transparent-electrode layers. *Journal of Science: Advanced Materials and Devices*, *6*(3), 446–452. https://doi.org/10.1016/j.jsamd.2021.05.004

Pierson, H. O. (1992). FUNDAMENTALS OF CHEMICAL VAPOR DEPOSITION. In *Handbook of Chemical Vapor Deposition* (pp. 17–50). Elsevier. https://doi.org/10.1016/B978-0-8155-1300-1.50008-8

Pilvi, T., Puukilainen, E., Kreissig, U., Leskelä, M., & Ritala, M. (2008). Atomic layer deposition of MgF2 thin films using TaF5 as a novel fluorine source. *Chemistry of Materials*, *20*(15), 5023–5028. https://doi.org/10.1021/cm800948k

Pilvi, T., Ritala, M., Leskelä, M., Bischoff, M., Kaiser, U., & Kaiser, N. (2008). Atomic layer deposition process with TiF4 as a precursor for depositing metal fluoride thin films. *Applied Optics*, *47*(13), C271. https://doi.org/10.1364/AO.47.00C271

Pilz, J., Perrotta, A., Leising, G., & Coclite, A. M. (2020). ZnO Thin Films Grown by Plasma-Enhanced Atomic Layer Deposition: Material Properties Within and Outside the "Atomic Layer Deposition Window." *Physica Status Solidi (A) Applications and Materials Science*, *217*(8). https://doi.org/10.1002/pssa.201900256

Polydorou, E., Zeniou, A., Tsikritzis, D., Soultati, A., Sakellis, I., Gardelis, S., Papadopoulos, T. A., Briscoe, J., Palilis, L. C., Kennou, S., Gogolides, E., Argitis, P., Davazoglou, D., & Vasilopoulou, M. (2016). Surface passivation effect by fluorine plasma treatment on ZnO for efficiency and lifetime improvement of inverted polymer solar cells. *Journal of Materials Chemistry A*, *4*(30), 11844–11858. https://doi.org/10.1039/c6ta03594a

Porch, A., Morgan, D. V., Perks, R. M., Jones, M. O., & Edwards, P. P. (2004). Transparent current spreading layers for optoelectronic devices. *Journal of Applied Physics*, *96*(8), 4211–4218. https://doi.org/10.1063/1.1786674

Preston, J. S. (1950). Constitution and mechanism of the selenium rectifier photocell. *Proceedings of the Royal Society of London. Series A. Mathematical and Physical Sciences*, *202*(1071), 449–466. https://doi.org/10.1098/rspa.1950.0112

Profijt, H. B., Potts, S. E., van de Sanden, M. C. M., & Kessels, W. M. M. (2011). Plasma-Assisted Atomic Layer Deposition: Basics, Opportunities, and Challenges. *Journal of Vacuum Science & Technology A: Vacuum, Surfaces, and Films*, *29*(5), 050801. https://doi.org/10.1116/1.3609974

Puurunen, R. L. (2003). Growth Per Cycle in Atomic Layer Deposition: A Theoretical Model. *Chemical Vapor Deposition*, *9*(5), 249–257. https://doi.org/10.1002/cvde.200306265

Qiu, S. N., Qiu, C. X., & Shih, I. (1987). Preparation of thin films. *Solar Energy Materials*, *16*(6), 471–475. https://doi.org/10.1016/0165-1633(87)90048-7

Raha, S., & Ahmaruzzaman, M. (2022). ZnO nanostructured materials and their potential applications: progress, challenges and perspectives. In *Nanoscale Advances* (Vol. 4, Issue 8, pp. 1868–1925). Royal Society of Chemistry. https://doi.org/10.1039/d1na00880c

Rousset, J., Saucedo, E., & Lincot, D. (2009). Extrinsic doping of electrodeposited zinc oxide films by chlorine for transparent conductive oxide applications. *Chemistry of Materials*, *21*(3), 534–540. https://doi.org/10.1021/cm802765c

Salami, H., Uy, A., Vadapalli, A., Grob, C., Dwivedi, V., & Adomaitis, R. A. (2019). Atomic layer deposition of ultrathin indium oxide and indium tin oxide films using a trimethylindium, tetrakis(dimethylamino)tin, and ozone precursor system. *Journal of Vacuum Science & Technology A: Vacuum, Surfaces, and Films*, *37*(1). https://doi.org/10.1116/1.5058171

Samanta, S., Paramanik, B., & Das, D. (2022). Structural characteristics, impedance spectroscopy, ac-conductivity and dielectric loss studies on RF-magnetron sputtered F doped ZnO (FZO) thin films. *Ceramics International*, *48*(21), 31370–31380. https://doi.org/10.1016/j.ceramint.2022.07.013

Sanchez-Juarez, A., Tiburcio-Silver, A., & Ortiz, A. (1998). Properties of fluorine-doped ZnO deposited onto glass by spray pyrolysis. In *Solar Energy Materials and Solar Cells* (Vol. 52).

Schmidt-Mende, L., & MacManus-Driscoll, J. L. (2007). ZnO - nanostructures, defects, and devices. *Materials Today*, *10*(5), 40–48. https://doi.org/10.1016/S1369-7021(07)70078-0

Şennik, E., Kerli, S., Alver, Ü., & Öztürk, Z. Z. (2015). Effect of fluorine doping on the NO2-sensing properties of ZnO thin films. *Sensors and Actuators, B: Chemical*, *216*, 49–56. https://doi.org/10.1016/j.snb.2015.04.023

Seto, J. Y. W. (1975). The electrical properties of polycrystalline silicon films. *Journal of Applied Physics*, *46*(12), 5247–5254. https://doi.org/10.1063/1.321593

Shevjakov, A. M., Kuznetsova, G. N., & Aleskovskii, V. B. (1965). Chemistry of high-temperature materials. *In Proceedings of the Second USSR Conference on High-Temperature Chemistry of Oxides*, 26–29.

Shigesato, Y., & Paine, D. C. (1993). Study of the effect of Sn doping on the electronic transport properties of thin film indium oxide. *Applied Physics Letters*, *62*(11), 1268–1270. https://doi.org/10.1063/1.108703

Srivastava, K., & Secco, E. A. (1967). Studies on metal hydroxy compounds. I. Thermal analyses of zinc derivatives E-Zn(0H) z, Znj(OH)8C12.H20, g-ZnOHC1, and ZnOHF. In *Canadian Journal of Chemistry* (Vol. 45). www.nrcresearchpress.com

Suntola, T. (1989). Atomic layer epitaxy. *Materials Science Reports*, *4*(5), 261–312. https://doi.org/10.1016/S0920-2307(89)80006-4

Suntola, T., & Antson, J. (1977). *Method for producing compound thin films* (Patent 4,058,430).

Szabó, Z., Baji, Z., Basa, P., Czigány, Z., Bársony, I., Wang, H. Y., & Volk, J. (2016). Homogeneous transparent conductive ZnO:Ga by ALD for large LED wafers. *Applied Surface Science*, *379*, 304–308. https://doi.org/10.1016/j.apsusc.2016.04.081

Tauc, J., Grigorovici, R., & Vancu, A. (1966). Optical Properties and Electronic Structure of Amorphous Germanium. *Physica Status Solidi (b)*, *15*(2), 627–637. https://doi.org/10.1002/pssb.19660150224

Tomer, S., Panigrahi, J., Pathi, P., Gupta, G., & Vandana. (2021). Effect of ALD window on thermal ALD deposited HfOx/Si interface for silicon surface

passivation. *Materials Today: Proceedings*, *46*, 5761–5765. https://doi.org/10.1016/j.matpr.2021.02.711

Tsai, Y. Z., Wang, N. F., & Tsai, C. L. (2009). Formation of F-doped ZnO transparent conductive films by sputtering of ZnF2. *Materials Letters*, *63*(18–19), 1621–1623. https://doi.org/10.1016/j.matlet.2009.04.032

Van Boort, H. J. J., & Groth, R. (1968). Low-pressure sodium lamps with indium oxide filter. *Philips Technical Review*, *29*, 47–48. https://www.pearl-hifi.com/06_Lit_Archive/02_PEARL_Arch/Vol_16/Sec_53/Philips_Tech_Review/PTechReview-29-1968-017.pdf

Wenas, W. W., Yamada, A., Takahashi, K., Yoshino, M., & Konagai, M. (1991). Electrical and optical properties of boron-doped ZnO thin films for solar cells grown by metalorganic chemical vapor deposition. *Journal of Applied Physics*, *70*(11), 7119–7123. https://doi.org/10.1063/1.349794

White, D. L., & Feldman, M. (1970). Liquid-crystal light valves. *Electronics Letters*, *6*(26), 837. https://doi.org/10.1049/el:19700578

Wu, C. C. (2018). Highly flexible touch screen panel fabricated with silver-inserted transparent ITO triple-layer structures. *RSC Advances*, *8*(22), 11862–11870. https://doi.org/10.1039/c7ra13550e

Wu, C. C., Yang, C. C., Wang, J. Z., & Chen, C. H. (2018). The characteristics of the gallium-doped zinc oxide films using radio frequency magnetron sputtering. *Proceedings - 2018 7th International Symposium on Next-Generation Electronics, ISNE 2018*, 1–3. https://doi.org/10.1109/ISNE.2018.8394654

Xu, H. Y., Liu, Y. C., Mu, R., Shao, C. L., Lu, Y. M., Shen, D. Z., & Fan, X. W. (2005). F-doping effects on electrical and optical properties of ZnO nanocrystalline films. *Applied Physics Letters*, *86*(12), 1–3. https://doi.org/10.1063/1.1884256

Yamada, A., Sang, B., & Konagai, M. (1997). Atomic layer deposition of ZnO transparent conducting oxides. *Applied Surface Science*, *112*, 216–222. https://doi.org/10.1016/S0169-4332(96)01022-7

Zhang, D. H., & Ma, H. L. (1996). Scattering mechanisms of charge carriers in transparent conducting oxide films. In *Appl. Phys. A* (Vol. 62).

Zhang, J., Yang, H., Zhang, Q. L., Dong, S., & Luo, J. K. (2013). Structural, optical, electrical and resistive switching properties of ZnO thin films deposited by thermal and plasma-enhanced atomic layer deposition. *Applied Surface Science*, *282*, 390–395. https://doi.org/10.1016/j.apsusc.2013.05.141

Zhang, X., Zhu, L., Xu, H., Chen, L., Guo, Y., & Ye, Z. (2014). Highly transparent conductive F-doped ZnO films in wide range of visible and near infrared wavelength deposited on polycarbonate substrates. In *Journal of Alloys and Compounds* (Vol. 614, pp. 71–74). Elsevier Ltd. https://doi.org/10.1016/j.jallcom.2014.06.098

Zhou, Y., Xu, W., Li, J., Yin, C., Liu, Y., Zhao, B., Chen, Z., He, C., Mao, W., & Ito, K. (2019). Vacancy defects and optoelectrical properties for fluorine tin oxide thin films with various SnF2 contents. *Journal of Applied Physics*, *125*(23). https://doi.org/10.1063/1.5110975

Zhuo, Y., Chen, Z., Tu, W., Ma, X., & Wang, G. (2018). Structural, electrical and optical properties of indium tin oxide thin film grown by metal organic chemical vapor deposition with tetramethyltin-precursor. *Japanese Journal of Applied Physics*, *57*(1). https://doi.org/10.7567/JJAP.57.01AE03